UNIVERSIDADE FEDERAL DE SANTA CATARINA
CENTRO TECNOLÓGICO DE JOINVILLE
PROGRAMA DE PÓS-GRADUAÇÃO EM ENGENHARIA E CIÊNCIAS MECÂNICAS

Rodrigo Michels

INVESTIGATION ON THE INFLUENCE OF CAPILLARY NUMBER ON THE IMMISCIBLE DISPLACEMENT USING A LATTICE BOLTZMANN METHOD

Joinville
2020

Rodrigo Michels

INVESTIGATION ON THE INFLUENCE OF CAPILLARY NUMBER ON THE IMMISCIBLE DISPLACEMENT USING A LATTICE BOLTZMANN METHOD

Dissertação submetida ao Programa de Pós-Graduação em Engenharia e Ciências Mecânicas da Universidade Federal de Santa Catarina para a obtenção do título de Mestre em Engenharia e Ciências Mecânicas.
Orientador: Prof. Luis Orlando Emerich dos Santos, Dr.
Coorientador: Prof. Diogo Nardelli Siebert, Dr.

Joinville
2020

Ficha de identificação da obra elaborada pelo autor,
através do Programa de Geração Automática da Biblioteca Universitária da UFSC.

Michels, Rodrigo
Investigation on the influence of capillary number on the immiscible displacement using a Lattice Boltzmann Method / Rodrigo Michels ; orientador, Luis Orlando Emerich dos Santos, coorientador, Diogo Nardelli Siebert, 2020.
103 p.

Dissertação (mestrado) - Universidade Federal de Santa Catarina, Campus Joinville, Programa de Pós-Graduação em Engenharia e Ciências Mecânicas, Joinville, 2020.

Inclui referências.

1. Engenharia e Ciências Mecânicas. 2. drainage. 3. porous media. 4. Lattice Boltzmann. 5. capillary number. I. dos Santos, Luis Orlando Emerich. II. Siebert, Diogo Nardelli. III. Universidade Federal de Santa Catarina. Programa de Pós-Graduação em Engenharia e Ciências Mecânicas. IV. Título.

Rodrigo Michels

INVESTIGATION ON THE INFLUENCE OF CAPILLARY NUMBER ON THE IMMISCIBLE DISPLACEMENT USING A LATTICE BOLTZMANN METHOD

O presente trabalho em nível de mestrado foi avaliado e aprovado por banca examinadora composta pelos seguintes membros:

Prof. Luiz Adolfo Hegele Jr., Dr.
Universidade do Estado de Santa Catarina

Prof. Fabiano Gilberto Wolf, Dr.
Universidade Federal de Santa Catarina

Prof. Kleber Vieira de Paiva, Dr.
Universidade Federal de Santa Catarina

Certificamos que esta é a versão original e final do trabalho de conclusão que foi julgado adequado para obtenção do título de Mestre em Engenharia e Ciências Mecânicas.

Documento assinado digitalmente
Regis Kovacs Scalice
Data: 27/04/2020 15:17:54-0300
CPF: 163.286.178-01

Prof. Régis Kovacs Scalice , Dr.
Coordenador

Documento assinado digitalmente
Luis Orlando Emerich dos Santos
Data: 27/04/2020 12:19:29-0300
CPF: 120.977.838-64

Prof. Luis Orlando Emerich dos Santos, Dr.
Orientador

Joinville, 2020.

RESUMO

A extração de petróleo de reservatórios não convencionais requer a compreensão da dinâmica do deslocamento imiscível em meios porosos. Este é um fenômeno complexo na mecânica dos fluídos, e geralmente é investigado com a utilização de experimentos em laboratório e simulações computacionais. Eles fornecem informações importantes para a avaliação das permeabilidades relativas e da saturação das fases existentes em um escoamento imiscível, o qual é predominantemente governado por forças capilares e viscosas relacionadas pelo número capilar.

Contribuições da comunidade científica mostram que o aumento do número capilar tem um efeito positivo na eficiência da recuperação. No entanto, este efeito pode ser sensível a vários parâmetros, tais como a razão de viscosidade, a molhabilidade e a geometria e heterogeneidade do meio.

O presente trabalho investiga o efeito do número capilar na saturação residual das fases molhante e não molhante durante processos de drenagem. Um modelo imiscível de Lattice Boltzman baseado no modelo de gradiente de cor é utilizado para simular o escoamento em modelos porosos 2D e 3D de rochas porosas. As razões de densidade e viscosidade e a condição de molhabilidade são fixas para todos os casos. Os valores da viscosidade e da tensão interfacial são consistentes com o modelo e garantem estabilidade computacional das simulações. O número capilar é variado ao se definir diferentes valores de velocidade na entrada do domínio computacional.

Os resultados mostram a evolução da drenagem nos modelos à medida que a fase não molhante invade os poros estreitos, forçando o fluido molhante a deixar o meio poroso através da saída. Diferentes padrões são observados dependendo do valor do número capilar e do grau de porosidade e heterogeneidade dos meios porosos. Eventos em escala de poro, como os saltos de Haines, são observados e desempenham um papel importante no aprisionamento do fluido molhante.

A saturação da fase molhante é medida nos estados de ruptura e quase permanente e plotada em função do número capilar. Nos modelos 2D, o efeito da baixa velocidade do fluido com Ca baixo fornece uma melhor condição para a redistribuição do fluido, causando uma menor saturação residual do fluido molhante. Nos modelos 3D, um valor mais baixo de Ca leva ao aprisionamento do fluido molhante principalmente por causa da geometria do meio. Em todos os casos, a faixa mais alta de Ca resultou na menor saturação residual do fluido molhante. Observa-se também que o grau de heterogeneidade nos modelos 3D tem um efeito importante na saturação residual após a drenagem, e parece ser mais significativo que a porosidade ou permeabilidade intrínseca dos modelos.

A permeabilidade relativa no ponto de saturação irredutível da fase molhante é calculada para cada valor de Ca utilizado. À medida que a saturação irredutível do fluido molhante aumenta, a permeabilidade relativa do fluido molhante também aumenta, enquanto o oposto ocorre com a permeabilidade relativa do fluido não molhante.

Os resultados encontrados contribuem para a compreensão do escoamento imiscível em meios porosos e para a avaliação de curvas completas de permeabilidade relativa e dessaturação capilar de rochas porosas.

Palavras-chave: meios porosos, número capilar, saturação residual, drenagem, Lattice Boltzmann

RESUMO EXPANDIDO

Introdução

A recuperação aprimorada de petróleo de reservatórios não convencionais requer a compreensão da dinâmica do deslocamento de fluidos imiscíveis em meios porosos. Este é um fenômeno muito complexo devido a inúmeros fatores que influenciam o escoamento, incluindo características dos fluidos como densidade, viscosidade, tensão interfacial, molhabilidade, e características dos meios porosos como geometria de poros, distribuição de tamanho de poros, heterogeneidade, rugosidade da superfície, etc. Em geral, os métodos aprimorados de recuperação de óleo são projetados com o objetivo de aumentar o número capilar, que representa a razão entre as forças viscosas e forças capilares no sistema multifásico.

O fenômeno do escoamento imiscível em meios porosos geralmente é investigado com a utilização de experimentos em laboratório e simulações computacionais. Enquanto o primeiro método pode se tornar caro e geralmente é limitado, o segundo método se vê cada vez mais viável tecnicamente e financeiramente devido ao rápido aprimoramento de técnicas computacionais visto nos últimos anos. Em especial, o Método de Lattice Boltzmann (LBM) fornece várias vantagens distintas dentro dos métodos computacionais disponíveis, como a relativa facilidade de lidar com geometrias complicadas e a adaptação a uma programação paralela eficiente.

Tanto os métodos experimentais como computacionais são capazes de fornecer os dados necessários para análise do efeito de diferentes parâmetros, incluindo o número capilar, na investigação das permeabilidades relativas e da saturação das fases existentes. Estes dados fornecem a informação sobre a capacidade da rocha do reservatório em deixar os fluidos passarem através da mesma e a quantidade de fluido que fica aprisionado dentro do reservatório ao final de processos de drenagem ou embebição. Estes processos se caracterizam pelo fluido que é deslocado ou deslocante.

Grande parte das contribuições da comunidade científica mostra que o aumento do número capilar tem um efeito positivo na eficiência de deslocamento de drenagem, isto é, a saturação do fluido deslocado (fluido molhante) é menor ao final do processo quando o número capilar é maior. No entanto, este efeito pode ser sensível a vários parâmetros, tais como a razão de viscosidade entre fluidos, a condição de molhabilidade e a geometria e heterogeneidade do meio. Outro fator importante é o momento de medição da saturação final. Em muitos trabalhos da literatura é utilizado como momento de medição o ponto de ruptura, isto é, o ponto onde o fluido não molhante alcança a saída do meio poroso. Em outros casos, as medições são realizadas em estado permanente, quando não há mais variação da saturação de fluido não molhante com o tempo. Este momento pode ocorrer muito depois do ponto de ruptura e essa diferença pode representar uma grande variação no valor de saturação final dos fluidos.

Objetivos

O principal objetivo deste trabalho é avaliar a influência do número capilar na saturação residual das fases molhante e não molhante após processos de drenagem em meios porosos. Um modelo multicomponente de Lattice Boltzmann (LB) é utilizado para simular os processos de drenagem com diferentes valores de número capilar em modelos digitais 2D e 3D de meios porosos. As simulações são realizadas até o estado quase permanente, e várias características são capturadas e medidas durante os processos de drenagem. A saturação irredutível do fluido molhante é alcançada, que é basicamente o volume de fluido molhante aprisionado dentro do meio poroso. No estado quase permanente, são calculadas as permeabilidades relativas para as fases molhante e não molhante. Somente a drenagem é simulada devido à capacidade computacional disponível. Os modelos digitais utilizados são relativamente grandes, e a simulação de processos subsequentes de embebição é inviável no momento. No entanto, os resultados serão válidos para trabalhos futuros que possam investigar outros fenômenos do escoamento imiscível em meios porosos.

Metodologia

Um modelo Lattice-Boltzmann multicomponente baseado no modelo de gradiente de cor é utilizado, incluindo um esquema de dois tempos de relaxação para o operador de colisão. Um termo de força adicional é incluído no operador de colisão para simular a dinâmica da interface entre os fluidos. Ele é formulado com base em uma perturbação de tensão viscosa que promove um degrau de pressão entre os fluidos na região interfacial. Uma regra de segregação é incluída no processo de evolução de partículas em uma etapa pós-colisão, pré propagação, e finalmente a etapa de propagação é executada com um algoritmo de permutação. Para implementar a condição de molhabilidade em uma parede sólida, supõe-se que a parede sólida seja uma mistura de dois fluidos com proporções constantes com tempo.

O modelo LB é utilizado para simular drenagem em dois modelos porosos 2D e dois modelos 3D. O primeiro é um modelo 2D homogêneo produzido manualmente, composto por grãos circulares de diâmetros iguais, distribuídos espacialmente para obter razão entre garganta e poro constante no meio. O segundo modelo 2D consiste em uma fatia de uma imagem digital de um rocha do tipo arenito chamada LV60A, que também é utilizada para os modelos 3D. Os modelos digitais 3D são obtidos a partir de arquivos brutos de imagens de microtomografia computadorizada de um arenito Berea e do arenito LV60A, para os quais estão disponíveis na literatura dados experimentais de porosidade, permeabilidade intrínseca e relativa e saturação residual. A porosidade absoluta e a permeabilidade intrínseca de todos os modelos são obtidos por meio de simulações de escoamento monofásico.

As razões de viscosidade e densidade são iguais para todas as simulações. Os valores individuais de viscosidades, densidades e tensão interfacial foram escolhidos considerando três critérios: atingir o número capilar desejado, garantir a estabilidade das simulações e obter tempo prático para as simulações. O ângulo de contato é definido para obter uma condição fortemente não molhante do fluido invasor em relação ao sólido.

O número capilar é variado ao se definir diferentes valores para velocidade constante na entrada no meio. Cada simulação é realizada individualmente, com as mesmas condições iniciais e com número capilar fixo calculado usando a velocidade de entrada. Seis processos de drenagem individuais com diferentes Ca são realizados em cada meio poroso. O intervalo do Ca está entre 5×10^{-6} e 1×10^{-3}. Os valores mais baixos de Ca estão na faixa de *fingering* capilar, onde as forças capilares são a principal força, e os valores mais altos de Ca estão na zona de transição entre o *fingering* capilar e o deslocamento estável.

A condição de anti escorregamento é imposta em todos os nós sólidos, e nas laterais e nas faces superior e inferior é imposta a condição de contorno periódica. Na entrada, é imposta uma velocidade constante do fluido não molhante, e na saída é aplicada uma condição de contorno convectiva. Inicialmente, o meio poroso é totalmente saturado com fluido molhante. O fluido não molhante invade o meio poroso a partir da entrada. As simulações são executadas até o estado quase permanente, que é alcançado quando a saturação do fluido não molhante se torna praticamente constante ao longo do tempo.

Resultados e Discussão

O modelo multicomponente de Lattice Boltzmann foi aplicado em testes de preenchimento capilar e teste de bolha. A força interfacial e a condição de contorno de molhabilidade mostraram boa consistência com os efeitos esperados de molhabilidade e capilaridade. A condição de contorno convectiva implementada fornece similaridade física razoável e estabilidade de fronteira. Nos processos de drenagem nos meios porosos, o modelo multicomponente foi capaz de recuperar com qualidade a dinâmica dos fluidos durante a drenagem. Vários aspectos foram observados, como os padrões de deslocamento e os mecanismos em escala de poro, que são semelhantes às observações encontradas na literatura.

Os eventos em escala de poro no regime capilar, como os saltos de Haines, são um importante mecanismo de aprisionamento durante a drenagem. Em todos os casos simulados, eles ocorrem com frequência, especialmente com baixos valores do Ca, e são mais intensos em geometrias com maior razão entre tamanhos de garganta e poro. Nos modelos 2D, esses mecanismos podem levar a uma maior saturação residual de fluido molhante em valores intermediários de Ca, devido à alta velocidade do fluido. Nos modelos 3D, o efeito depende da conectividade dos poros e do grau de heterogeneidade.

Caminhos preferenciais para o escoamento são observados durante a drenagem nos modelos 2D e 3D. Eles fornecem a pressão capilar mais baixa necessária para o fluido não molhante escoar até a saída. Nos modelos 3D, é possível encontrar mais de um caminho, dependendo da conectividade dos poros. Em meios de baixa conectividade, como a rocha Berea, o caminho preferencial é mais claro e tem mais efeito sobre a saturação no ponto de ruptura. Além disso, durante a drenagem, o caminho preferencial pode ser afetado pelos mecanismos em escala de poro, e isso leva a diferentes caminhos preferenciais entre regimes de escoamento distintos.

A saturação residual de fluido molhante (S_w) no estado de ruptura e quase permanente é altamente dependente do número capilar. Um valor mais baixo do Ca leva a um maior aprisionamento de fluido molhante nos modelos 3D, principalmente por causa das geometrias dos meios. Nos modelos 2D, a baixa velocidade do fluido a baixo Ca forneceu uma melhor condição para a redistribuição do fluido, causando uma menor saturação residual do fluido molhante. Em todos os casos, os maiores valores do Ca resultaram em uma menor S_w.

O grau de heterogeneidade nos modelos 3D tem um efeito importante na saturação residual após a drenagem. A rocha LV60A possui uma ampla distribuição de tamanho dos poros, com mais poros sem saída e poros e gargantas pequenos, o que aumenta a quantidade de aprisionamento de fluido molhante. A rocha da Berea tem menor porosidade e permeabilidade intrínseca, mas o grau de heterogeneidade é menor que na LV60A. Isso leva a uma maior eficiência de varredura da drenagem e maior permeabilidade relativa no mesmo valor de Ca usado na drenagem. A rocha LV60A possui maior porosidade e permeabilidade intrínseca, o que resulta em maior permeabilidade relativa para o mesmo nível de saturação.

No alto nível de saturação de fluido não molhante atingido no estado quase permanente com modelos 3D, as permeabilidades relativas para os fluidos molhante e não molhante têm uma relação linear com a saturação. À medida que a saturação irredutível do fluido molhante aumenta, a permeabilidade relativa para o fluido molhante também aumenta, enquanto o oposto ocorre com a permeabilidade relativa para o fluido não molhante.

Considerações Finais

A investigação realizada no presente trabalho é um primeiro passo no estudo da eficiência

de recuperação em meios porosos reais. Trabalhos futuros podem se beneficiar dos resultados e condições finais do presente trabalho. Por exemplo, deslocamentos de embebição e subsequentes processos de drenagem podem ser simulados usando as distribuições de fluido obtidas no estado final. Isso permite o cálculo de curvas completas de permeabilidade relativa e curvas de dessaturação capilar, que são os principais insumos para decisões na indústria de recuperação de petróleo.

Além disso, este trabalho mostrou o potencial do LBM para o cálculo de escoamento imiscível em geometrias complexas. O método é uma ferramenta importante para a avaliação de propriedades relevantes de deslocamento imiscível em meios porosos. Devido à capacidade computacional, não foi possível simular valores adicionais do Ca ou investigar outros parâmetros relevantes. Entretanto, a metodologia apresentada neste trabalho fornece uma ferramenta eficiente para calcular curvas completas de permeabilidade relativa e curvas de dessaturação capilar para drenagem e embebição usando uma variedade de parâmetros. Com o atual desenvolvimento da tecnologia computacional e das técnicas de modelagem, o estudo do deslocamento imiscível é consideravelmente beneficiado. Eventualmente, trabalhos futuros podem introduzir novos detalhes sobre a recuperação de petróleo, simulando a rocha completo do reservatório com propriedades reais medidas no local.

Palavras-chave: meios porosos, número capilar, saturação residual, drenagem, Lattice Boltzmann

ABSTRACT

Oil recovery from unconventional reservoirs relies on the comprehension of the dynamics of immiscible displacement in porous media. This is a complex phenomenon in fluid mechanics, and it is usually investigated with laboratory experiments and computational simulations. They provide important information for the evaluation of relative permeabilities and saturation of existing phases in a immiscible flow, which is predominantly governed by viscous and capillary forces related by the capillary number.

Contributions of the scientific community show that the increase in capillary number has a positive effect on fluid recovery efficiency. However, this effect can be sensitive to several parameters such as viscosity ratio, wettabillity and the medium geometry and heterogeneity.

The present work investigates the effect of the capillary number on the residual saturation of wetting and nonwetting phases during processes of drainage. A multiphase Lattice Boltzmann model based on the color gradient model is used to simulate the flow in 2D and 3D digital models of porous rocks. Density and viscosity ratios and wettability condition are fixed for all cases. The values of viscosity and interfacial tension are consistent with the model and ensure computationally stable simulations. The capillary number is varied by setting different values of the inlet velocity at the entrance of the computational domain. The results show the evolution of drainage in the models as the nonwetting phase invades the narrow pores, forcing the wetting fluid to leave the porous medium through the outlet. Different patterns are observed depending on the value of capillary number and the degree of porosity and heterogeneity of the porous media. Pore-scale events such as Haines jumps are observed and play an important role in the trapping of wetting fluid.

The wetting phase saturation is measured at breakthrough and quasi-steady states and plotted as a function of the capillary number. In 2D models, the effect of the low velocity of the fluid at low Ca provides a better condition for fluid redistribution, causing a lower residual wetting fluid saturation. In 3D models, a lower value of Ca leads to more trapped wetting fluid mainly because of the media geometries. In all cases, the highest Ca range resulted in the lowest residual wetting fluid saturation. It is observed that the degree of heterogeneity in 3D models has an important effect on the residual saturation after drainage, which seems to be more significant than porosity or intrinsic permeability of the models.

The relative permeability at the point of irreducible wetting phase saturation is calculated for all Ca cases. As the irreducible wetting fluid saturation increases the relative permeability for the wetting fluid also increases, while the opposite occurs with the relative permeability for the nonwetting fluid.

Those findings contribute for the comprehension of two phase flow in porous media and for the evaluation of complete curves of relative permeability and capillary desaturation of porous rocks.

Keywords: porous media, capillary number, residual saturation, drainage, Lattice Boltzmann

LIST OF FIGURES

LIST OF TABLES

LIST OF ABBREVIATIONS AND ACRONYMS

EOR	Enchanced oil recovery
CDC	Capillary desaturation curves
MF	Microfuidic
CFD	Computational fluid dynamics
LBM	Lattice Boltzmann Method
CT	Computed tomography
LB	Lattice Boltzmann
REV	Representative elementary volume
CA	Cellular automaton
LGCA	Lattice gas cellular automata
$D2Q9$	Lattice configuration with 2 dimensions and 9 velocities
LBE	Lattice Boltzmann Equation
BGK	Collision operator developed by Bhatnagar, Gross and Kook
$D3Q19$	Lattice configuration with 3 dimensions and 19 velocities
RK	Rothman and Keller (1988) multiphase model
SC	Shan and Chen (1993) multiphase model
SCMP	Single-component multiphase model
EOS	Equation of state
MCMP	Multi-component multiphase model
FE	Free-energy multiphase model of Swift et al. (1996)
HCZ	He, Chen and Zhang (1999) multiphase model
BT	Breakthrough
QS	Quasi-steady
VOF	Volume of fluid
PV	Pore volume
UNK	Unknown

LIST OF SYMBOLS

ϕ	Porosity
ϕ_a	Absolute porosity
ϕ_e	Effective porosity
V_V	Volume of void spaces
V_T	Total bulk volume
V_C	Volume of the interconnected void spaces
k	Intrinsic permeability
Q	Volumetric flow rate or discharge
A	Normal cross-sectional area
μ	Fluid dynamic viscosity
L	Length in the macroscopic flow direction
Δp	Hydrostatic pressure drop
σ	Interfacial tension
θ	Contact angle
p_c	Capillary pressure
R	Capillary tube radius
p_{nw}	Pressure in the nonwetting fluid
p_w	Pressure in the wetting fluid
Ca	Capillary number
V	Characteristic velocity of the fluid
M	Viscosity ratio
S_w	Wetting fluid saturation
S_{nw}	Nonwetting fluid saturation
S_{wi}	Irreducible saturation of the wetting fluid
S_{nwr}	Residual saturation of nonwetting fluid
k_{rj}	Relative permeability to the fluid j
k_j	Effective permeability to the fluid j
k_{rnw}	Relative permeability to the nonwetting fluid
k_{rw}	Relative permeability to the wetting fluid
f_i	Particle distribution function
$\mathbf{x}$	Particle position
t	Time
$\mathbf{c}_i$	Particle velocity
b	Maximum number of possible velocity directions
Δt	Timestep
$\Delta \mathbf{x}_i$	Distance between two orthogonal nodes
ρ	Density

$\mathbf{u}$	Macroscopic velocity
Ω_i	Collision operator
τ	Relaxation time
f_i^{eq}	Local equilibrium distribution of particles
w_i	Weight in direction i
$u_{\alpha(\beta)}$	$\alpha(\beta)$ component of the velocity vector $\mathbf{u}$
p	Thermodynamic pressure
ν	Kinematic viscosity
c_s	Speed of sound in lattice units
$\mathbf{a}_g$	Gravitational acceleration
l	Linear dimension
N	Number of lattice nodes
δ_x	Equivalent of the lattice space in centimetres
δ_t	Equivalent of the timestep in seconds
μ_F	Dynamic viscosity in physical units
μ_{LB}	Dynamic viscosity in lattice units
σ_{LB}	Interfacial tension in lattice units
σ_F	Interfacial tension in physical units
ρ_F	Physical specific mass
δ_m	Mass of a node in grams
R_i	Red fluid distribution function
B_i	Blue fluid distribution function
ρ^N	Phase field
ρ_R	Red fluid density
ρ_B	Blue fluid density
f_s	Symmetric part of the distribution function
f_s	Antisymmetric part of the distribution function
$f_{s,i}^{eq}$	Equilibrium distribution for the symmetric part of the distribution function
$f_{a,i}^{eq}$	Equilibrium distribution for the antisymmetric part of the distribution function
τ_s	Relaxation time for the symmetric part of the distribution function
τ_a	Relaxation time for the antisymmetric part of the distribution function
F_i	Force term for the interfacial tension
∇w_r	Gradient of red fluid saturation for each direction of a lattice node
$\mathbf{n}$	Unit vector normal to the interface between phases
δ_{mn}	Kronecker delta
α	Coefficient proportional to the emerging interfacial tension between phases
β	Recolouring coefficient that controls the interface width
w_{wr}	Concentration of red fluid at the wall
θ_r	Contact angle to the red fluid
u_x	x component of velocity $\mathbf{u}$

R^2	Coefficient of determination

CONTENTS

1 INTRODUCTION

In the past 10-20 years, unconventional oil and gas sources have become a large supplier of energy worldwide. Moreover, it is predicted that in the next 20-50 years these sources will increase in prominence and play a significant and vital role in the energy budget (HONGJUN et al., 2016).

Unconventional reservoirs usually consist of porous rocks with complex geometry, low porosity and low permeabilities. The pore structure is characterized by a large range in pore sizes from the order of nanometres to microns (YEKEEN et al., 2019). Enhanced oil recovery (EOR) methods are specially designed to increase oil recovery during secondary and tertiary stages, and depend on the comprehension of the dynamics of fluid flow inside these complex structures. The scientific challenge lies in the physics of multiphase immiscible flow in porous media. This is a common environmental phenomenon and it is important for many industrial problems, such as enhanced oil recovery, geological carbon dioxide sequestration, fuel cells, groundwater supply and remediation and catalytic processing in fixed bed reactors.

An immiscible system of a reservoir usually consists of water and hydrocarbons in liquid and/or gaseous phase enclosed in a solid porous media (BEAR, 1972). The dynamics of this multiphase system is very complicated due to numerous factors influencing the flow, including fluid characteristics such as density, viscosity, interfacial tension, wettability, and porous media characteristics such as pore geometry, pore size distribution, heterogeneity, surface roughness, etc.

EOR methods often aim to increase the capillary number, which represents the balance between viscous and capillary forces in the multiphase fluid-rock system, either by decreasing the interfacial tension between phases (surfactant injection) or by increasing the viscosity of the injected phase (polymer injection). The impact of a particular EOR approach on sweep efficiency can be observed in a capillary desaturation curve (CDC), which shows the influence of the capillary number on remaining phases and hence help to reduce uncertainty during the planning and execution of a project (XU et al., 2018).

A traditional method for analysis of flow in porous media is the Darcy's law and its modifications for multiphase flows. Basically, Darcy's law allows the calculation of the medium permeability (or relative permeability for multiphase flow), which indicates, in general terms, the ability of the porous medium to transmit fluids. Another parameter of great importance is the volume of residual oil trapped in the porous medium after the processes of displacement of oil and/or water (usually the nonwetting and wetting phases, respectively). This is influenced by the characteristics of the porous medium and the flow dynamics, and can result in a significant loss of oil during the extraction in a reservoir.

Darcy's law does not allow the evaluation of important parameters, such as capillary number, viscosity ratio and wettability, and their effects on the relative permeability and residual oil saturation. To investigate those effects, advanced methods with pore-scale view capacity are required, such as laboratory experiments with rock samples, microfluidic (MF) technology or computational simulations, which can yield the relationship between phase saturation, fluid pressure and relative permeability.

Accurate determination of those relationships for petroleum reservoirs is a difficult and expensive process, which usually involves performing laboratory experiments on rock cores that are specially cut during the drilling process of the well. The cores must be carefully selected to provide an accurate representation of the entire reservoir rock. Retrieval of such cores is expensive and usually limited. Moreover, the laboratory experiments may not always reflect the actual subsurface conditions (WARDA et al., 2017).

An alternative approach to analyze the multiphase flow in such systems is the use of advanced simulation tools such as computational fluid dynamics (CFD) and pore-scale modelling techniques. Conventional CFD methods based on Navier-Stokes equations and the classical continuum approach require a highly refined grid and huge computational resources to capture the underlying flow physics in porous media. To overcome these limitations, a considerable development in non-conventional techniques, such as the Lattice Boltzmann Method (LBM), has been observed in recent years.

LBM is based on a mesoscopic scale approach, which allows the method to capture physical phenomena on the microscopic scale and translate them into macroscopic scale parameters, within manageable and efficient use of computer resources. Unlike conventional CFD methods, LBM focuses on solving the Boltzmann transport equation, which is known to be equivalent to the Navier-Stokes equation (SUCCI, 2001). LBM provides several distinct advantages, such as the relative ease of handling complicated geometries and adaptation to efficient parallel programming, and it is now commonly applied to analyze multiphase flow in complex porous media. The inputs for these computations are digital representations of the porous medium which usually comes from computed tomography (CT) scans (MOHAMAD, 2011).

In this work, a Lattice Boltzmann (LB) multiphase model is used to simulate the drainage displacements with different values of capillary number in 2D and 3D digital models of porous media. Simulations are carried out until quasi-steady state, and several characteristics are captured and measured during the drainage processes. The irreducible saturation of wetting fluid is achieved, which is basically the volume of wetting fluid trapped inside the porous medium. At quasi-steady state, the relative permeabilities for the wetting and nonwetting phases are calculated.

Only drainage is simulated due to computational capacity available. The digital models used are relatively big, and simulate subsequent processes of imbibition is unfeasible at this time. However, the results will be valid for future works which may investigate other phenomena of multiphase flow in porous media.

1.1 OBJECTIVES

1.1.1 General Objective

The main objective of this work is to evaluate the influence of the capillary number on the residual saturation of wetting and nonwetting phases after drainage processes in porous media, using a computational method based on a Lattice Bolztmann multiphase model.

1.1.2 Specific objectives

The following specific objectives were established to develop and present the current work in the best possible way:

(i) review the classical literature on relevant topics of porous media and multiphase flow with the support of recognized references;

(ii) study and compile the basic concepts of the Lattice Boltzmann Method and well-known single and multiphase models;

(iii) investigate and discuss the state of the art, addressing recent publications on multiphase flow in porous media, with special attention to publications on pore-scale mechanisms and residual saturation during drainage;

(iv) define, analyze and explain the novel LB multiphase model, the rules for collision and streaming and the implementation of interfacial tension and wettability;

(v) verify the consistency of the LB multiphase model in reproducing wettability, capillarity and boundary physics using well-known tests;

(vi) produce and/or select and examine digital models of porous media, and compute the porosities and intrinsic permeabilities;

(vii) carry out simulations of drainage in the selected digital models at different capillary numbers with the LB model;

(viii) analyze and discuss the results, confronting with expected physical phenomena and/or literature observations;

(ix) validate the results with the objectives and premises of the work;

(x) review the main contributions of this work for the development of the subject in the scientific community, provide a lessons-learned and indicate possible future works to be developed with the methodology and contributions of this work.

2 LITERATURE REVIEW

This chapter is dedicated to a literature review on the fundamental topics required for fully understanding of the work and the state of the art on the main subjects addressed in the next chapters.

Section 2.1 outlines the aspects of the fluid flow in porous media: the characterization of the porous media and relevant parameters, the concepts of fluid mechanics governing the flow and important aspects of immiscible displacement regarding capillary mechanisms and phase saturation inside a porous medium.

Section 2.2 introduces the Lattice Boltzmann Method: the concepts of particle distribution function, the main equations for collision and propagation, implementation of boundary conditions, and an introduction on multiphase models.

The last section presents a review of the state of the art on the main subject of this work, providing an insight on recent publications that apply the LBM or experimental methods to evaluate the influence of capillary number on the immiscible displacement in a porous medium.

2.1 FLUID FLOW IN POROUS MEDIA

This section covers the main characteristics of fluid flow in porous media, specially for immiscible displacement in capillary systems. The porous medium is characterized and the relevant parameters for fluid flow are explained. In the following, the basic aspects of multiphase flow such as wettability and capillarity are described. Finally, the mechanisms of immiscible displacement are explained focusing on the relationship of phase saturation and capillarity.

2.1.1 The porous medium

Porous materials can be found in everyday life, in technology and in nature. With the exception of metals, some dense rocks, and some plastics, virtually all solid and semi-solid materials are porous to varying degrees. A material or structure must have these two characteristics to be qualified as a porous medium (DULLIEN, 1992):

(i) it must contain spaces, so-called voids or pores, free of solids, embedded in the solid or semi-solid matrix. The pores usually contain some fluid, such as air, water, oil or a mixture of different fluids;

(ii) it must be permeable to a variety of fluids, i.e., fluids should be able to penetrate through one face of a sample of material and emerge on the other side.

Fluid flow in porous media is strongly influenced by pore structure parameters. Macroscopic pore structure parameters represent average behaviour over a representative elementary volume (REV), which is the smallest volume over which a measurement can be made that yields a value representative of the whole sample (BEAR; BACHMAT, 2012).

A basic pore structure parameter is the porosity (ϕ). From the standpoint of flow through porous media, it is possible to define two distinct types of porosity: absolute

(ϕ_a) and effective (ϕ_e) porosity. The absolute porosity is defined as the ratio between the volume occupied by pores or void spaces (V_V) and the total bulk volume (V_T). However, many of the void spaces are not interconnected and do not contribute effectively to the flow. Thus, it is more common to use the concept of effective porosity, which is the ratio between the volume occupied by interconnected void spaces (V_C) and the total bulk volume (V_T). Both types of porosity can be determined by several established experimental methods.

An important porous media parameter is the permeability (k), also called specific or intrinsic permeability since it is an intensive property of the porous medium. It is a measure that indicates the ability of a porous medium to allow fluids to pass through it. The permeability of a medium is influenced by the material, the porosity, the shapes of the pores in the medium and their level of connectivity. It was first defined mathematically by Henry Darcy in 1856. In steady unidirectional flow and at low Reynolds number, Darcy's law is written as

$$Q = \frac{kA}{\mu}\left(\frac{\Delta p}{L}\right), \tag{2.1}$$

where Q is the volumetric flow rate (discharge), A is the normal cross-sectional area of the medium, μ is the fluid dynamic viscosity, L is the length of the medium in the macroscopic flow direction and $\Delta p \equiv p_1 - p_2$ is the hydrostatic pressure drop (BEAR, 1972).

Although Darcy's law is simple and efficient, it is valid essentially for single component, steady and incompressible flow at low Reynolds number. Many improvements using mathematical and empirical approaches were proposed trying to overcome the limitations of Darcy's law (INGHAM; POP, 1998).

There are several other macroscopic and microscopic pore structure parameters such as specific surface area, pore size distribution and compressibility, which are important to related studies in porous media. Dullien (1992) and Bear (1972) are two outstanding works that provide detailed descriptions of porous media characteristics.

2.1.2 Multiphase flow in porous media

In the previous section, the relevant parameters of porous media were defined in terms of a single-component system. Simultaneous presence of two or more fluids in the porous medium requires defining new properties such as interfacial tension, wettability and capillarity.

2.1.2.1 Interfacial tension and wettability

When two immiscible fluids are in contact, they are separated by a thin layer or transition zone of small thickness called interface (when two liquids) or surface (when liquid and gas) (DULLIEN, 1992). In this interface, a tension arises from the difference of intermolecular forces acting on molecules at the interface. In the bulk of the fluid, each molecule is pulled equally in every direction by neighbouring-like molecules, resulting in zero net force. The molecules at the surface do not have neighbouring-like molecules on all sides and therefore are pulled inwards. This creates internal pressure and forces fluid surfaces to contract to a minimal area. The unbalanced attraction force between the molecules creates the interfacial tension (σ) (BEAR; BACHMAT, 2012).

Figure 1 illustrates two immiscible fluids over a solid surface and between two parallel plates or inside a capillary tube. The equilibrium configuration of the fluid phases depends on the relative values of the interfacial tension between each pair of the three phases. Each interfacial tension acts upon its respective interface defining the contact angle (or wetting angle) θ, which is the angle between the interface AB and the interface SA (BEAR; BUCHLIN, 1991). In an equilibrium state, the tensions must also be in equilibrium, which results in

$$\sigma_{AB}\cos\theta = \sigma_{SB} - \sigma_{SA}. \tag{2.2}$$

Equation 2.2 is called Young-Dupré equation and relates the contact angle with the interfacial tensions.

Figure 1: Interfacial tension and contact angle in an immiscible system over a solid surface (a) and inside a capillary tube (b).

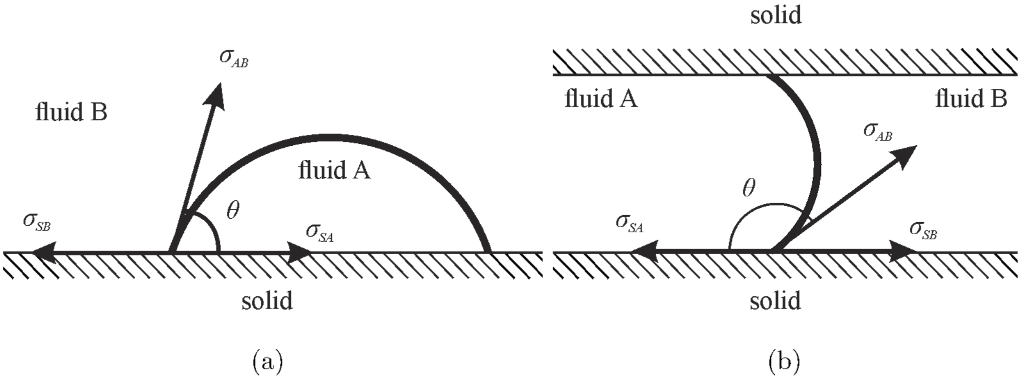

Source: elaborated by the author.

The contact angle θ is a measure of wettability, which is defined as the tendency of one fluid to spread on or adhere to a solid surface in the presence of other immiscible fluids. In Figure 1 the wetting characteristics of fluid A and B change as the contact angle increases. Fluid A is said to be the wetting fluid when $\theta < 90°$, and B is the nonwetting fluid (Figure 1(a)). This means that fluid A has higher tendency to adhere to the solid surface compared to fluid B. If $\theta > 90°$, A is said to be the nonwetting phase and B the wetting phase (Figure 1(b)). When $\theta = 90°$, there is an equal tendency of both fluids to "wet" the solid surface (GENNES; BROCHARD-WYART; QUÉRÉ, 2013).

The interfacial tension, contact angle and wettability are extremely relevant in capillary systems such as those present in porous media. However, the evaluation of these parameters in real systems is very difficult because of the intrinsic characteristics of the solid surface and the fluids. Surface roughness, heterogeneity and contamination are among the aspects that contribute to uncertainties during measurements (DULLIEN, 1992).

2.1.2.2 Capillarity

At least three phases are involved in an immiscible system as illustrated in Figure 1: the wetting phase, the nonwetting phase and the solid phase. A discontinuity in pressure rises between the two fluids deriving from interfacial tensions and the curvature of the interface separating the fluids. This difference existing across the interface is called capillary pressure (p_c), which is defined as the pressure difference between the nonwetting and wetting phases (BEAR; BACHMAT, 2012). For the case of an immiscible system in a capillary tube illustrated in Figure 1(b), the capillary pressure can be calculated by the Young-Laplace equation (BEAR, 1972):

$$p_c = p_{nw} - p_w = \frac{2\sigma \cos\theta}{R}, \tag{2.3}$$

where σ is the interfacial tension, θ is the contact angle and R is the capillary tube radius. p_{nw} and p_w are the pressure of the nonwetting and the wetting fluids, respectively.

The capillary pressure depends on the geometry of the void spaces within the porous medium, the nature of fluids and solids and the degree of phases saturation. Due to the irregular geometry of real porous media, the problem is more complex and cannot be described analytically. Idealized models of the pore space such as capillary tubes, packing spheres or parallel circular rods are adopted in order to obtain analytical solutions for the capillary pressure curves as a function of phase saturations. Laboratory experiments or computational methods can be employed to obtain those curves for immiscible displacement in complex porous media (BEAR, 1972).

The displacement of one fluid by another in the pores of a porous medium is either aided or opposed by the capillary pressure. In order to maintain a porous medium partially saturated with nonwetting fluid while the medium is also exposed to wetting fluid, it is necessary to maintain the pressure of the nonwetting fluid at a value greater than that in the wetting fluid. Moreover, Equation 2.3 shows that capillary pressure is inversely proportional to the capillary tube diameter. This means that the nonwetting fluid pressure must be higher in thinner capillary tubes in order to maintain an equilibrium state. This condition has important consequences in the dynamics of immiscible displacement, as will be seen in section 2.3.

Considering the immiscible displacement in thin capillary tubes inside porous media without the action of gravity, two forces play major roles: capillary and viscous forces. It is possible to relate these forces by a nondimensional parameter called the capillary number, which is defined as the ratio between viscous forces and capillary forces (GENNES; BROCHARD-WYART; QUÉRÉ, 2013):

$$Ca = \frac{\mu V}{\sigma}, \tag{2.4}$$

where μ is the dynamic viscosity of the displacing fluid, V is a characteristic velocity and σ is the interfacial tension between the fluids. A high value of Ca means that the flow is dominated by viscous forces, while low values indicate the predominance of capillary forces. The crossover value usually lies within 10^{-5} and 10^{-4} (CHATZIS; MORROW, 1984).

Another important dimensionless number is the ratio M between injected fluid viscosity and displaced fluid viscosity. For certain values of Ca and M, either viscous or capillary forces dominate the flow, and phenomena of viscous and capillary fingering may occur (see section 2.3).

2.1.2.3 Two-phase immiscible displacement

In the two phase immiscible system illustrated in Figure 2, it is possible to distinguish three saturation states depending on the saturation of the wetting phase (S_w). At very low wetting phase saturation, wetting fluid forms rings called pendular rings around the grain contact points. At this state, the rings are isolated and do not form a continuous wetting phase. Practically no pressure can be transmitted from one ring to the next within the wetting phase. As the wetting phase saturation increases, the pendular rings expand until a continuous wetting fluid phase is formed. The saturation at which this occurs is called equilibrium saturation to the wetting phase. Above this critical saturation, the saturation is called furnicular and the flow of the wetting phase is possible. As the saturation of the wetting fluid increases, the nonwetting fluid is no longer a continuous phase, but consisted of individual droplets lodged in the larger pores. The nonwetting phase saturation (S_{nw}) at this point is called insular saturation. A globule of this type can move only if a pressure difference sufficient to squeeze it through capillary restrictions is applied (BEAR; BACHMAT, 2012).

Figure 2: Possible wetting fluid saturation states: (a) pendular rings; (b) equilibrium; (c) furnicular.

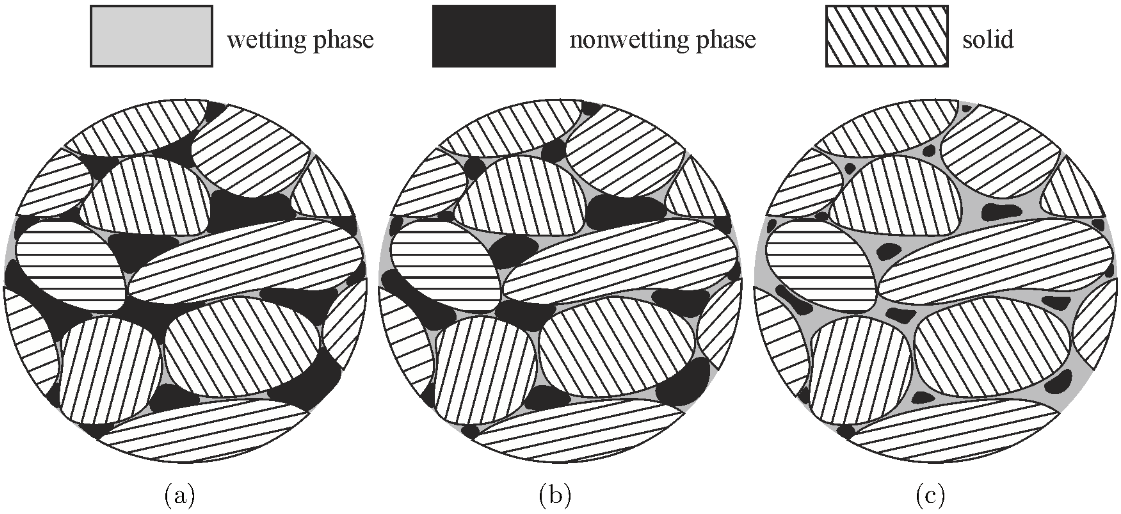

(a) (b) (c)

Source: adapted from Bear (1972).

In the dynamics of immiscible displacement, there are two major process that are characterized by the phase saturation: drainage and imbibition. When a sample is initially saturated with a wetting phase that is displaced by the nonwetting phase, the process is called drainage. The inverse process, by which the wetting fluid displaces a nonwetting fluid that initially saturates a porous medium sample, is called imbibition. When this phenomena occurs only by capillary forces without the application of pressure in the wetting fluid the process is called spontaneous imbibition (BEAR, 1972).

Figure 3 shows a typical capillary pressure curve as a function of the wetting phase saturation. Initially, the sample is completely saturated by a wetting fluid and the nonwetting fluid is injected by slowly increasing the pressure, therefore characterizing a drainage process. A certain pressure must be reached in the nonwetting phase before the latter begins to penetrate the sample initially into the thicker pores, displacing the wetting phase. This minimum pressure is called threshold pressure (BEAR; BACHMAT, 2012).

As the capillary pressure increases, the saturation of wetting fluid decreases. A certain quantity of wetting fluid remains in the sample even at high capillary pressures. The saturation at this point is called irreducible saturation of the wetting fluid (S_{wi}).

Starting from this point, the imbibition curve is obtained by decreasing the pressure in the nonwetting fluid. The wetting phase saturation increases, and the nonwetting phase saturation decreases until it reaches the point of residual saturation of nonwetting fluid (S_{nwr}), at zero capillary pressure. This saturation indicates the amount of nonwetting

Figure 3: Typical capillary pressure - wetting fluid saturation curves during drainage and imbibition.

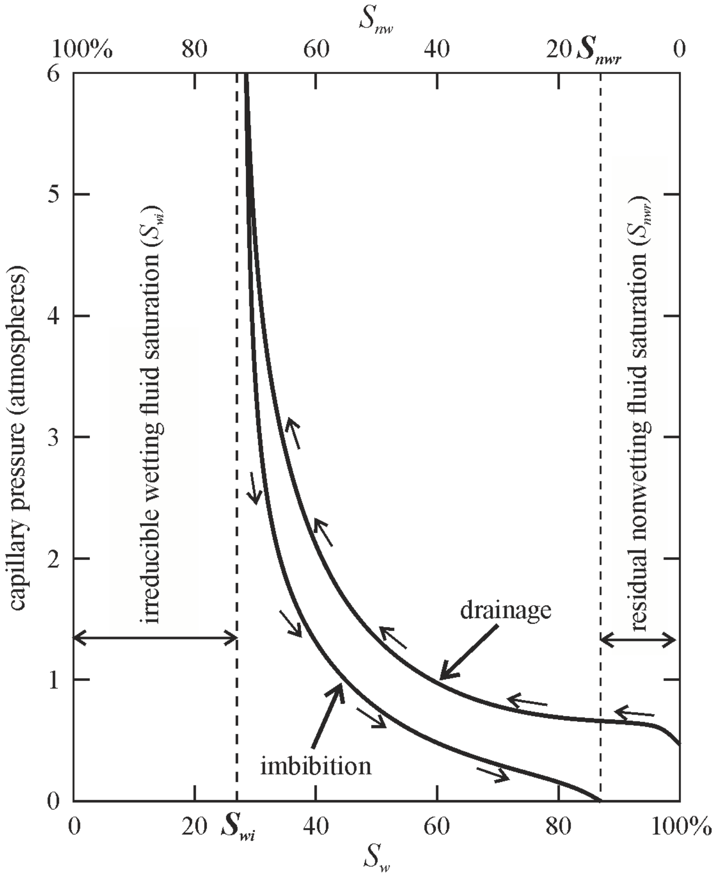

Source: adapted from Bear (1972).

fluid entrapped in the porous medium, i.e., below this level the nonwetting fluid ceases to flow (BEAR; BACHMAT, 2012).

In Figure 3, the drainage and imbibition curves are not the same. Because of the capillary hysteresis phenomena, different capillary pressure curves may be obtained depending on the saturation history. It has generally two causes: hysteresis of contact angle and pore structure effects (DULLIEN, 1992).

The contact angle θ is a function of the direction of the displacement (Figure 4). An advancing contact angle occurs in an imbibition process, where the wetting phase advances through the nonwetting phase. A receding contact angle occurs in a drainage process. Because of this phenomenon, it is not possible to determine the capillary pressure curves without knowing the past drainage-imbibition history of the sample considered (BEAR, 1972).

Several other aspects of immiscible displacement are covered in detail in section 2.3, such as capillary and viscous fingering, capillarity and viscosity effects on phase trapping and clustering, pore-scale mechanisms, etc.

2.1.2.4 Relative permeability

In multiphase flow in porous media, the relative permeability k_r of a phase is a dimensionless measure of the effective permeability of that phase, i.e., is a measure of

Figure 4: Contact angle in a capillary tube in a stationary state (θ), in an imbibition process (θ_1) and in a drainage process (θ_2).

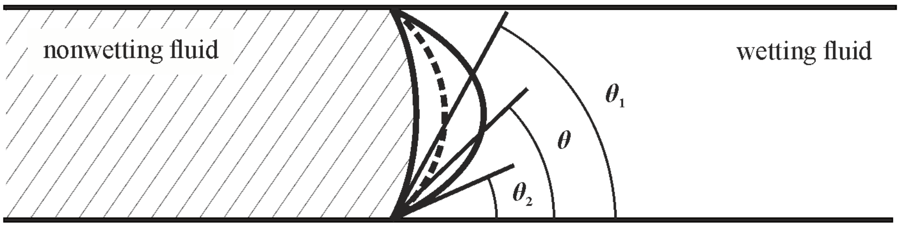

Source: adapted from Bear (1972).

conductance of the porous medium for one fluid phase in the presence of other fluid phases. It is not determined by the pore structure of the porous medium alone as the intrinsic permeability, but it depends also on the parameters of the multiphase system. Macroscopically, it can be described with an adaptation of Darcy's law (Equation 2.1) for multiphase flow (DULLIEN, 1992):

$$Q_j = \frac{k_{rj} k A}{\mu_j} \left(\frac{\Delta p_j}{L} \right), \qquad j = 1, 2. \tag{2.5}$$

k is the intrinsic permeability of the medium calculated with single phase flow and the value of the subscript j indicates which fluid is being considered. The effective permeability k_j of a phase in the multiphase flow is:

$$k_j = k_{rj} k. \tag{2.6}$$

The effective permeability is a function of fluid saturation, saturation history, wettability characteristics and pore geometry. In contrast to the intrinsic permeability, relative permeability for each phase is not a unique value and there is a specific relative permeability value for each saturation amount. It is usual to plot the relative permeability as a function of fluids saturation, as illustrated in Figure 5. The curves for drainage and imbibition are not the same because of the hysteresis effect. In drainage, as the nonwetting fluid saturation increases, the relative permeability to the nonwetting fluid (k_{rnw}) also increases while the relative permeability to the wetting fluid (k_w) decreases. The opposite occurs in imbibition, where the wetting fluid saturation increases during the process.

2.2 THE LATTICE BOLTZMANN METHOD

This section provides an introduction to the Lattice Bolztmann Method, which is the computational method used in this work to calculate the immiscible flow in the porous medium. Particular aspects of the model used in this work are discussed in details in the methodology chapter. This section presents a concise history of the method, the basic equations for the two dimensional single component model, boundary conditions and forcing methods, the conversion from lattice units to physical units, and an introduction on the popular models for multiphase flow calculation.

Figure 5: Illustration of relative permeability curves as function of phase saturation during drainage and imbibition.

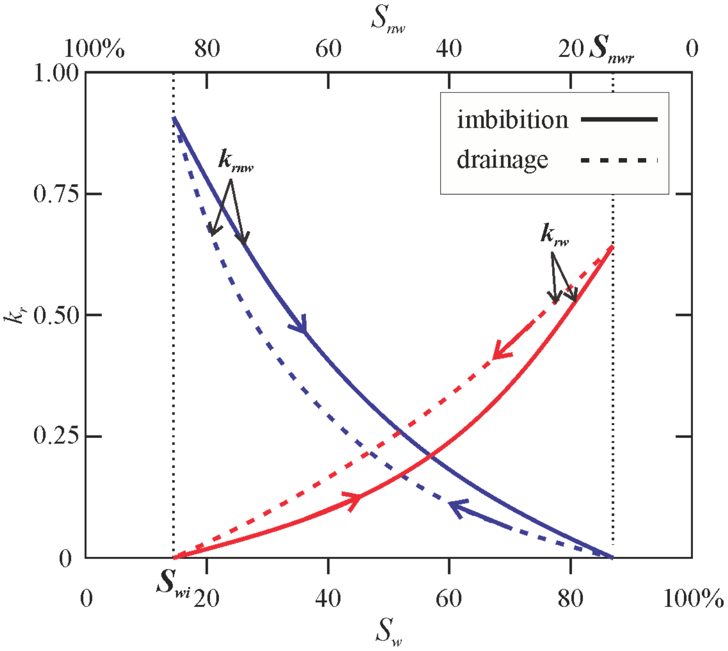

Source: adapted from Bear (1972).

2.2.1 History

The Lattice Boltzmann Method was introduced in the 1980s as a computational method for fluid dynamics calculation. The mathematical model is based in the Kinetic Theory of Gases and the simulation dynamics was adapted from a discrete algorithmic model called cellular automaton (CA).

Within the select group of scientists who dedicated themselves to the field of the Kinetic Theory of Gases, it is important to mention James C. Maxwell and Ludwig Boltzmann. Maxwell described the particle distribution function of gases on heuristic grounds, which was later generalized by Boltzmann who investigated the physical origins of the distribution and established the Maxwell-Boltzmann particle distribution function. Boltzmann also developed the Boltzmann transport equation to determine the evolution of the particle distribution function in a thermodynamic system. Their works were essential for the development of the Kinetic Theory of Gases and many other fields such as quantuum mechanics.

The Boltzmann transport equation was first implemented in a cellular automata algorithm at the same time by McNamara and Zanetti (1988) and Higuera and Jimenez (1989) and Higuera, Succi and Benzi (1989). They proposed the application of the transport equation in a lattice-gas cellular automata (LGCA) model, a precursor of the LBM that is also used for fluid dynamics calculation. Both methods, when analyzed in the macroscopic limit, are capable of satisfying the Navier-Stokes equations. However, LBM has the advantage of using a velocity distribution function on each node of the lattice instead of boolean variables. Furthermore, the LGCA produces intrinsic noise and requires greater effort to calculate macroscopic properties (WOLF-GLADROW, 2004).

After the works of McNamara and Zanetti (1988) and Higuera and Jimenez (1989), the application of the LBM for simulations in fluid mechanics expanded quickly. Several collision and boundary models were developed as well as methods for multiphase and multicomponent flow simulation.

The application of LBM for the analysis of flow in porous media was first proposed by Rothman (1988), who used a LGCA model to analyze flow in a 2D porous configuration. In another paper, Rothman and Keller (1988) introduced a collision rule that yields immiscible two-phase flow. Those works showed the potential of LBM for the investigation of flow through porous media, which is evident nowadays considering the great development observed in the last decades.

2.2.2 Single-phase Lattice-Boltzmann model

The Lattice Boltzmann Method is a mesoscopic method that describes a mechanical system of particles. It may be expressed as a discrete form of the Boltzmann transport equation, where the system is described by a particle distribution function $f_i(\mathbf{x}, t)$, which represents the probable number of particles in the position $\mathbf{x}$, at time t, with velocity $\mathbf{c}_i$. In LBM, the particles are confined to the nodes of a discrete cartesian lattice representing the space. Each group of particles are allowed to move in a finite number of directions b (Figure 6). Velocities are also discrete (since space and time are discretized) and limited by the directions of movement and number of lattice neighbours. Figure 6, for example, illustrates a $D2Q9$ lattice, with 2 dimensions and 9 possible velocities.

Figure 6: Illustration of a two dimensional lattice with nine possible velocities ($D2Q9$).

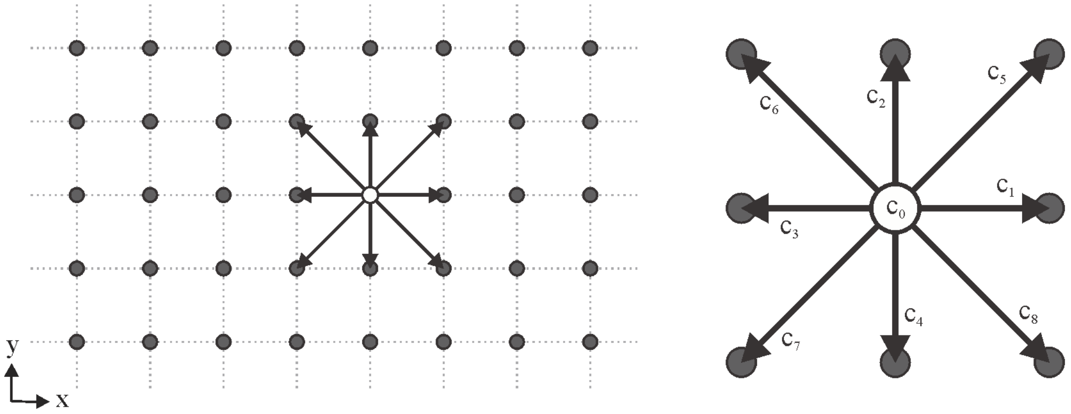

Source: elaborated by the author.

By considering Δt as the timestep and $\Delta \mathbf{x}_i$ as the distance between two orthogonal nodes, velocity may be defined as $\mathbf{c}_i = \Delta \mathbf{x}_i / \Delta t$. The time step ($ts$) and the distance between nodes (lattice unit or lu) are usually unitary. Consequently, in the $D2Q9$ lattice of Figure 6, the set of available velocities is $\mathbf{c}_i \in \{(0,0); (1,0); (0,1); (-1,0); (0,-1); (1,1); (-1,1); (1,-1); (-1,-1)\}$.

Each node of the lattice is populated by a particle distribution function $f_i(\mathbf{x}, t)$, which gives the number of particles at time t with velocity $\mathbf{c}_i$. The local macroscopic properties may be obtained from the distribution function. Usually, in LBM, the particle mass is assumed to be unitary, and is called mass unit or mu. Therefore, density and momentum are given by

$$\rho = \sum_i f_i \qquad \text{and} \qquad \rho \mathbf{u} = \sum_i f_i \mathbf{c}_i, \tag{2.7}$$

where f_i and $\mathbf{c}_i$ are functions of $\mathbf{x}$ and t, and i indicates the velocity direction ($i = 0, 1, ..., b$). Once the distribution function is known, the velocity and pressure field may be obtained. Pressure is a function of density and temperature at the node. For an isothermal gas, pressure depends only on density. Velocity $\mathbf{u}$ is given by

$$\mathbf{u} = \frac{\sum f_i \mathbf{c}_i}{\sum f_i}. \tag{2.8}$$

The evolution of the system of particles is characterized by two distinct stages: collision and streaming (Figure 7). The collision consists in the interaction of particles within each node individually, e.g., no information is exchanged between nodes. In the streaming step, the particle distribution is propagated from each node to neighbouring nodes, e.g., the post-collision distribution is transferred from the point $\mathbf{x}$ to the point $\mathbf{x}+\mathbf{c}_i$ (considering $\Delta t = 1$. Therefore, the LBM is an iterative method where in every time step there is a collision stage followed by a streaming stage. The equation that describes the evolution of the particle distribution is the Lattice Boltzmann Equation (LBE):

$$f_i(\mathbf{x} + \mathbf{c}_i, t + 1) - f_i(\mathbf{x}, t) = \Omega_i(\rho(\mathbf{x}, t), \mathbf{u}(\mathbf{x}, t)). \tag{2.9}$$

Figure 7: Evolution of the system of particles in one node.

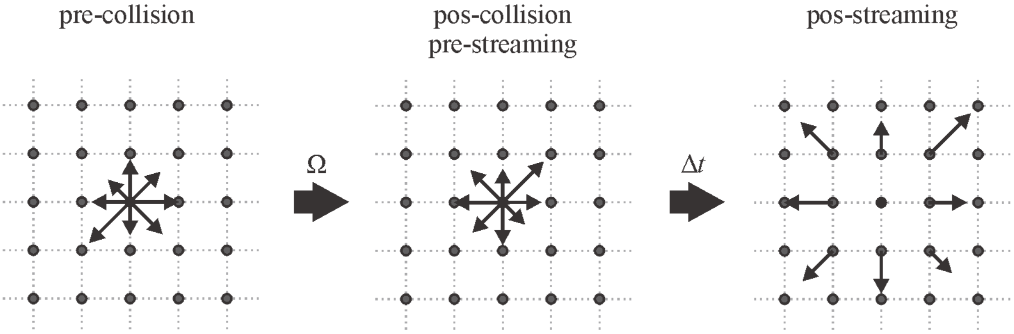

Source: elaborated by the author.

The left side of Equation 2.9 describes the streaming stage and the right side describes the collision stage. Although the stages can be combined into a single statement, they must be separated during the implementation. Ω_i is called collision operator and must be properly chosen to ensure that mass and momentum are conserved.

$$\sum_i \Omega_i = 0 \qquad \text{and} \qquad \sum_i \Omega_i \mathbf{c}_i = 0. \tag{2.10}$$

The simplest collision operator is the BGK, implemented in LBM by Qian, d'Humières and Lallemand (1992). It describes the collision as a process of relaxation to the local equilibrium state and is given by

$$\Omega_i = -\frac{1}{\tau}(f_i - f_i^{eq}), \tag{2.11}$$

where τ is the relaxation time and f_i^{eq} is the local equilibrium distribution of particles. To achieve the correct macroscopic behaviour of fluids governed by the Navier-Stokes equation, the equilibrium distribution must be properly chosen. Qian, d'Humières and

Lallemand (1992) proposed the following expression

$$f_i^{eq}(\rho, \mathbf{u}) = \rho w_i \left[1 + \frac{3(\mathbf{c}_i \cdot \mathbf{u})}{c^2} + \frac{9(\mathbf{c}_i \cdot \mathbf{u})^2}{2c^4} - \frac{3\mathbf{u}^2}{2c^2} \right]. \tag{2.12}$$

In Equation 2.12, w_i and c depend on the implemented lattice. For the $D2Q9$ lattice, $c = |\mathbf{c}_i|$ and $w_0 = 4/9$, $w_1 = w_2 = w_3 = w_4 = 1/9$ and $w_5 = w_6 = w_7 = w_8 = 1/36$. The weights w_i are selected in order to achieve macroscopic isotropy and Galilean invariance.

The extension from two dimensions to a three-dimensional lattice configuration follows a similar procedure. The main problem consists in selecting a 3D lattice and calculating the appropriate equilibrium distribution function. A illustration of the $D3Q19$ lattice is shown in Figure 8 with the nineteen possible velocities. Derivation of alternative lattice configurations can be found in Wolf-Gladrow (2004).

The Navier-Stokes equation can be obtained from the described system through a Chapman-Enskog multiscale procedure (CHEN; CHEN; MATTHAEUS, 1992; SHAN; YUAN; CHEN, 2006; PHILIPPI et al., 2006; SIEBERT et al., 2007). The equations for conservation of mass and momentum are, respectively,

$$\partial_t \rho + \partial_\alpha (\rho u_\alpha) = 0, \tag{2.13}$$

$$\partial_t (\rho u_\alpha) + \partial_\beta (\rho u_\alpha u_\beta) = -\partial_\alpha (p) + \nu \partial_\beta \left[\partial_\beta (\rho u_\alpha) + \partial_\alpha (\rho u_\beta) \right], \tag{2.14}$$

where p is the thermodynamic pressure and ν is the kinematic viscosity, given in LBM by

$$p = \rho c_s^2, \tag{2.15}$$

$$\nu = c_s^2 (\tau - 1/2), \tag{2.16}$$

respectively, where c_s is the speed of sound in lattice units and τ is the relaxation time.

Figure 8: Illustration of a three dimensional lattice with nineteen possible velocities ($D3Q19$).

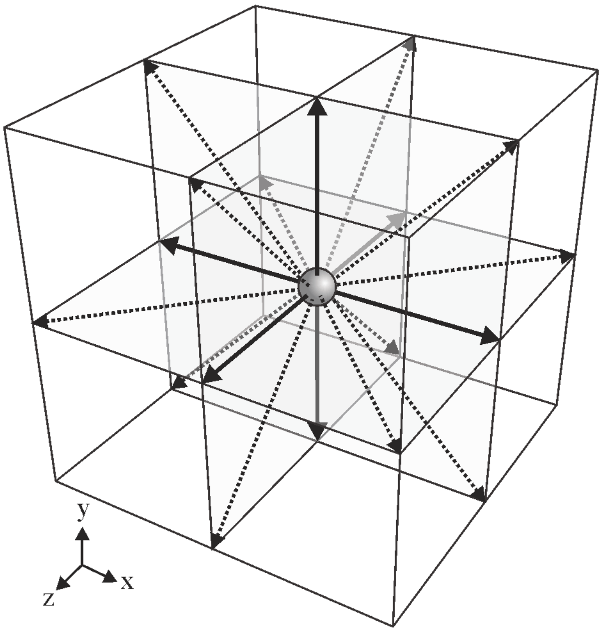

Source: elaborated by the author.

2.2.3 Boundary conditions and forcing schemes

Boundary conditions are an essential part of LBM and must be properly selected to ensure the consistency between simulation and the physical aspects of the system. In the following, the most elementary boundary conditions are briefly described.

(i) Periodic: the simplest boundary conditions are periodic (Figure 9), where opposite edges of the system are connected, e.g., the particle distribution in one edge (which would leave the domain in the propagation stage) return to the opposite edge of the lattice. The result is an infinite system consisting of repetitions of the domain. Periodic conditions are useful when the phenomena is isolated or when external effects are negligible (SUKOP; THORNE, 2006).

Figure 9: Periodic boundary condition.

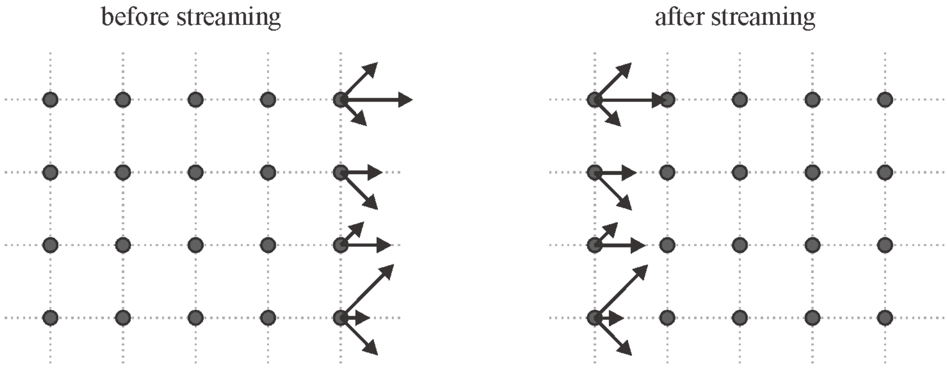

Source: elaborated by the author.

(ii) Bounce-back (no-slip): next to solid surfaces, the bounce-back boundary condition may be imposed in particles contacting solid nodes to simulate viscous friction. This condition consists in inverting the particle distribution in the exact opposite direction of contact. Although the bounce-back condition is simple, it ensures the no-slip condition of the fluid next to the solid wall. Usually, the half-way bounce-back scheme is used as shown in Figure 10 (SUKOP; THORNE, 2006).

Figure 10: Half-way bounce-back boundary condition.

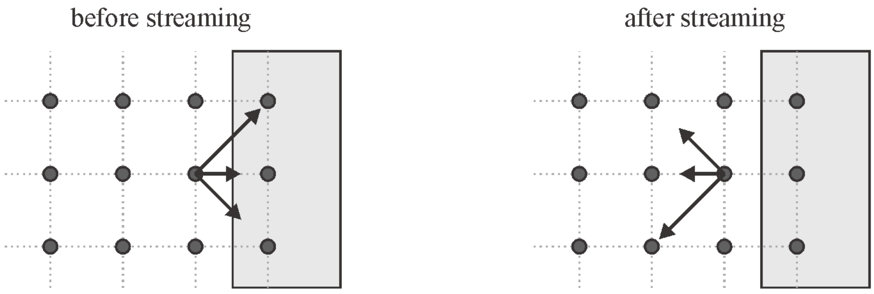

Source: elaborated by the author.

(iii) Mirror (free-slip): this condition is applied to simulate smooth boundaries with negligible friction exerted upon the fluid (free-slip). It may be imposed with a especular reflexion process, which is opposite to the bounce-back condition (Figure 11) (SUCCI, 2001).

Figure 11: Mirror boundary condition.

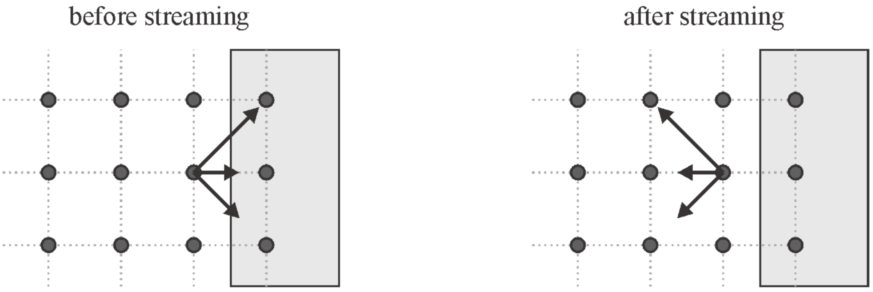

Source: elaborated by the author.

(iv) Neumann: the flux is constrained at the boundary. A common example is when a constant velocity vector is specified at the boundary, and the distribution function and density/pressure are computed at the nodes to maintain this constant velocity (SUKOP; THORNE, 2006).

(v) Dirichlet: a constant pressure/density value is constrained at the boundary. The velocity and distributions functions are computed at the nodes in order to maintain the constant pressure/density (specifying density is equivalent to specifying pressure since they are related by Equation 2.15). The mathematical model for LBM of the Neumann and Dirichlet boundary conditions were proposed by Zou and He (1997) (SUKOP; THORNE, 2006).

Other boundary conditions can be implemented for specific problems. Furthermore, body forces may be incorporated in the model by rearranging the velocity during the computation of f_i^{eq}. For example, the gravitational acceleration ($\mathbf{a}_g$) is incorporated using $f_i^{eq}(\rho, \mathbf{u} + \tau\mathbf{a}_g)$ instead of $f_i^{eq}(\rho, \mathbf{u})$. The variation of momentum in the collision process is

$$\rho \sum_i \Omega_i \mathbf{c}_i = \rho \mathbf{a}_g. \tag{2.17}$$

Another method used to incorporate external forces in LBM is called forcing scheme, which basically consists in adding a force term in the collision operator (Equation 2.11) or adding a source term in the evolution equation (Equation 2.9). Several forcing schemes are available in literature and provide an important technique for particular problems (MOHAMAD, 2011).

2.2.4 Relation of lattice units and physical units

In LBM, physical quantities are computed in terms of lattice units. The length is expressed in lattice space units, time is expressed in time step units, and mass is expressed in terms of the density of number of particles (number of particles per node). It is convenient to use dimensionless parameters (such as the Reynolds or capillary number) to analyze and compare results, since they provide a similarity relation between simulation and the real system without the need of unit conversion.

However, in several cases the physical quantity is relevant and it is necessary to convert lattice units to physical units. The procedure for space, time and mass conversion is described in the following, from which all physical quantities may be calculated. (WOLF, 2006)

(i) Length: the lattice unit space, Δx, is the basic length unit and represents the space between two neighboring nodes. By assigning a linear dimension l to N lattice nodes, the physical equivalent δ_x is

$$\delta_x \equiv \Delta x = \frac{l}{N}. \tag{2.18}$$

(ii) Time: the timestep Δt is the basic time unit in lattice units and represents the time required for a particle to move between two neighbouring nodes. The physical correspondent is obtained by equalizing the capillary number in lattice units and the capillary number in physical units. Thus,

$$\delta_t \equiv \Delta t = \frac{\mu_F}{\mu_{LB}} \frac{\sigma_{LB}}{\sigma_F} \delta_x, \tag{2.19}$$

where the index F indicates a physical unit and LB a lattice unit.

(iii) Mass: the number of particles per lattice nodes ρ is the basic specific mass unit in lattice units. The physical specific mass is $\rho_F = \rho\delta_m/\Delta x^3$. Thus

$$\delta_m = \frac{\rho_F}{\rho} \Delta x^3. \tag{2.20}$$

δ_m represents the product between the mass of a fluid molecule and the number of molecules that each LB particle represents, which is evident when $\rho = 1$ (WOLF, 2006).

2.2.5 Multiphase and multicomponent models

Microscopically, the segregation of a multicomponent fluid system is due to the interparticle forces. While these particle-particle interactions are difficult to implement in traditional methods, they can be naturally taken into account in numerical methods based on the simulation of the motion of particles or particle distributions, such as the LBM (HOU et al., 1997).

The application of LBM for multiphase and multicomponent flow analysis has been discussed since the emergence of the method. Several models have been introduced during the last two decades and the development is in constant growth. Among the popular models are the color-gradient model, the inter-particle potential model, the free-energy model and the mean-field theory model. They have distinct characteristics, mainly in the calculation of the interface between phases and fluids during the evolution of the particle distribution functions. The characteristics of the studied phenomena must be considered during the model selection.

The earliest model is the color-gradient model proposed by Gunstensen et al. (1991), which is based on the Rothman-Keller (RK) multiphase lattice gas model (ROTHMAN; KELLER, 1988). In the two-component model, one component is red-colored fluid and the other is blue-colored fluid. Two distribution functions are used to represent the two fluids. In addition to the common collision step in the LBM, there is an extra collision term and a recoloring step that promotes the phase segregation. One advantage of the RK model is that the surface tension and the ratio of viscosities can be adjusted independently (HUANG; SUKOP; LU, 2015).

The Shan-Chen (SC) or inter-particle potential model (SHAN; CHEN, 1993) appeared soon after the color-gradient model. In the single-component multiphase (SCMP) SC model, incorporating a forcing term into the corresponding LB equation replaces the ideal gas equation of state (EOS) by a nonideal nonmonotonic EOS. In the multicomponent multiphase (MCMP) SC model, each component is represented by its own distribution function.

Swift et al. (1996) introduced the free-energy (FE) model. It is built upon the phase-field theory, in which a free-energy functional is used to account for the interfacial tension effects and describes the evolution of interface dynamics in a thermodynamically consistent manner (LIU et al., 2016).

In the mean-field theory or HCZ model proposed by He, Chen and Zhang (1999), two distribution functions and two corresponding LBEs are used: a pressure distribution function is introduced to replace the single-particle density distribution function and an index function is used to track interfaces between different phases.

Many derivations of the popular models are available in literature. The objectives of these improvements are to increase density and viscosity ratios, specify the wetting condition and increase the discretization order of kinetic equations. Huang, Sukop and Lu (2015) and Philippi et al. (2016) provide a detailed insight on the models presented in this section and further improvements.

Recently, Spencer, Halliday and Care (2010) introduced a novel fluid segregation scheme and interface-forcing method with flexibility to multi-relaxation times schemes based on the color-gradient model. This model is used as a basis for the LBM code used in this work and it will be detailed in chapter 3.

2.3 STATE OF THE ART

This section is dedicated to the review of recent publications which refer to the main topic of this work – the influence of capillary number on the residual saturation of wetting phase during drainage. The capillary number (Equation 2.4) is the ratio of viscous to capillary forces and depends on the fluid viscosity, the velocity (or rate) of displacement and the interfacial tension between fluids. Therefore, the effect of capillary number may be evaluated by changing these three parameters individually or mutually.

The variation in capillary number (Ca) in an immiscible displacement may produce different phenomena depending on the set of parameters that are changed and the range of variation. Moreover, the effect of Ca can be influenced by distinct porous media geometries, wettabillity characteristics, high heterogeneity, fluid rheology, etc. The very form of capillary number equation (Equation 2.4) can be written in different versions and it is subject of discussion on time and length scale of acting forces (JAMALOEI; ASGHARI; KHARRAT, 2012; ARMSTRONG et al., 2014). The extensive available literature on immiscible displacement attests to the complexity of this subject. The following discussion attempts to resume relevant phenomena with recent contributions available in scientific literature.

2.3.1 Drainage and imbibition mechanisms

Capillary forces are described by the Young-Laplace equation (Equation 2.3) and depend on the interfacial tension between phases and geometry of the medium. The effect of viscous forces is determined by the intermolecular forces of each fluid and is strongly influenced by fluids viscosity ratio. The balance of these two forces affects directly the form of displacement during the processes of drainage and imbibition.

Drainage occurs when a nonwetting fluid displaces a wetting fluid, contrary to imbibition where a wetting phase displaces the nonwetting fluid. The two processes are governed by different mechanisms. Typically, in slow drainage the invading nonwetting fluid enters first the bigger pores, only when capillary pressure is equal to or greater than the threshold pressure of these pores. In contrast, in imbibition at low injection rate, the invading fluid will enter first the narrowest pores.

Lenormand, Touboul and Zarcone (1988) published one of the first works comparing pore-network models and experiments to analyze the macroscopic forms of displacement during drainage. A two-dimensional porous medium made of interconnected capillaries was used and several drainage process were carried out under different capillary number and viscosity ratios (M). Their results show the existence of three basic regimes: capillary fingering, viscous fingering and stable displacement (Figure 12).

Figure 12: Immiscible displacement patterns during drainage: (a) stable displacement; (b) viscous fingering; (c) capillary fingering.

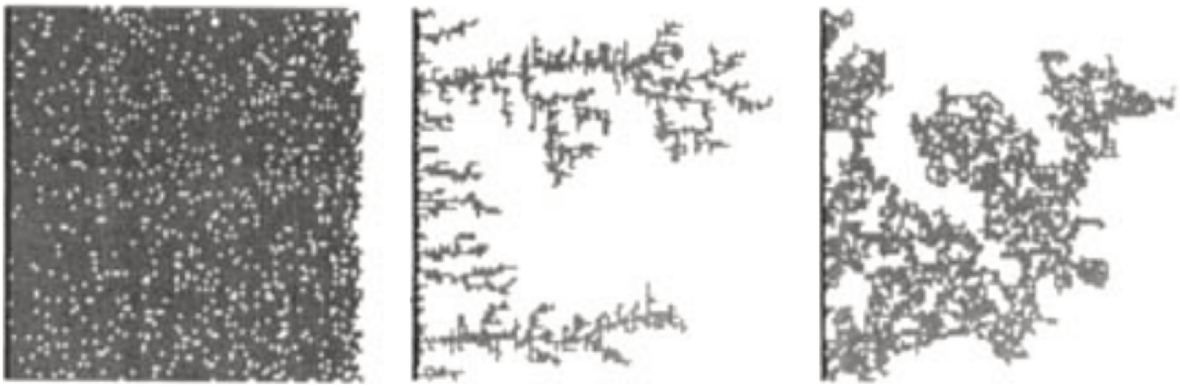

(a) (b) (c)

Source: Lenormand, Touboul and Zarcone (1988).

Stable displacement occurs when viscosity of injected fluid is higher than displaced one ($M > 1$) and at relatively high Ca. The principal force is due to the viscosity of the injected fluid; capillary effects and pressure drop in the displaced fluid are negligible. The pattern presents a flat front with some irregularities at the scale of a few pores. The size of the clusters trapped behind the front is also only a few pores.

At relatively high Ca and $M < 1$, tree-like fingers of the invading fluid appear leading to unstable displacement, characterizing the viscous fingering regime. The main force is due to the viscosity of the displaced fluid; capillary effects and pressure drop in the displacing fluid are negligible. The tree-like fingers present no loops, they spread across the whole network and they advance constantly towards the outlet.

By lowering Ca and balancing viscosity ratio ($M \sim 1$), capillary fingering regime is achieved. Nonwetting phase invades the largest available pore throats, and progressively invades smaller and smaller pore throats in an "invasion percolation" process (WILKINSON; WILLEMSEN, 1983) as nonwetting phase pressure increases. The fingers spread across the network and grow in all directions, even backward (towards the entrance). They form loops which trap the displaced fluid and the size of the trapped clusters ranges from the pore size to big clusters (at core sample scales).

Morphologically, capillary fingering patterns approach a fractal shape and are characterized by many trapped fluid clusters, whereas viscous fingering patterns exhibit thin, branching fingers, with fewer interconnections and, hence, reduced trapping (BORGMAN et al., 2019).

Sukop and Or (2003) used a Shan-Chen LBM multiphase model to analyze the invasion percolation during drainage in simple porous media consisting of a random networks of pores generated by sparse distributions of solid disks and squares. Their results are simple, but demonstrate the invading fluid's selectivity for the largest available pore and the effect of Ca. Capillary and viscous fingering are also exhibited even though no discussion is carried out on the subject.

A number of recent numerical and experimental studies have been conducted to understand and characterize the drainage patterns described by Lenormand, Touboul and Zarcone (1988). Yiotis et al. (2007) used HCZ LBM multiphase model to investigate viscous coupling in co-current flow and described the lubricating effect and its influence on relative permeability and saturation. Dong et al. (2010) and Dong, Yan and Li (2011) run simulations with a SC multiphase model to investigate the effect of several parameters (including Ca) on viscous fingering in capillary tube and 2D homogeneous porous media. Zhao and Mohanty (2019) conducted experiments on different oil-wet cores under low Ca and found that as flow rate decreases fewer fingers are created. The experiments also showed that under similar conditions, viscous fingering is more severe in drainage compared to imbibition.

The three displacement regimes described by Lenormand, Touboul and Zarcone (1988) were plotted on a $Ca-M$ phase diagram (Figure 13), separated by zone boundaries that indicate the crossover region (white) between the regimes. Liu et al. (2013) and Huang, Huang and Lu (2014) used different LBM models to evaluate the regime patterns under different Ca and M. Both works demonstrate that LBM is capable of simulating fingering phenomena in heterogeneous 2D media. Moreover, different zone boundaries of the phase diagram were found to be caused by distinct media geometries, leading to larger crossover regions where more than one regime is found. Based on percolation theory, Liu et al. (2013) stated that the difference is resulted mainly from heterogeneity, which is an additional factor that affects the fingering patterns. In fact, by using a more homogeneous medium, Zhang et al. (2011) found a smaller crossover zone and stated that the $Ca - M$ diagram is system-dependent: "if the same Ca was imposed on our micromodel and a similar micromodel with different post and pore-throat sizes, the dominant displacement mechanism (viscous versus capillary fingering and unstable versus stable displacement) would not necessarily be the same" (ZHANG et al., 2011).

Tsuji, Jiang and Christensen (2016) used the color-gradient model to analyze the drainage patterns in a 3D digital model constructed from CT scans of a natural rock sample. Capillary and viscous fingering regimes were observed and highlighted in a phase diagram. However, clear stable displacement was not observed. Instead, an unstable displacement close to capillary fingering was found mainly due to heterogeneity. The natural rock embodies a wide variety of pores (from narrow to wide throats). Thus, high threshold capillary pressure is required when the nonwetting phase passes through the

Figure 13: $Ca - M$ phase diagram.

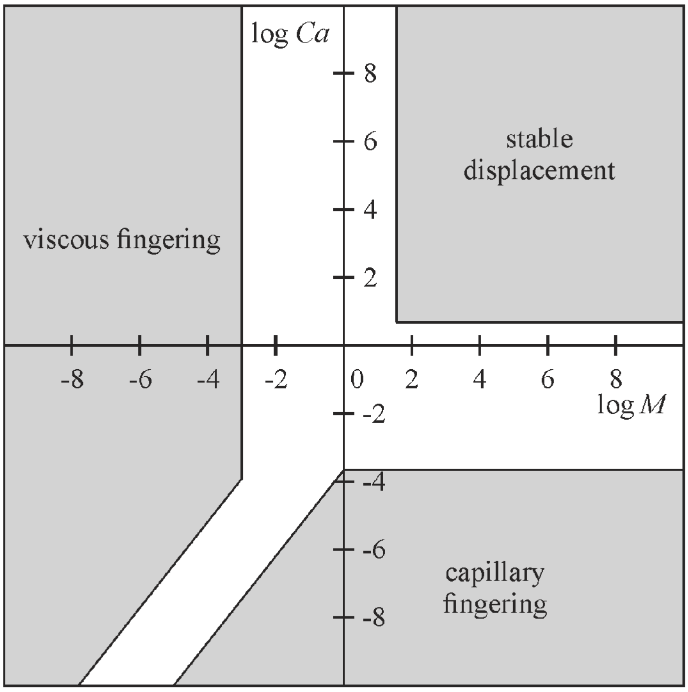

Source: adapted from Lenormand, Touboul and Zarcone (1988).

narrow pore throats. This leads to heterogeneous trapping of nonwetting phase, local capillary fingering even at relatively high Ca and simultaneous occurrence of multiple displacement patterns.

Those findings clearly show that displacement patterns are dependent not only on flow parameters, but also on pore structure and particularly on local pore geometry, mostly because pore-scale flow events depend strongly on the geometry of pores and throats.

Pore-scale mechanisms can impact the pressure-saturation relationship during drainage, however they are not entirely understood in the range of the three displacement patterns (TSUJI; JIANG; CHRISTENSEN, 2016). Andrew et al. (2015) described three mechanisms during low rate drainage which occur due to Haines jumps (HAINES, 1930; SUN; SANTAMARINA, 2019). Using laboratory experiments and LBM simulations, Herring et al. (2018) found snap-off events caused by Haines jumps and showed the relationship of ganglia distribution caused by snap-off with flow rate.

The occurrence of Haines jump events is a characteristic feature of multiphase flow in porous media, primarily associated with drainage dynamics. These events are accompanied by an abrupt increase in the fluid velocity, as the interface jumps from a narrow restriction into a wider pore body. This leads to fluid redistribution in the surrounding area of a draining pore, as a significant fraction of the nonwetting phase, required to drain the pore-body, is supplied by imbibition occurring in the neighbouring pore throats (ZACHAROUDIOU; BOEK, 2016). The localized imbibition of wetting phase at the constriction causes snap-off of small isolated nonwetting ganglia in front of the main invading fluid front or even in areas far from the jump local (HERRING et al., 2018). Several works were published trying to describe these mechanisms, which are strongly influenced by the capillary number (ANDREW et al., 2015; ARMSTRONG et al., 2015; ZACHAROUDIOU; BOEK, 2016; HERRING et al., 2018; TSUJI; JIANG; CHRISTENSEN, 2016).

Imbibition usually shows distinct macroscale displacement patterns and pore-scale mechanisms. Hughes and Blunt (2000) used a pore network model and identified five generic displacement patterns: flat frontal advance, dendritic frontal advance, bond percolation, compact cluster growth, and ramified cluster growth. These patterns are strongly influenced by capillary number, viscosity ratio, contact angle and initial wetting saturation. At pore-scale, they can be characterized by different mechanisms: piston-like advance in throats and pores, snap-off and cooperative pore-body-filling.

Piston-like advance refers to the displacement of nonwetting phase from a throat by an invading interface initially located in an adjoining wetting phase filled pore-body. The invading wetting phase preferentially fills the narrowest regions of the pore space. Piston-like displacement in throats is favoured while wetting phase advance is impeded by the larger pore-bodies.

Snap-off refers to the invasion of a nonwetting phase filled throat by arc menisci or wetting layers initially present in corners, crevices and rough surfaces of the pore space. For small injection velocities, wetting layers will swell and thicken ahead of the bulk wetting phase invasion in pores and throats. At a critical capillary pressure, the arc menisci fuse and the center of the throat spontaneously fills with wetting phase, sometimes trapping the nonwetting phase on a pore.

Cooperative pore-body filling refers to cases where wetting phase displaces nonwetting phase from a pore-body when one or more of the connecting throats are filled with nonwetting phase (RUSPINI; ØREN, 2017).

2.3.2 Capillary number effect on residual saturation

Displacement patterns are associated with different pore-scale mechanisms and are influenced by several parameters, Ca being one of the most relevant. These are important information to understand how capillary number affects the residual wetting and nonwetting saturation during drainage and imbibition, since the final phase distribution inside the porous medium is strongly influenced by events occurring during the process. The following discussion addresses first the drainage process and then the imbibition, while some referenced works investigated both processes.

Typical field reservoirs are in a Ca range of 10^{-8} to 10^{-2} (SATTER; IQBAL, 2016). The lower values of Ca in typical field reservoir are very difficult to simulate because of low rates of fluid injection. However, they are important in the evaluation of capillary desaturation curves (CDC), which describe the relationship between Ca and the residual phase saturation for different wettability system (Figure 14). The CDC allows the analysis of the critical Ca, which is a value that indicates the point where increasing Ca effectively decreases the residual saturation of the displaced fluid. Below critical Ca, the variation of Ca does not affect the residual saturation (LAKE, 1989).

Lenormand, Touboul and Zarcone (1988) introduced the $Ca - M$ diagram and showed the different patterns during drainage. They measured the wetting phase saturation when the displacing nonwetting fluid reached the outlet, characterizing the breakthrough (BT). At this stage, the effect of Ca on wetting phase saturation depends highly on M. If $M < 1$, S_w increases with increasing Ca. The opposite trend is found when $M > 1$. However, the effect of Ca on S_w can be different if measured at breakthrough of at quasi-steady state, were irreducible wetting saturation is reached.

Cottin, Bodiguel and Colin (2010) and (ZHANG et al., 2011) reported experimental results of drainage in micromodels for Ca ranging between 10^{-7} and 10^{-1} and different values of M. At a quasi-steady (QS) state, they found that increasing Ca leads to a

Figure 14: Typical capillary desaturation curve (CDC).

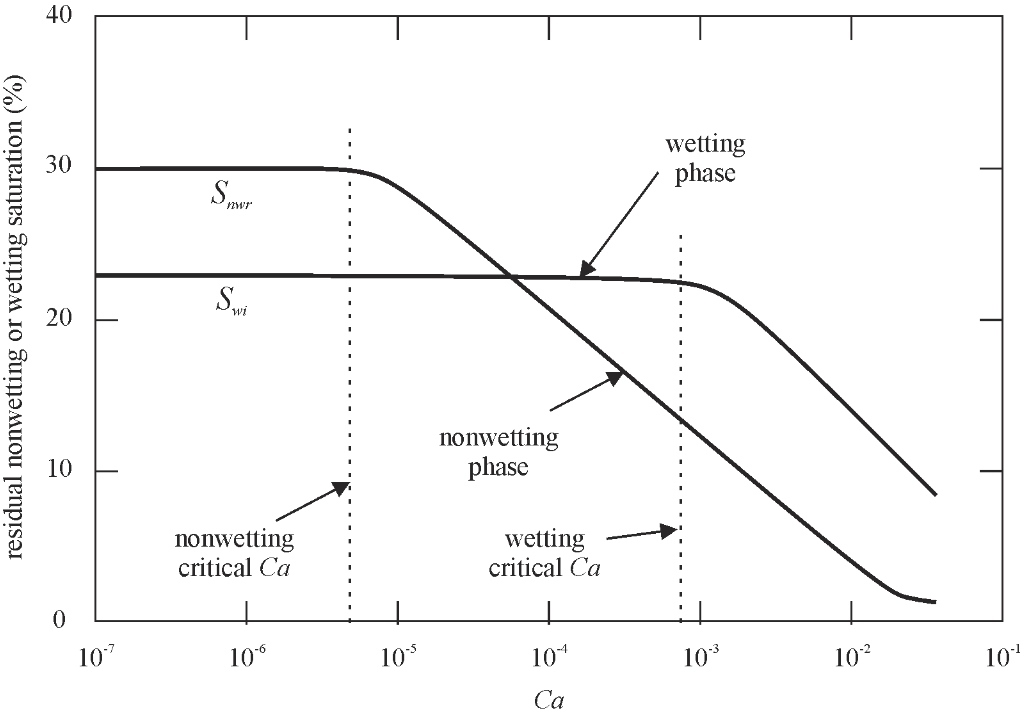

Source: adapted from Lake (1989).

decrease in S_{wi}, mostly by reducing the number and size of clusters trapped because of capillary fingering.

Liu et al. (2013) carried out LBM simulations of drainage until breakthrough. The 2D domain consisted of a staggered periodic array of uniform square grains. Ca ranged from 8.66×10^{-5} to 8.66×10^{-3}. It was found that S_w decreases with increasing Ca, with small deviations due to viscous instabilities. Moreover, at high Ca less time is needed for breakthrough, as well as an increasing non-uniform distribution in finger size. Huang, Huang and Lu (2014) achieved similar results using a more heterogeneous porous medium and a multi-relaxation time model for simulations.

Tsuji, Jiang and Christensen (2016) used a LBM model to analyze drainage in a 3D digital model constructed from CT scans of a natural rock sample. They plotted the nonwetting saturation at breakthrough on the $Ca - M$ phase diagram, showing that the increase in Ca tends to increase S_w. The capillary fingering results in a higher sweeping efficiency, followed by stable displacement and viscous fingering. A different trend is found with a 2D homogeneous model, where stable displacement is more effective. However, since irreducible wetting saturation at final steady state was not reached it is not possible to affirm which pattern is really more effective in the sweeping process. Their results also show the effect of displacement pattern on the saturation history. Capillary fingering curve shows a step-like behaviour suggesting reverse Haines Jumps and reverse flow. Viscous fingering shows almost a linear curve suggesting a constant advance of fingers towards the outlet.

Using a LBM method, Xu et al. (2018) investigated the capillary desaturation curve during drainage and imbibition with the discontinuous and continuous displacement methods. These methods were first proposed by Chatzis and Morrow (1984) and Morrow, Chatzis and Taber (1988), who used laboratory experiments to analyze only imbibition. The continuous CDC method involves a series of unsteady-state simulations. Separate simulations are conducted, each with the same initial fluid distribution but at different capillary numbers. Remaining phase saturation at steady state is then measured for each simulation. In the discontinuous CDC method an initially small capillary number is simulated until remaining phase saturation is achieved. Then the capillary number is increased in a step-wise fashion (bumped) and a new saturation is measured for each "bump" in capillary number (XU et al., 2018).

Their results confirm that the critical capillary number is larger for the discontinuous CDC method, indicating a less efficient displacement process. Moreover, the critical capillary number tends to be higher in drainage than for imbibition, and the residual phase saturation in drainage tends to be lower than in imbibition at low capillary numbers (XU et al., 2018). This is consistent with the CDC example shown in Figure 14.

It is important to note that the CDC curves are obtained with drainage and imbibition in partially saturated rocks. This is usually done by carrying out initial drainage and imbibition processes to achieve the desired saturation of nonwetting and wetting fluids.

Patel, Kuipers and Peters (2019) analyzed drainage in a repeated single-pore and in a random multi-pore network with a VOF (volume of fluid) method. They found that in a single-pore domain, increasing Ca leads to higher residual wetting saturation at breakthrough, in opposite to multi-pore arrangement where residual wetting saturation decreases at higher Ca. This is because in a viscous fingering regime in the single-pore the nonwetting fluid will travel one path, leaving most of other pores full of trapped wetting phase. Ca values in the simulations were relatively high compared to typical field values.

Zhao and Mohanty (2019) conducted drainage and imbibition experiments in natural cores using typical reservoir low Ca range. They found that fluid recovery at breakthrough and after injection of 1 PV (pore volume) depends on the geometry used, and in majority of the cases the residual S_w increases with increasing Ca.

Wang et al. (2019) performed simulations using a VOF method and digital models constructed with CT scans, showing that oil recovery increases with increasing Ca for oil-wet and water-wet models. They found also that critical Ca in the CDC for drainage is higher than imbibition and range from 10^{-5} to 10^{-6}, which is in agreement with laboratory experiments. However, the critical Ca is dependent on wettability, viscosity ratio and heterogeneity, which makes the estimation of the CDC more challenging (LAKE, 1989).

Wang et al. (2019) also calculated the residual saturation as function of a "macroscopic" capillary number. They found that for the considered form of macroscopic Ca, the critical Ca is about 1. This method allows the analysis of the effect of up-scaling Ca by considering the size of clusters during displacement (GEORGIADIS et al., 2013; ARMSTRONG et al., 2014).

Imbibition shows a similar trend as drainage in the $S_{nwr} - Ca$ relationship. As Ca increases, the residual saturation of nonwetting fluid decreases (HAZLETT; CHEN; SOLL, 1998).

Nguyen et al. (2006) used a pore-network model to analyze the effect of displacement rate, contact angle and pore geometry on residual saturation during imbibition. At low Ca, snap-off events are visualized leading to more trapping and higher S_{nwr}. At high displacement rates, snap-off is suppressed and lower residual saturation is achieved. The results also showed that the effect of Ca is sensitive to pore-throat aspect ratio and pore shape. This proves that heterogeneity is an important factor on residual saturation and critical Ca for imbibition.

Other forms of evaluating the effect Ca on residual saturation during imbibition were studied. Nilsson et al. (2013) carried out imbibition experiments in micromodels, and varied Ca by changing flow rate and interfacial tension between fluids. Both methods show that with higher Ca tends to decrease S_{nwr}. Khishvand, Akbarabadi and Piri (2016) conducted drainage-imbibition cycles on rock samples and found that as capillary number increases, imbibition produces smaller trapped oil globules, i.e., the volume of individual trapped oil globules decreased at higher flow rates, resulting in lower residual saturation. Critical Ca is found to be between 10^{-6} and 10^{-5}.

Ansarinasab and Jamialahmadi (2017) run imbibition simulations with a LB model in a 2D heterogeneous model created by Yiotis et al. (2007). They found that increasing Ca leads to an increase in residual saturations. This is a different trend than those observed in previous works. Difference in structure and size of porous media, density of phases and a high Ca range considered ($10^{-2} < Ca < 10^{-1}$) are the main reasons for observed discrepancies.

Recently, Pereira (2019) used a “gray-scale” LB model to run drainage and imbibition displacements in a 3D heterogeneous model constructed from CT scans of a rock sample with low porosity (0.11) and permeability (57.03 mD). Wettability was changed to simulate cases of wetting and nonwetting invasion and one case with neutral wettability. It was found that residual saturation at breakthrough decreases with increasing Ca for all cases. However, in neutral wetting, at the highest capillary number the residual saturation is significantly higher. At a higher capillary number the invading fluid tends to take the most direct path to the outlet (similar to viscous fingering). It does not invade as much of the porous medium as with slightly lower capillary numbers. The flood at the lower Ca ensembles a capillary fingering pattern – a meandering path ensues and consequently reduces residual saturation.

In drainage, the capillary pressure head required for the nonwetting fluid to invade is much larger than for the neutral wetting case, resulting in higher residual saturation. For a wetting fluid invasion, the residual saturation decreases more than other cases. The fluid tends to wet as many as the accessible pores as possible, yielding more efficient sweep of the porous domain. However, the residual saturation is still high indicating a highly disconnected pore structure and very low permeability (PEREIRA, 2019).

An important point observed was the time required to reach maximum residual saturation for the three different wetting cases. The longest time corresponds to the wetting invading fluid and indicates that the flood is mainly driven by preference of wetting fluid to be adsorbed to the substrate. The neutral wetting case took the shortest time, indicating the flow was driven by pressure difference between fluids. In the nonwetting invading fluid case, the flow is also driven by pressure difference, but it is inhibited by the additional capillary pressure required by the nonwetting fluid to enter pores. However, since nonwetting fluid tends to take the most direct path to the outlet, it takes a shorter time to reach breakthrough than the wetting invading flood (PEREIRA, 2019).

2.3.3 Conclusions

The discussion showed relevant results and contributions for the analysis of the effect of capillary number on immiscible displacement and residual saturation. Table 1 gives a summary of the main conclusions from the referenced works. It is interesting to observe the diversity of parameters and methods used. The conclusions are also different mainly because of different times of measure (breakthrough or quasi-steady state). At a quasi-steady state, increase of capillary number appears to have a positive effect on recovery efficiency. However, this effect can be sensitive to other parameters such as viscosity ratio, wettabillity, and more important, the medium geometry and heterogeneity. Natural rocks present complex geometries with a large range of pore sizes and shapes which can change in the extension of the rock. Moreover, they can present surface roughness, contamination, and heterogeneous wettabillity conditions that can even change with time. Thus, for any new rock to be explored, it is necessary to evaluate its extraction efficiency taking into account the specific characteristics of the rock and the fluids contained therein. All theses aspects introduce challenges for the real evaluation of residual saturation, which is the main objective of the present work.

Table 1: Main parameters and conclusions of referenced works. BT = breakthrough; QS = quasi-steady; UNK = unknown.

Reference	**Method**	**Dim**	**Geometry**	$\boldsymbol{Ca}$	$\boldsymbol{M}$	$\boldsymbol{\theta}$	**Time**	**Conclusion**
Lenormand, Touboul and Zarcone (1988)	pore network model	2D	homogeneous	$10^{-11} - 10^{0}$	2×10^{-5} and 79	UNK	BT	Ca effect on S_w depends on M
Cottin, Bodiguel and Colin (2010)	MF experiments	3D	homogeneous	$10^{-7} - 10^{-2}$	0.7, 3.4 and 10	$110° - 160°$	QS	S_{wi} decreases with increasing Ca
Zhang et al. (2011)	MF experiments	3D	homogeneous	$10^{-6} - 10^{-1}$	$10^{-2} - 10^{2}$	$105° - 128°$	QS	S_{wi} decreases with increasing Ca
Liu et al. (2013)	LBM	2D	homogeneous	$9 \times 10^{-5} - 9 \times 10^{-3}$	0.05	120°	BT	S_w decreases with increasing Ca
Huang, Huang and Lu (2014)	LBM	2D	heterogeneous	$10^{-3} - 10^{3}$	$10^{-2} - 10^{2.7}$	180°	BT	S_w decreases with increasing Ca
Tsuji, Jiang and Christensen (2016)	LBM	3D	heterogeneous	$10^{-5} - 10^{-1}$	$10^{-1} - 10^{1}$	180°	BT	S_w increases with increasing Ca
Huang, Xiao and Yin (2017)	LBM	3D	nearly homogeneous	$1.5 \times 10^{-4} - 2 \times 10^{-1}$	1 and 10	120°	QS	S_{wi} decreases with increasing Ca
Jiang et al. (2018)	MF experiments	3D	heterogeneous	$5 \times 10^{-9} - 10^{-7}$	0.03 and 0.3	UNK	QS	S_{wi} decreases with decreasing Ca
Xu et al. (2018)	LBM	3D	heterogeneous	$2 \times 10^{-5} - 3.5 \times 10^{-4}$	UNK	150°	QS	S_{wi} decreases with increasing Ca
Borgman et al. (2019)	pore network model and MF experiments	2D	nearly homogeneous	$2 \times 10^{-6} - 3.7 \times 10^{-5}$	0.018	163°	BT	S_w decreases with decreasing Ca
Hejazi, Shah and Pini (2019)	natural rocks experiments	3D	heterogeneous	$10^{-8} - 10^{-7}$	0.02	UNK	QS	S_{wi} decreases with increasing Ca
Patel, Kuipers and Peters (2019)	VOF	3D	heterogeneous	$0.01 - 1$	20	120°	QS	S_{wi} decreases with increasing Ca
Pereira (2019)	LBM	3D	heterogeneous	$5 \times 10^{-6} - 5 \times 10^{-4}$	1	UNK	BT	S_w decreases with increasing Ca
Wang et al. (2019)	VOF	3D	heterogeneous	$10^{-8} - 10^{-2}$	0.08	170°	QS	S_{wi} decreases with increasing Ca
Zhao and Mohanty (2019)	natural rocks and MF experiments	3D	heterogeneous	$5 \times 10^{-9} - 2.4 \times 10^{-7}$	$10^{-3} - 0.04$	150°	BT	Ca effect on S_w depends on geometry

Source: elaborated by the author.

3 METHODOLOGY

In this chapter, the methods and steps applied to carry out the computational simulations of drainage in digital rock models using LBM are explained. In the first section, the novel multiphase Lattice Boltzmann model used for simulations is explained. Section two shows the relevant characteristics of the different digital models used to simulate the porous medium, including 2D homogeneous and heterogeneous models and the 3D natural rock models. Section three describes the setup of simulations, i.e., initial and boundary conditions, computational domain, fluid parameters and simulation process.

3.1 TWO-PHASE LATTICE BOLTZMANN MODEL

A three-dimensional color gradient multicomponent LB model is used based on the work of Spencer, Halliday and Care (2010) and Spencer, Halliday and Care (2011). The present work introduces a new feature for this model by including a two-relaxation time scheme for the collision operator. The method will be explained in a succinct version since the mathematical description is too extensive to be shown in this work. The references following each part provide further details.

In this model, two fluids, designated as red and blue, which occupy lattice link i at nodal position $\mathbf{x}$ and time t are described by two colors distribution functions R_i and B_i, respectively, and

$$f_i(\mathbf{x},t) = R_i(\mathbf{x},t) + B_i(\mathbf{x},t). \tag{3.1}$$

The nodal density and momentum of the red and blue fluids are calculated with Equation 2.7 using each individual distribution function (R_i and B_i). Density and velocity of the single sum lattice fluid are defined by Equation 2.7 using distribution f_i.

As the fluids mix in an interfacial region, they define a single mixed fluid which evolves according to evolution equation (Equation 2.9). To distinguish individual fluids in a lattice node, a fluid component index, or phase field, is used:

$$\rho^N(\mathbf{x},t) \equiv \frac{\rho_R(\mathbf{x},t) - \rho_B(\mathbf{x},t)}{\rho_R(\mathbf{x},t) + \rho_B(\mathbf{x},t)}, \qquad -1 < \rho^N(\mathbf{x},t) < 1, \tag{3.2}$$

where surfaces of constant value define the interface, with the surface $\rho^N = 0$ taken to define its center (HALLIDAY; HOLLIS; CARE, 2007). In practical terms, this is equivalent to calculate the concentration of each fluid in a lattice node. By distinguishing the fluids in each lattice node with the phase field, it is possible to define which parameters (density and viscosity) will be used to apply the collision rule in each lattice node.

The two-relaxation time scheme of Ginzburg (2005) is implemented for the collision operator. This model relays on the concept of decomposition of the distribution function in a symmetric (f_s) and an antisymmetric (f_a) part. Then, the collision is performed using a BGK operator (Equation 2.11) for each part:

$$\Omega_i = \frac{f_{s,i} - f_{s,i}^{eq}}{\tau_s} + \frac{f_{a,i} - f_{a,i}^{eq}}{\tau_a}, \tag{3.3}$$

where $f_{s,i}^{eq}$ and $f_{a,i}^{eq}$ are the equilibrium distribution for the symmetric and antisymmetric part, respectively, each part having an individual method for calculation (GINZBURG, 2005). In this model, viscosity is calculated by Equation 2.16 using the relaxation time of the symmetric part τ_s for each fluid. The τ_a is a function of τ_s in order to vanish high order spurious terms.

An additional force term is included in the collision operator to apply the interface dynamics, and it is formulated based on a viscous stress perturbation that promotes a Laplace pressure step between the fluids in the interfacial region (SPENCER; HALLIDAY; CARE, 2010). In Einstein notation, the force term is given by:

$$F_i = \rho w_i \left(\frac{\alpha |\nabla w_r|}{c_s^2 \tau} \right) (\mathbf{n}_m \mathbf{n}_n - \delta_{mn})(\mathbf{c}_{i,m}\mathbf{c}_{i,n} - c_s^2 \delta_{mn}), \tag{3.4}$$

where w_i is a directional-dependent weight as shown in Equation 2.12 for the $D2Q19$ lattice, ∇w_r is the gradient of red fluid saturation for each direction of a lattice node, $\mathbf{n}$ is the unit vector normal to the interface between phases, $\mathbf{c}_i$ is the lattice velocity, δ_{mn} is the Kronecker delta, and α is a coefficient proportional to the emerging interfacial tension between phases. Using this force term, the interfacial tension will be given by

$$\sigma = 2\rho c_s^2 \alpha. \tag{3.5}$$

A segregation rule is included in the particle evolution process in a post-collision, pre-streaming step, and is defined by the following recolouring scheme:

$$R_i(\mathbf{x} + \mathbf{c}_i, t+1) = \frac{\rho_R}{\rho_R + \rho_B} f_i(\mathbf{x}, t+1) + \beta w_i \frac{\rho_R \rho_B}{(\rho_R + \rho_B)^2} \mathbf{n}_m \mathbf{c}_{i,m}, \tag{3.6}$$

$$B_i(\mathbf{x} + \mathbf{c}_i, t+1) = \frac{\rho_B}{\rho_R + \rho_B} f_i(\mathbf{x}, t+1) - \beta w_i \frac{\rho_R \rho_B}{(\rho_R + \rho_B)^2} \mathbf{n}_m \mathbf{c}_{i,m}, \tag{3.7}$$

where ρ_R and ρ_B are, respectively, the red and blue fluid densities at a node $\mathbf{x}$ in timestep t, and β is a recolouring coefficient that controls the interface width. Together with α, they control the interface characteristics and their values must be carefully chosen to ensure simulation stability.

The streaming stage is carried out with a swap algorithm proposed by Mattila et al. (2007). Its main assets are the possibility of using only one lattice and its ability to fuse the collision and streaming steps at the implementation level by exploiting only a few temporal variables. The lattice nodes in the domain are iterated starting from the node having the smallest enumeration number up to the node with the largest number. For each fluid node, the distribution values with defined velocity index are exchanged with the appropriate distribution values of the neighbouring node. Immediately after the swapping of distribution values, the collision procedure is performed for the node in question. Special attention must be given to the locations of distribution values after the collision and for initialization of boundary nodes (MATTILA et al., 2007, 2008).

To implement wettability on a solid wall, it is assumed that the solid wall is a mixture of two fluids with constant proportions, i.e., solid nodes have a certain value of the phase field ρ^N. This is controlled by a parameter called concentration of red fluid at the wall w_{wr}. If the contact angle to the red component is θ_r, then

$$w_{wr} = \frac{\cos\theta_r - 1}{2}, \qquad 0 \leq w_{wr} \leq 1. \tag{3.8}$$

If $\theta_r = 180$, then w_{wr} is 0 and ρ^N at the wall is -1, and the red fluid will be strongly nonwetting. If $w_{wr} = 1$, the red fluid is strongly wetting, and for intermediate values the wetting condition is mixed.

Finally, the algorithm steps used in the simulation consist in:

(i) create the distribution functions R_i and B_i in the fluid nodes of the computational domain according to the initial saturation condition chosen;

(ii) apply the boundary conditions, including wetting condition on solid walls;

(iii) collide according to the two-relaxation time collision operator with the interfacial forcing term;

(iv) determine and apply the segregation rule;

(v) swap the distribution values with the appropriate distribution values of the neighbouring nodes (streaming).

It should be noted that it is difficult to consider a significant density contrast of two-phase fluids using the present model, and such conditions require the use of other more appropriate models, such as Shan-Chen and free-energy models (SPENCER; HALLIDAY; CARE, 2010).

Regarding the boundary conditions, four different types are used in the simulations: periodic, half-way bounce-back, constant inlet velocity and convective condition. The first two are simply implemented in the algorithm by properly allocation of distribution functions during the streaming step (see subsection 2.2.3).

The constant velocity boundary condition is based on the work of Zou and He (1997), where the mass and momentum equations (Equation 2.7) are used to calculate the distribution functions specified velocity value and direction.

The convective boundary condition proposed by Lou, Guo and Shi (2013) is also used, where a zero velocity gradient is constrained at the boundary. In the x axis:

$$\partial_t f_i + u_x \partial_x f_i = 0, \tag{3.9}$$

or in the discrete form

$$f_i(x, t+1) = \frac{f_i(x,t) + u_x f_i(x + \Delta x, t+1)}{1 + u_x}. \tag{3.10}$$

To define the velocity u_x it is necessary to take the average value of the velocities in the x direction on nodes located in the first and second neighbouring layers. This condition is used at the outlet of the computational domain, and provides a stable and physically accurate option for the simulation.

The application of those boundary conditions in the computational domain is further explained in section 3.3.

3.2 DIGITAL POROUS MEDIA MODELS

The LB multiphase model is used to simulate drainage in 2D and 3D models. For 2D models, two types are used (Figure 15). The first is a homogeneous model manually produced consisted of circular grains of diameter equal to 20 pixels, spatially distributed to obtain throats with 5 pixels of width and pores in the order of 10 pixels. The image has 400^2 pixels. Porosity and absolute permeability, calculated with a single phase LB model, are 42.0% and 0.84 Darcy, respectively.

The second 2D model consists of a slice of a micro-CT image from a sandpack called LV60A (IMPERIAL COLLEGE CONSORTIUM ON PORE-SCALE MODELLING, 2014b), which is also used for the 3D models. The physical size of the image is 4500.9^2 μm^2 and the digital image size is 450^2 pixels, resulting in a scale of 10.002 μm/pixel. The absolute porosity is obtained from ImageJ software which shows a value of 37.5%. The calculated absolute permeability is 4.04 Darcy.

Figure 15: 2D porous media models: (a) homogeneous produced model and (b) slice of the sandpack LV60A.

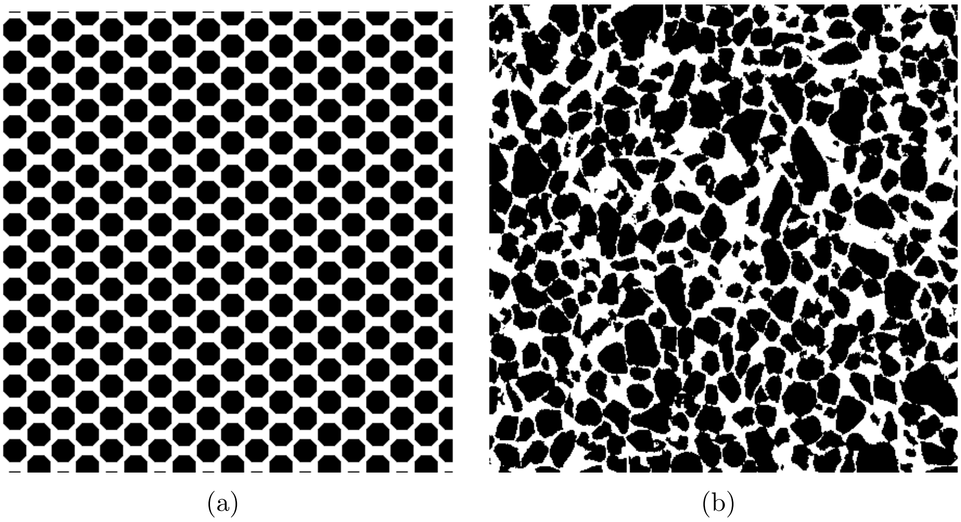
(a) (b)

Source: elaborated by the author.

The 3D digital models are obtained from raw files of micro-CT images of a Berea sandstone (IMPERIAL COLLEGE CONSORTIUM ON PORE-SCALE MODELLING, 2014a) and the sandpack LV60A (IMPERIAL COLLEGE CONSORTIUM ON PORE-SCALE MODELLING, 2014b), for which experimental data of porosity, intrinsic and relative permeabilities and residual saturation are available (RAEINI; BLUNT; BIJELJIC, 2014; MOSTAGHIMI; BLUNT; BIJELJIC, 2013; DONG; BLUNT, 2009; TALABI et al., 2008; RAEINI; BIJELJIC; BLUNT, 2015). Figure 16 shows the 3D representation of the rock models. Berea sandstone is a standard material consisting of quartz with minor amounts of feldspar, dolomite, and clays, which is also widely used for core analysis due to its fine-grained, well-sorted characteristics with closely spaced planar bedding (DONG; BLUNT, 2009). The sandpack LV60A (Leavenseat LV 60) is an industrial sand consisted mainly of quartz and presents broader grain size distribution with more large grains (SAYARI, 2009).

The physical size of the Berea image is 2138^3 μm^3, and the digital image size is 400^3 voxels, resulting in a scale of 5.345 μm/voxel. The LV60A image has a physical size of 4500.9^3 μm^3 and a digital size of 450^3 voxels, resulting in a scale of 10.002 μm/voxel. Both images were sliced to obtain models with 300^3 voxels.

The raw images of the samples are treated using ImageJ software, where a segmentation process is carried out to find an absolute porosity of 19.8% and 39.4%, respectively for Berea and LV60A. This is similar to porosity levels found by Raeini, Bijeljic and Blunt (2015) and Mostaghimi, Blunt and Bijeljic (2013). The raw files are then used as input for the LBM simulations. Single phase displacements are carried out to obtain the absolute permeability of each sample, resulting in 1.55 Darcy and 36.58 Darcy for Berea and

LV60A, respectively. These values are very similar with those reported by Talabi et al. (2008), Dong and Blunt (2009), Mostaghimi, Blunt and Bijeljic (2013) and Raeini, Bijeljic and Blunt (2015).

Table 2 gives a summary on the main parameters of the porous media used in this work.

Figure 16: 3D porous media models: (a) Berea sandstone and (b) sandpack LV60A.

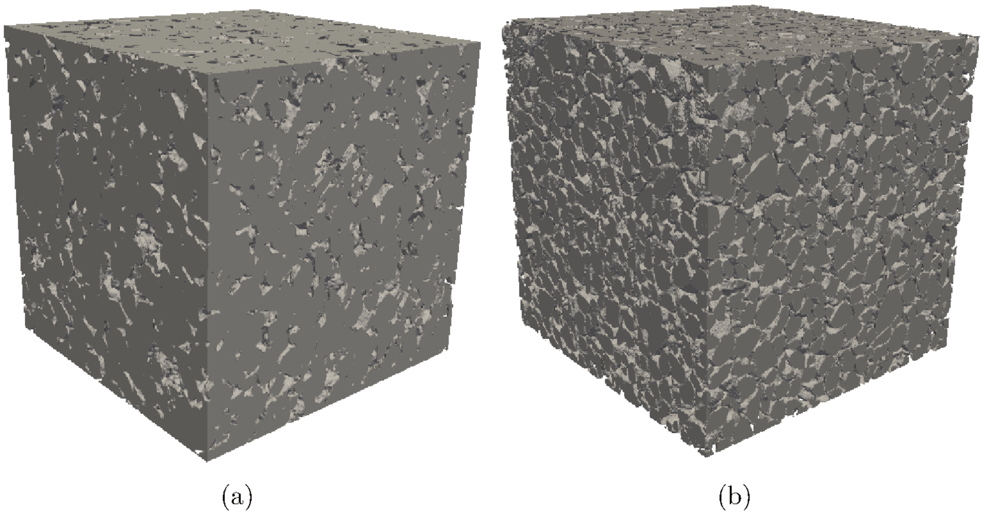
(a) (b)

Source: IMPERIAL COLLEGE CONSORTIUM ON PORE-SCALE MODELLING (2014a, 2014b).

Table 2: Main parameters of the porous media used for the simulations of drainage.

Parameter	**homogeneous**	**LV60A slice**	**LV60A**	**Berea**
Dimensionality	2D	2D	3D	3D
Physical size (μm)	400^2	4500.9^2	3000.6^3	1603.5^3
Image size (pixels)	400	450^2	300^3	300^3
Scale (μm/pixel)	1	10.002	10.002	5.345
Porosity (%)	42.0	37.5	39.4	19.8
Intrinsic permeability (Darcy)	0.84	4.04	36.58	1.55

Source: elaborated by the author.

3.3 SIMULATION SETUP

Viscosity and densities ratios are fixed as 1 for all simulations. Although it was seen that M has an important influence on drainage patterns and residual saturation, the main objective of this work is the evaluation of the effect of Ca alone. Furthermore, to evaluate the combined effect of M and Ca a high number of simulations is needed. This would require considerable computational resources and more time to run simulations, and adding that the digital rock models used in this work are relatively big, this becomes impractical at this time. Thus, the viscosity ratio was fixed in 1 mainly because it is the most robust and stable case which can be studied.

Individual values of viscosities, densities and interfacial tension were chosen considering three criteria: to achieve the desired capillary number, to assure the stability of simulations and to obtain practical time for simulations. If low values of interfacial tension were chosen, for example, the inlet velocity should be lower and total time of simulation would be impracticable. A low value of viscosity would increase the required inlet velocity, however simulation stability would be jeopardized. Several simulations were run to find the best match for the three parameters. Final values of viscosities, densities and interfacial tension were defined, in lattice units, as 0.133 lu^2/ts, 1 mu/lu^3 and 0.0667 mu/ts^2, respectively. This is obtained by setting $\tau_s = 0.9$, $\alpha = 0.1$ and $\beta = 0.9$.

The contact angle is set to 180° ($w_{wr} = 0$), characterizing strong nonwetting condition of red fluid in relation to the solid. Different wetting conditions can affect the displacement process and change the residual saturation during drainage. Thus, only one contact angle is considered to focus on the effect of Ca.

Capillary number is varied by setting different values for constant velocity at the inlet. The continuous displacement method (CHATZIS; MORROW, 1984; MORROW; CHATZIS; TABER, 1988) is used since it is a more practical method for the extensive simulations considered in this work. Each simulation is carried out individually, with same initial conditions and with fixed capillary number calculated using the inlet velocity.

Six individual drainage processes with different Ca are carried out in each porous medium. The Ca range lies between 5×10^{-6} to 1×10^{-3}. Comparing these values with referenced works in the $Ca-M$ diagram, the lowest Ca values are in the range of capillary fingering, where capillary forces are the main driving force, and the highest Ca values are in the transition zone between capillary fingering and stable displacement. Table 3 gives a summary of the fluid parameters used in the simulations.

Table 3: Fluid parameters used in the simulations in lattice units.

Parameter	**Value (lattice units)**
Densities	1
Viscosities	0.133
Interfacial tension	0.0667
τ_s	0.9
α	0.1
β	0.9
θ_r	180°
w_{wr}	0
$\mathbf{u}_{inlet}$	$2.5 \times 10^{-6} - 5 \times 10^{-4}$
Ca	$5 \times 10^{-6} - 1 \times 10^{-3}$

Source: elaborated by the author.

An attempt to simulate higher and lower ranges of Ca was made with 2D porous models. However, at lower Ca ranges, the time taken by simulation to reach breakthrough and quasi-steady states is very long because of low velocity, which makes the condition not feasible. This is even more critical when using 3D porous models. In simulations where

Ca is relatively high, the process diverged at a certain timestep. As seen in section 3.2, the models have low permeability. During the drainage, the nonwetting fluid is trapped in the dead-end pores and thin throats of the porous medium, which generates an obstacle for the flow. The inlet constant velocity boundary injects more nonwetting fluid into this spaces, increasing the fluid density until the density ratio between nonwetting and wetting fluid becomes very large ($\rho_R/\rho_B > 10$). This creates local instabilities near the fluid-fluid interface and simulation diverges.

To overcome those problems, some tests were carried out with different Ca until the definitive range was selected. Furthermore, the high density ratio caused by constant inlet velocity was also an issue in the dead-end pores of the inlet boundary. This was overcome by including a section of fluid nodes with specific width at the inlet of the computational domain. At the outlet, another section of fluid nodes with same width was created. Thus, the computational domain contains an inlet section, the digital porous medium domain, and an outlet section (Figure 17). This slightly increased the simulation time by adding more fluid nodes but it was necessary to assure the stability of the simulations.

No-slip boundary condition is imposed in all solid nodes via a half-way bounce-back scheme, and at laterals, top and bottom faces, periodic boundary condition is imposed. At the inlet, a constant velocity of nonwetting fluid is imposed with the scheme of Zou and He (1997). At the outlet, a convective boundary scheme is imposed based on Lou, Guo and Shi (2013), as seen in section 3.1.

For initial conditions, wetting fluid (blue) is created in all nonsolid nodes, i.e., at timestep zero the porous media is full with wetting fluid. The nonwetting (red) fluid invades the porous media starting from the inlet. Simulations are run until quasi-steady state, which is reached when saturation of nonwetting fluid becomes practically constant over time. The stop criterion is when the calculated relative change of two saturation levels in an interval of 100 timesteps is lower than 10^{-6}. The final irreducible saturation of wetting phase is then obtained from trapped fluid.

Figure 17: Setup of computational domain: (a) the inlet and outlet sections and (b) a 3D schematic of the domain.

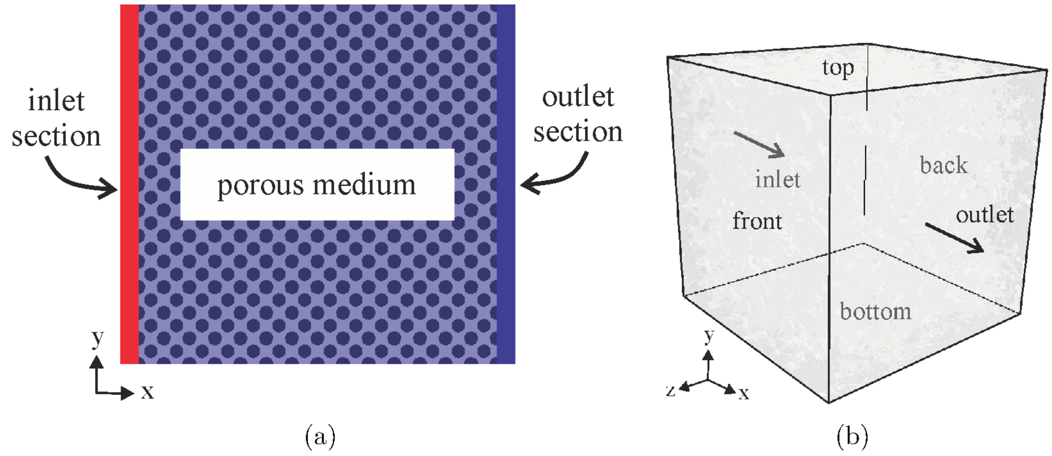

Source: elaborated by the author.

4 RESULTS AND DISCUSSION

This chapter presents the results of simulations in which the methodology proposed in the last chapter was applied. It is divided in three sections.

The fist section shows the results of cases usually applied to verify the LB multiphase model and its capacity to accurately reproduce wettabillity and capillary effects and boundary conditions physical similarity.

Section 2 presents the results using the homogeneous and heterogeneous 2D images. Saturation curves and further results are presented and discussed, comparing with available results in literature.

Section 3 shows the results of simulations using 3D digital rock models and discusses the various phenomena observed, including residual saturation effects caused by different capillary number considered and relative permeability of samples.

4.1 MODEL VERIFICATION

The first case used to verify the proposed LB model is the injection of a nonwetting fluid through two parallel capillary tubes, a case that is used to assess whether the model is able to capture capillary effect and reproduce correct displacement behavior. The lattice domain consists of 200 × 60 nodes and the widths of two capillary tubes are $R_1 = 10$ and $R_2 = 20$ lattices. p_{c1} and p_{c2} are the corresponding capillary pressures. A uniform pressure is imposed at the inlet and at the outlet (p_{in} and p_{out}, respectively). Initially, the invading nonwetting fluid is located at the entrance of the domain. The displacement behavior is determined by the pressure difference between the inlet and the outlet, $\Delta p = p_{in} - p_{out}$, and the capillary pressures. The simulation parameters are set, in lattice units, as $\rho_w = \rho_{nw} = 1.0$, $\nu_w = \nu_{nw} = 1/3$, $\sigma = 0.0667$ and $\theta_{nw} = 180°$. α and β values are 0.1 and 0.9, respectively. With those parameters, the capillary pressures can be calculated by Young-Laplace equation (2.3), and their values, in lattice units, are $p_{c1} = 0.01333$ and $p_{c2} = 0.00667$. Three different pressure differences are simulated in this test case: $\Delta p = 0.005$, 0.01 and 0.015. The corresponding simulation results are shown in Figure 18, where red fluid is nonwetting and blue fluid is wetting. When Δp is smaller than p_{c2}, the invading fluid cannot enter both capillary tubes. When Δp is between p_{c2} and p_{c1}, the nonwetting fluid only flows into the larger capillary tube. When the pressure difference is increased to $\Delta p > p_{c1}$, the invading fluid flows into both capillary tubes, but the displacement is much faster in the larger capillary tube.

A second test is conducted to check the ability of the model in relating the pressure difference, radius of curvature and interfacial tension in the situation that a droplet of one fluid is immersed in another fluid. The pressure difference in this case is given by Laplace law for a 2D droplet:

$$\Delta p = \frac{\sigma}{r}, \tag{4.1}$$

where r is the droplet radius.

Initially, a square droplet of nonwetting fluid is created in the center of a 100 × 100 lu^2 system filled with wetting fluid. All boundaries are periodic. Density and viscosity ratios are 1 and $\beta = 0.9$. The system is left to relax until a steady circle of nonwetting fluid appears. The pressure difference between fluids and the droplet diameter are measured.

Figure 18: Injection of nonwetting fluid into two parallel capillary tubes: (a) $\Delta p = 0.005$, (b) $\Delta p = 0.01$ and (c) $\Delta p = 0.015$.

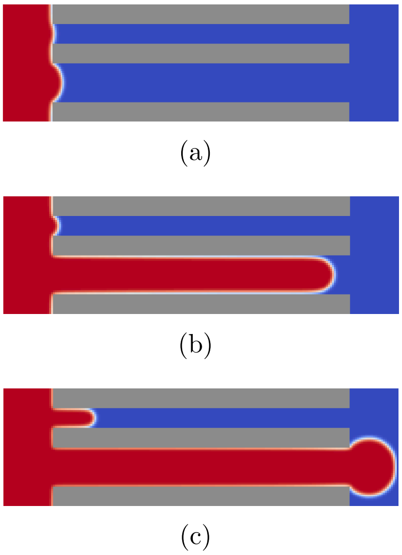
(a)

(b)

(c)

Source: elaborated by the author.

It should be noted that in the present model, at a site predominately occupied by one of the fluids, there can be a small amount of dissolved component of another fluid. In the present case, a threshold is applied at $S_{nw} = 0.5$ to define the interface between fluids. Furthermore, due to the discrete characteristic of the method, the droplet diameter is determined in integer values. Thus, small variations of the droplet radius caused by different interfacial forces, for example, are difficult to capture.

The results of tests considering different initial droplet sizes and different α are presented in Figure 19. The pressure difference inside and outside of the droplet is proportional to the reciprocal of the droplet radius for all α values as expected by Laplace law. It is also clear that the slope of fitted lines (interfacial tension) increases for increasing α. This is expected since the interfacial tension is proportional to α as shown in Equation 3.5. The solid lines represent linear fitting curves with the coefficient of determination $R^2 > 0.998$ for all cases.

A third test is used to verify the wettability conditions of the model by evaluating the equilibrium contact angle of a 2D droplet placed on a solid wall. A 200×100 lu^2 lattice domain is created where a 40×40 lu^2 square of red fluid is placed in contact with the bottom solid boundary, while the rest of the domain is filled with blue fluid. Periodic boundary condition is imposed at top, left and right boundaries. Density ratio is 1.0, $\tau_{red} = \tau_{blue} = 0.9$, $\alpha = 0.1$ and $\beta = 0.9$. Simulation is carried out until steady state. As shown in Figure 20, different contact angles can be achieved by adjusting the concentration of red fluid at the wall w_{wr} according to Equation 3.8. In simulations with porous media, $w_{wr} = 0$ resulting in strongly nonwetting condition as shown in Figure 20(a).

The last test is carried out to verify qualitatively the implemented convective boundary condition based on Lou, Guo and Shi (2013). A droplet of nonwetting fluid is created in a channel with length $L = 400$ and height $H = 80$ lattice nodes. Solid nodes are created at top and bottom boundaries, Neumann constant velocity boundary condition is imposed at the left inlet and the convective boundary condition at the right outlet. Then, the droplet is moved by imposing a constant and low velocity of wetting fluid at

Figure 19: Relationship between pressure difference between fluids and droplet radius for the bubble tests.

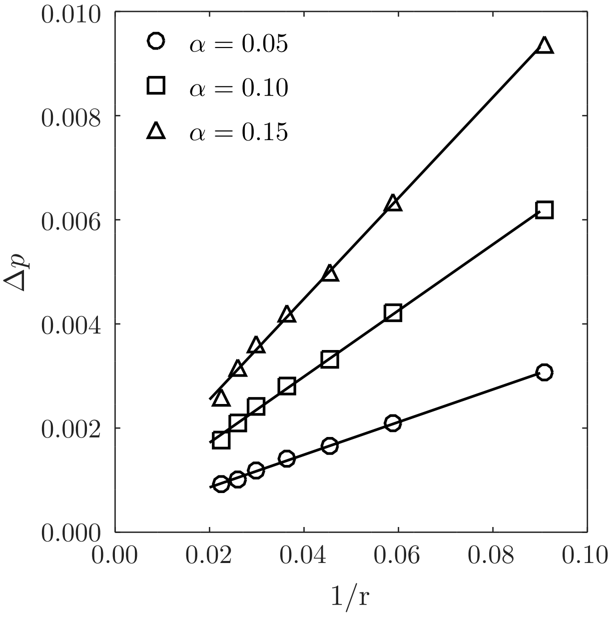

Source: elaborated by the author.

Figure 20: Droplet on a solid surface with different values of concentration of red fluid at the wall: $w_{wr} = 0.0$ (a), 0.25 (b), 0.5 (c), 0.75 (d) and 1.0 (e).

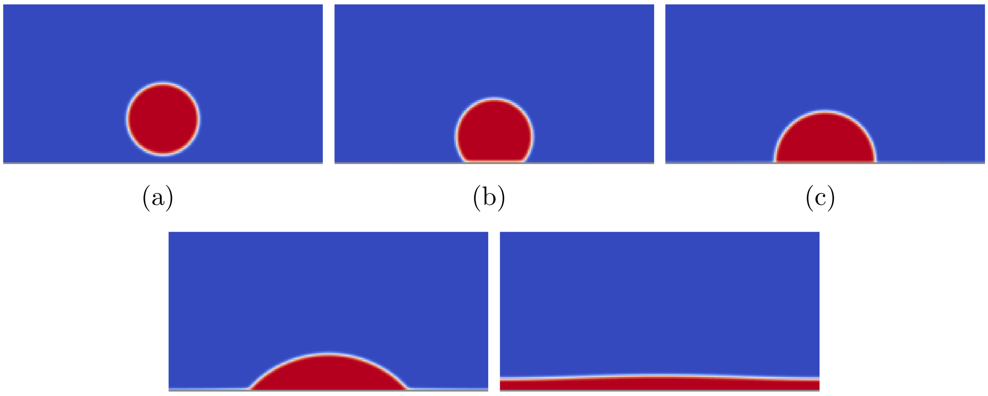

(a) (b) (c)

(d) (e)

Source: elaborated by the author.

the channel inlet. The droplet moves toward the outlet and leaves the channel. Figure 21 shows the resulting phenomenon. Similar result is demonstrated by Lou, Guo and Shi (2013), who compared the physical behavior with other types of outflow boundary condition, and showed that the convective boundary condition gives a more reasonable prediction of interface behavior.

4.2 RESULTS WITH 2D POROUS MODELS

This section presents and discuss the results of drainage displacements in the 2D porous models shown in section 3.2, starting with the homogeneous model manually

Figure 21: Snapshots of the droplet with the outlet convective boundary condition at different times.

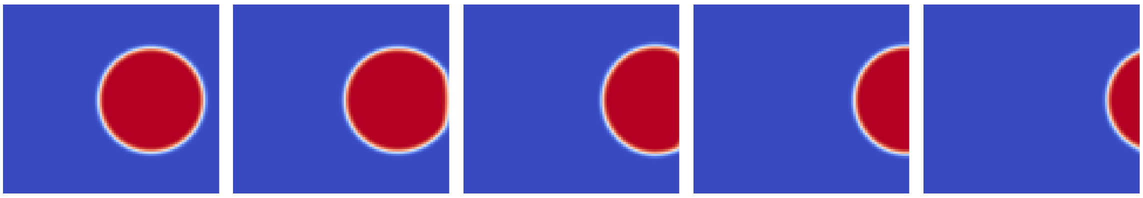

(a) (b) (c) (d) (e)

Source: elaborated by the author.

produced and following the heterogeneous model consisted of a slice of the LV60A digital rock model. Parameters and setup of simulations are defined in section 3.3.

4.2.1 Drainage in the homogeneous model

The first case analyzed is the drainage in the homogeneous 2D model manually produced. Figure 22 shows snapshots of the displacement process with $Ca = 5.0 \times 10^{-5}$ at different times, where red is the nonwetting fluid, blue is the wetting fluid and gray represents the solid grains. The nonwetting fluid starts to enter the domain from inlet and invades the narrow spaces occupied by the wetting fluid, creating the first fingers by selecting paths where required capillary pressure is lower. As time increases, more space is occupied by the nonwetting fluid, while part of the wetting fluid leaves the porous medium through the outlet and other part is trapped inside the pores. The fingers grow towards the outlet of the domain reaching the breakthrough (BT). After BT, the nonwetting fluid invades pores in other areas creating new fingers until final quasi-steady (QS) state is reached. This aspect is not exactly the same in cases with different Ca.

Figure 22: Snapshots of drainage in the homogeneous 2D model with $Ca = 5.0 \times 10^{-5}$ at different timesteps:(a) 20,0000, (b) 1,640,000, (c) 2,670,000 and (d) 4,560,000.

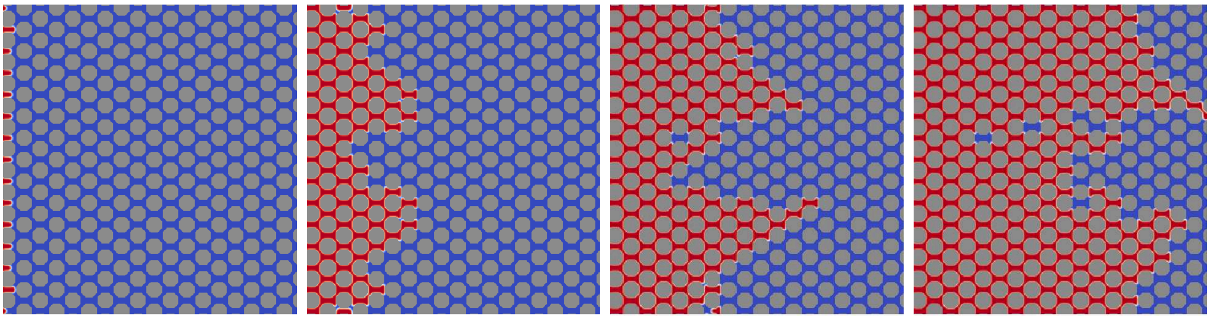

(a) (b) (c) (d)

Source: elaborated by the author.

In Figure 23, snapshots at half breakthrough time, breakthrough and quasi-steady state of four simulated cases are compared. Two displacement patterns characterized by Lenormand, Touboul and Zarcone (1988) are found, which are dependent on the value of Ca. When Ca is high (Figures 23(a)-(c)), stable displacement is achieved due to higher inertial and viscous forces of the invading fluid. The nonwetting fluid has a uniform frontal flow, sweeping a broad area the porous medium at the same time and leaving a low amount of trapped wetting fluid behind the nonwetting fluid front. There is a small difference on saturation condition between BT and QS states.

An intermediate crossover pattern is observed when $Ca = 5.0 \times 10^{-4}$ (Figure 23(d)-(f)), where it is not possible to determine between capillary fingering and stable displacement. The displacement is nearly uniform and a few fingers grow ahead of the nonwetting fluid front, leading to a higher amount of trapped wetting fluid than in stable displacement.

Capillary fingering occurs when Ca decreases (Figures 23(g)-(i) and (j)-(l)). Nonwetting fluid flows through preferential paths which provide less resistance to flow, creating fingers that spread across the network and grow in all directions. After reaching BT, the nonwetting fluid slowly invades further pores and saturation increases imperceptible until simulation reaches QS state. There is practically no difference between BT and QS state.

Although Figures 23(g)-(i) and (j)-(l) are characterized as capillary fingering because of similar invasion mechanisms during drainage, the final conditions are very different. This occurs because of the velocity of pore filling events and the geometry of the medium, which affect the trapping mechanisms during the process and hence the residual wetting saturation. In the following, this phenomenon is explained in more details.

Viscous fingering is not observed in present cases since viscosity ratio is 1. As seen in section 2.3, the viscosity of wetting fluid should be higher than the viscosity of nonwetting fluid to achieve viscous fingering. Furthermore, when creating the model of a homogeneous porous medium, Lenormand, Touboul and Zarcone (1988) produced small geometric perturbations to facilitate the development of preferential paths for the fluid. In the present case, the homogeneous model was created with regular sizes of pores and throats. However, the periodic condition that connects the upper and lower boundaries provide a small perturbation since circular grains at those boundaries are not similar as the rest of the geometry. This is similar to what occurs in microfluidic experiments where periodic boundaries are difficult to implement and the model solid boundaries always represent a perturbation in the medium.

Figure 24 shows the relationship between S_{nw} and normalized frontal location of nonwetting fluid during drainage in the homogeneous model. This refers to the distance from the inlet to the most deeply penetrated nonwetting fluid in the porous medium. The color of each curve represents the pattern observed in the snapshots: stable displacement is represented in blue, crossover in green and capillary fingering in red.

In stable displacement and crossover patterns, the frontal location of nonwetting fluid increases in a uniform step-like behavior, which indicates a linear increase of saturation and position of frontal fingers with time. The steps occur due to the identical shape of the grains uniformly spaced in the medium, and in the case of the crossover pattern they occur also due to localized capillary fingering mechanisms.

Capillary fingering curves present also step-like behavior, but the steps are larger, suggesting that the saturation of the nonwetting phase increases considerable while the most advanced finger remains stationary. This is caused by side or backward movements of the nonwetting phase, which increases the S_{nw} behind the front line, and reflects the domination of localized pore-scale capillary forces in this fingering regime. Furthermore, the effect of different flow patterns of Figures 23(g)-(i) caused by the pore filling events can be seen in Figure 24. The capillary fingering curves with a more uniform step-like behavior are relative to the lowest Ca range, while the cases with intermediate Ca present more disordered step-like behavior and lower S_{nw} for the same value of the frontal location.

The step-like behavior of capillary fingering pattern in Figure 24 is better explained

Figure 23: Snapshots of drainage in the homogeneous 2D model at half breakthrough time, breakthrough and quasi-steady state with four different Ca: (a)-(c) 1.0×10^{-3}, (d)-(f) 5.0×10^{-4}, (g)-(i) 1.0×10^{-4} and (j)-(l) 1.0×10^{-5}.

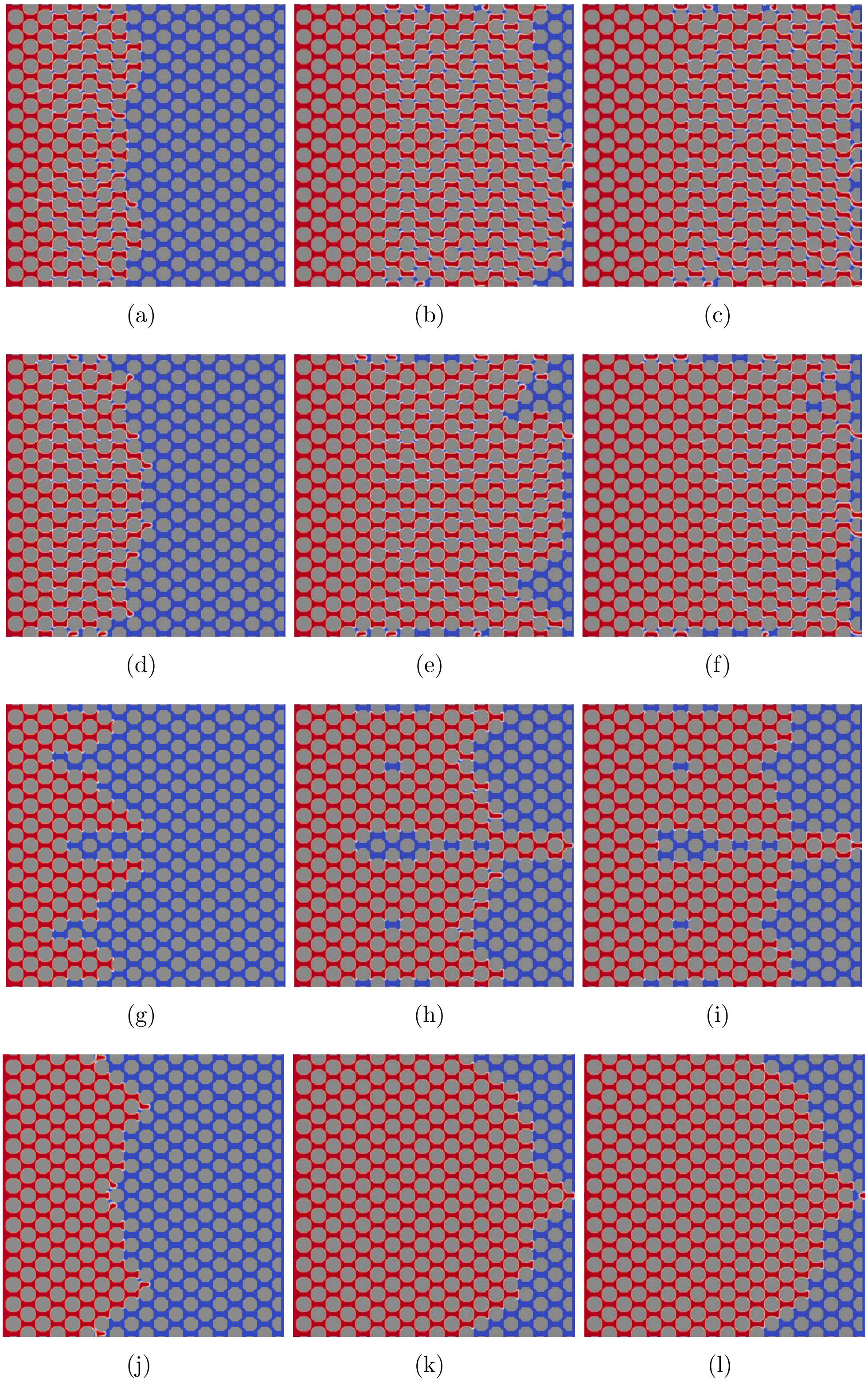

(a) (b) (c)

(d) (e) (f)

(g) (h) (i)

(j) (k) (l)

Source: elaborated by the author.

by looking into the pore-scale events during drainage. Figure 25 shows snapshots of pore filling events at the most advanced finger during drainage with $Ca = 5.0 \times 10^{-5}$. The

Figure 24: Relationship between normalized frontal location and saturation of nonwetting fluid for drainage in the homogeneous 2D model. The color of each curve represents the pattern observed in the snapshots.

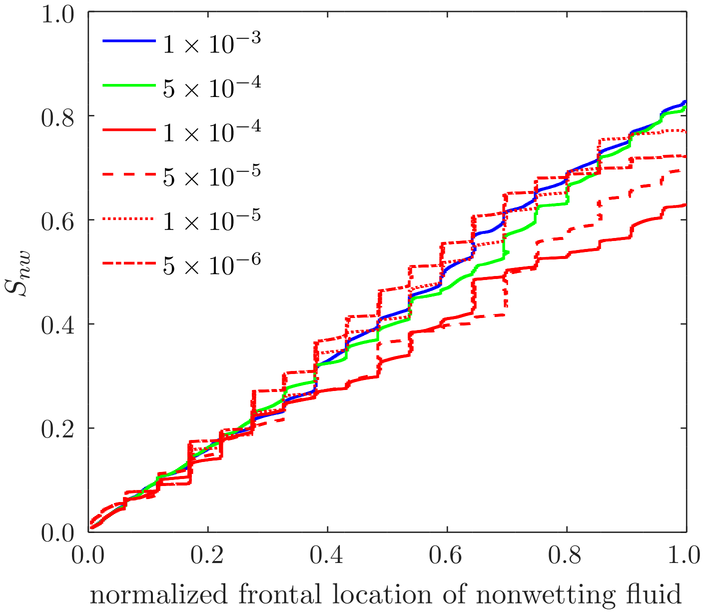

Source: elaborated by the author.

timesteps in which the snapshots are taken are around the same timestep of Figure 22(c), where the finger is visible. The location of the events is relative to the considerable increase in S_{nw} curve at about 0.65 of the normalized frontal location for the capillary fingering curves in Figure 24. Two Haines jumps are observed: the first forward and the second backward.

During the Haines jumps, the nonwetting fluid front at the entrance of a thin throat reaches the required pressure to enter the throat, and moves slowly until it finds the throat exit. At this point, the fluid reaches the entrance of a pore, which has a bigger size and lower required capillary pressure. This causes the nonwetting fluid to increase its velocity, immediately invading the pore, while an instantaneous drop in the concentrated pressure occurs. The movement stops once the nonwetting fluid finds other throats at the exit of the pore (HAINES, 1930; SUN; SANTAMARINA, 2019).

To demonstrate the relative high velocity of the pore filling event, the time gap between each snapshot was measured. For example, the time gap between Figures 25(c) and (d) is around 20 times higher than between Figures 25(e) and (f). This shows that the pore filling events and migration of fingers are governed by local flow dynamics and that inertial effects at pore-scale might play an important role in the capillary fingering regime (TSUJI; JIANG; CHRISTENSEN, 2016).

A subtle imbibition in surrounding pores occurs during the Haines jumps due to the fluid redistribution. Although this imbibition is almost negligible at the pore-scale, it happens in various pores across the medium at the same time. One Haines jump can affect the fluid distribution in pores located far from where it occurs, and the combined effect causes significant trapping of wetting fluid. Comparing the location of this finger in Figures 22(c) and (d), it is possible to observe that the finger stops to move forward after the backward Haines jump. It is surpassed by fingers growing in other areas. This is probably caused by subsequent fluid redistribution, i.e., Haines jumps occurring in

Figure 25: Snapshots of pore filling events during drainage in the homogeneous 2D model with $Ca = 5.0 \times 10^{-5}$.

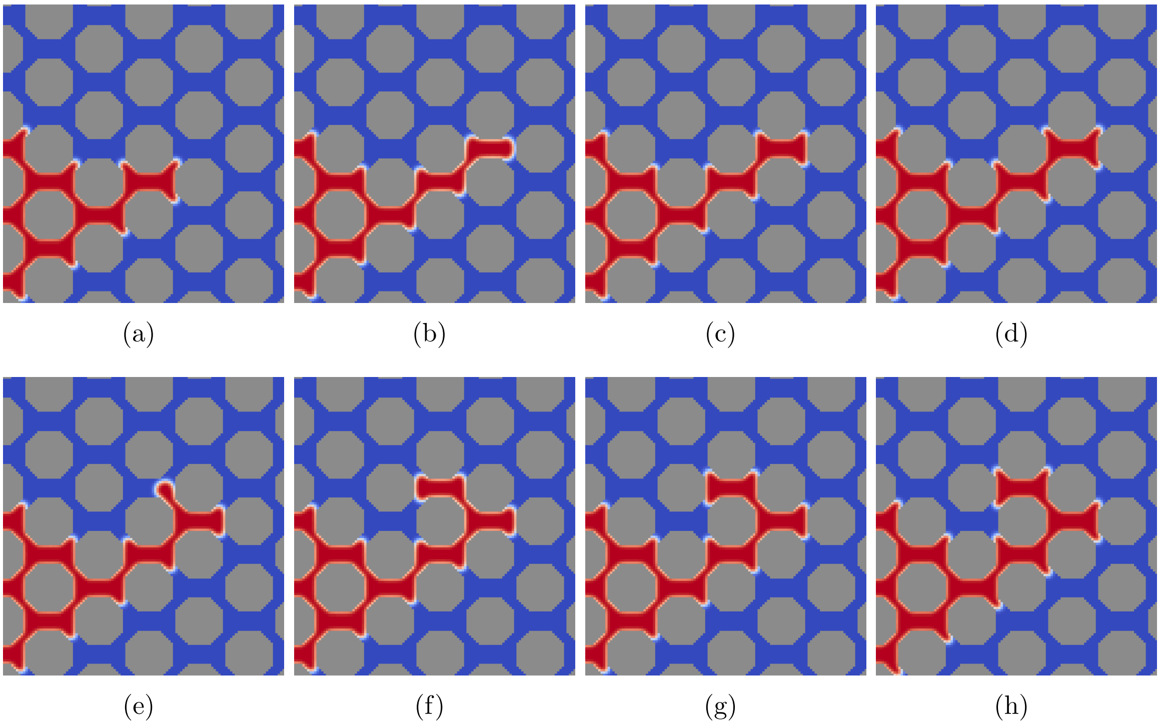

Source: elaborated by the author.

surrounding areas redistribute the fluid in such way that the pressure in the finger front does not reach the required value to enter further throats. Furthermore, as shown Figure 25(h), the wetting fluid is trapped behind this nonwetting fluid finger and remains until quasi-steady state is reached.

The increase of nonwetting fluid saturation with time is shown in Figure 26, where timestep is normalized. The red markers represent the time when breakthrough occurs for each case. In some cases, the rate of increase in S_{nw} decreases considerably after BT. As shown in Figure 23, the nonwetting fluid creates fingers that grow towards the outlet creating preferential paths. Considerable part of the fluid flows through those paths after BT avoiding enter further pores and throats because a higher pressure is necessary. The increase in S_{nw} at this stage is due to the slow invasion in other areas of the porous medium which are not connected with the preferential path.

In some cases the QS state is reached right after BT. In this 2D model, individual stop criterion for each case had to be defined to achieve consistent results. The stop criterion is defined in the present work as the relative difference of S_{nw} measured each 100 timesteps. At high Ca, if the stop criterion was low, the simulation would run considerable time after breakthrough. The nonwetting fluid would keep invading further pores by the continuously increase in pressure, reaching higher values of S_{nw}. However, simulations could diverge because of high density ratios ($\rho_R/\rho_B > 10$) related to the increase in pressure.

At low Ca, a high stop criterion would inhibit the simulation to reach breakthrough because of the low invasion rate. Furthermore, if stop criterion is too low, simulations would take a long time to finish but high values of S_{nw} could be achieved. This is the reason that final state in present simulations is called quasi-steady state and that several works referenced in section 2.3 use only the breakthrough point to evaluate the saturation

Figure 26: Nonwetting fluid saturation as a function of normalized timestep during drainage in the homogeneous 2D model. The red marker indicates the breakthrough point.

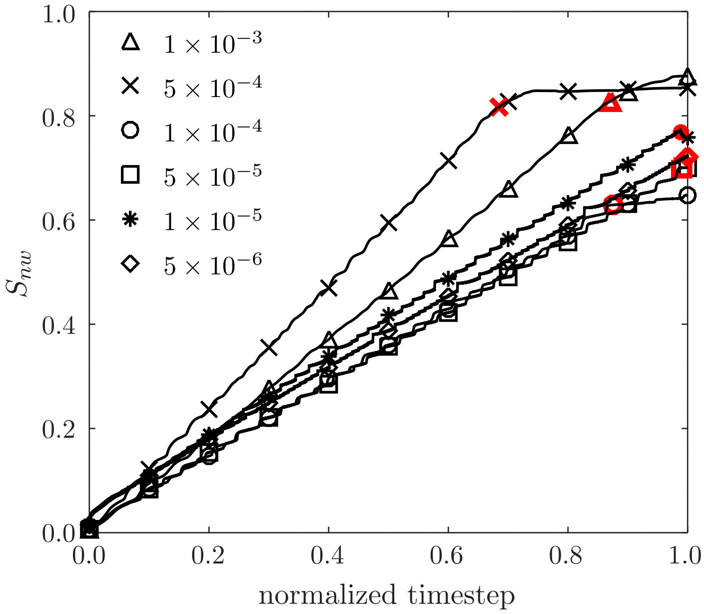

Source: elaborated by the author.

during drainage. In the present work, the stop criterion of 2D cases was set after several trials to assure stability and feasibility of simulations, and to assure that breakthrough and further quasi-steady states were achieved.

In Figure 27, the total time to reach BT and QS state is plotted in a log-log chart as a function of Ca. At both moments, the total time of simulation increases considerably as Ca decreases because of lower velocity of nonwetting fluid invasion. Furthermore, for low Ca cases, the time to reach QS is practically the same as BT time. As explained earlier, after BT, the nonwetting fluid avoids to enter further pores and throats and flows mainly through the preferential path created, and stop criterion is found quickly.

Time in Figure 27 is the lattice timestep in simulations. The equivalent physical time of the drainage process can be calculated with Equation 2.19 by using usual values of viscosity and interfacial tension of water (wetting fluid) and oil (nonwetting fluid). Those values vary considerably between different reservoirs, but the order of magnitude is usually similar. Therefore, the calculated order of magnitude of the physical time of the process is about 1 s and 1000 s for the highest and lowest Ca cases, respectively.

Figure 28 shows the wetting fluid saturation at breakthrough and quasi-steady state as a function of Ca in the 2D homogeneous model. The two cases with the highest Ca values yield the lowest amount of residual wetting fluid saturation at both BT and QS. By comparing the snapshots in Figure 23, it is clear that the stable displacement pattern had a more efficient sweeping effect. The viscous forces of the invading fluid play an important role in this process.

The cases with $Ca = 1.0 \times 10^{-4}$ and $Ca = 5.0 \times 10^{-5}$ yield a higher S_w at BT and QS. This is explained by analyzing Figures 22(d) and 23(i). At this Ca range, the nonwetting fluid creates fingers which grow quickly towards the outlet because of fast pore filling events. This causes a high amount of trapped wetting fluid behind the finger front. Furthermore, after the BT, the fingers stop to grow in other directions and nonwetting

Figure 27: Timestep at breakthrough and quasi-steady state as a function of the Ca for drainage in the homogeneous 2D model.

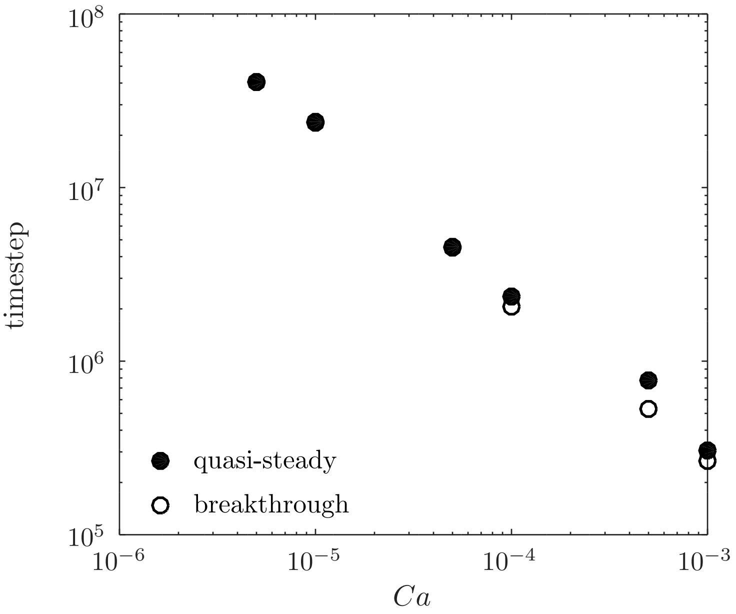

Source: elaborated by the author.

fluid flows mainly through the preferential path created. This results in a high amount of wetting fluid remaining in the outlet area.

Figure 28: Wetting fluid saturation as a function of Ca at breakthrough and quasi-steady state for drainage in the homogeneous 2D model.

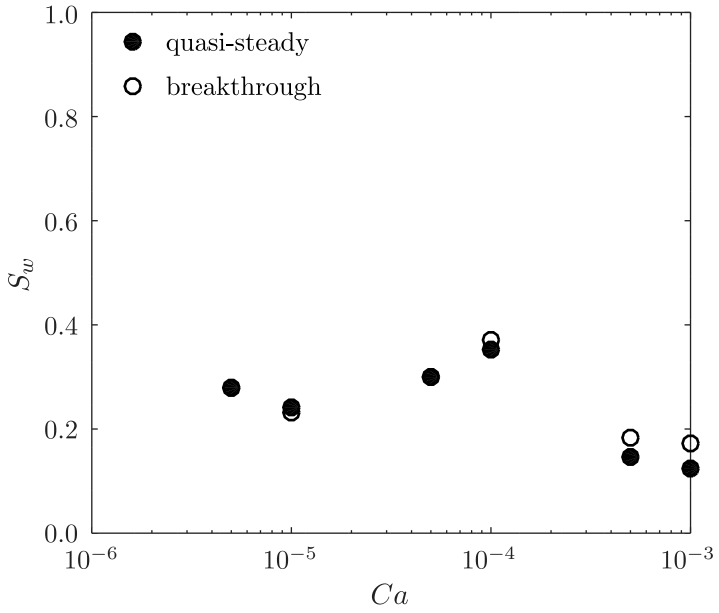

Source: elaborated by the author.

The low values of S_w in the cases with $Ca = 5.0 \times 10^{-6}$ and $Ca = 1.0 \times 10^{-5}$ are explained by looking at the pore filling mechanisms during drainage, which produce the pattern observed in Figures 23(j)-(l). At this Ca range, the drainage is consisted of consecutive Haines jumps at low rate. This provides more time for the fluid to redistribute in the surrounding areas and hence reduces the trapping of wetting fluid. To compare the velocity of pore filling events, with $Ca = 1.0 \times 10^{-5}$ the time of each Haines jumps is around five times longer than with $Ca = 5.0 \times 10^{-5}$. Furthermore, the intrinsic characteristic of the present homogeneous model, with similar sizes of grains uniformly distributed and without dead-end pores, provides a better condition for a uniform redistribution of the fluid during the pore filling events. This prevents the trapping of wetting fluid behind the nonwetting fluid front, which occurs frequently in intermediate Ca cases. However, a considerable amount of wetting fluid still remains in the outlet area caused by the early breakthrough of the fingers, resulting in higher residual wetting saturation than with high Ca values.

4.2.2 Drainage in the heterogeneous model

An example of drainage in the 2D slice of LV60A is illustrated in Figure 29 for the case with $Ca = 5.0 \times 10^{-5}$ at different timesteps. As the nonwetting fluid invades the porous medium, the fingers grow by selecting the path with less resistance, i.e., the path where pores and throats are bigger and yield lower capillary pressure. Furthermore, in this case the medium is heterogeneous. The geometry of pores and throats is very irregular, which creates various dead-end pores where fluid gets trapped and do not contribute to the flow. Those characteristics lead to finger growing in various directions at the same time, resulting in a higher amount of trapped wetting fluid. This is more clear when Figures 29 and 22 are compared.

Figure 29: Snapshots of drainage in the LV60A 2D model with $Ca = 5.0 \times 10^{-5}$ at different timesteps:(a) 770,000, (b) 2,300,000, (c) 3,280,000 and (d) 3,610,000.

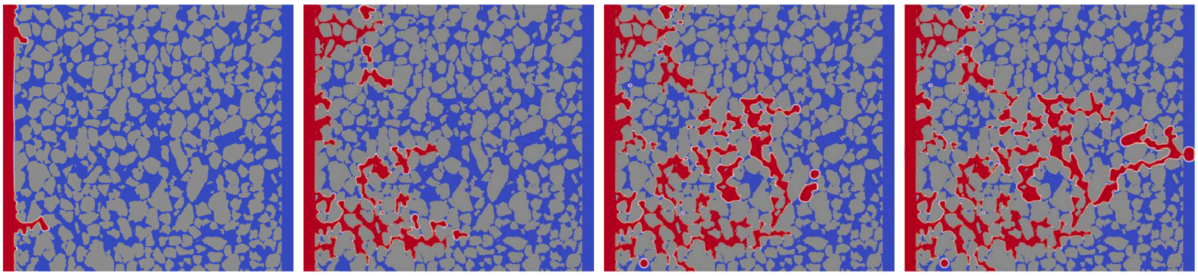

(a) (b) (c) (d)

Source: elaborated by the author.

In Figure 30, snapshots at half breakthrough time, breakthrough and quasi-steady state are compared for four simulated cases. In this case, stable displacement at high Ca is not observed, mainly because of the medium heterogeneity. Dead-end pores and thin throats break the uniform advance of the flow and causes an unstable displacement, where the fluid usually selects bigger pores and throats as in capillary fingering, but it is also capable to flow through the thin throats because of the momentum provided by viscous forces. This creates larger fingers and leads to higher fluid connectivity as the fluid continues to invade further areas after BT. By decreasing the Ca, capillary fingering is achieved where the main characteristic is the selectivity of the fluid for paths with lower capillary pressure.

In the snapshots at breakthrough, one clear preferential path through the outlet is found in all cases, i.e., the fluid flows through the same path with the lowest capillary pressure despite the difference in flow rate. This is an important characteristic for oil recovery, specially because Ca ranges are usually lower in typical reservoirs. If the preferential paths of a reservoir are identified, it would be possible to decide the location of the extraction wells that would yield lower fluid trapping. However, the real process is much more complex and must be verified with subsequent imbibition and drainage processes in 3D models considering the importance of the dimensionality and of a reliable REV.

The cases with higher Ca show less trapped wetting fluid at QS state. Big clusters of wetting fluid are found in the same areas in all cases because of dead-end pores. For example, near the inlet, where a big cluster remains trapped at QS state even in high Ca cases.

Figure 31 shows the relationship between normalized frontal location of nonwetting fluid and S_{nw} during drainage. The unstable displacement is represented in green and capillary fingering in red. In unstable displacement, the frontal location of nonwetting fluid increases smoothly with a few instabilities at some points caused by local capillary fingering mechanisms. As in the homogeneous model, capillary fingering presents a step-like behavior, suggesting side or backward movements of the nonwetting phase while the most advanced finger remains at the same location. However, the steps are not regular as in the homogeneous model. When the fluid finds an obstruction provided by dead-end pores or thin throats, the saturation increases constantly until a new path is found. This is highly dependent on the geometry of pores and throats, which in this case is very irregular compared to the homogeneous model. Furthermore, the subtle increases in S_{nw} occur nearly at the same location in all cases of unstable displacement and capillary fingering regimes, which confirms the presence of a preferential path even at different Ca.

Figure 32 shows snapshots of a fluid's selectivity event during drainage with $Ca = 5.0 \times 10^{-5}$. The timesteps in which the snapshots are taken are around the same timestep of Figure 29(b), and the event is occurring in the second most advanced finger. This location is relative to the step at about 0.57 of the normalized frontal location curve for the capillary fingering case in Figure 31. The step occurs because the most advanced finger is blocked while the events are happening in the second most advanced finger.

In the beginning, two fronts of the nonwetting fluid are observed (Figure 32(a)). The front A is obstructed by a thin throat while front B is invading two throats. The first movement observed (Figure 32(b)) is the breakthrough of front A while front B selects a preferential throat to flow, enters a dead-end pore and is disconnected front the main flow. In the next moment, front A moves in two directions, backward and forward, to the entrance of two opposite pores (Figure 32(c)). The backward pore has a larger size entrance, which would provide less resistance. However, when front A reaches the entrance of the forward pore, it finds a path with lower required capillary pressure and moves towards this pore (Figure 32(d)). Part of the fluid that is invading the backward throat moves to the opposite side accompanying the flow. This occurs because the pore in the backward direction is a dead-end pore which its only exit is already filled by nonwetting fluid. This shows that the fluid's selectivity is also influenced by surrounding fluid fronts. The main cause is still the capillary force: the two fronts of nonwetting fluid pushes the wetting fluid inside the dead-end pore, increasing wetting fluid pressure and consequently increasing the required capillary pressure. Once front A tries to enter this pore, it finds a higher resistance and selects the opposite pore.

Front A and B continue to move in the selected direction (Figures 32(e) and (f)).

Figure 30: Snapshots of drainage in the LV60A slice model at half breakthrough time, breakthrough and quasi-steady state with four different Ca: (a)-(c) 1.0×10^{-3}, (d)-(f) 5.0×10^{-4}, (g)-(i) 1.0×10^{-4} and (j)-(l) 1.0×10^{-5}.

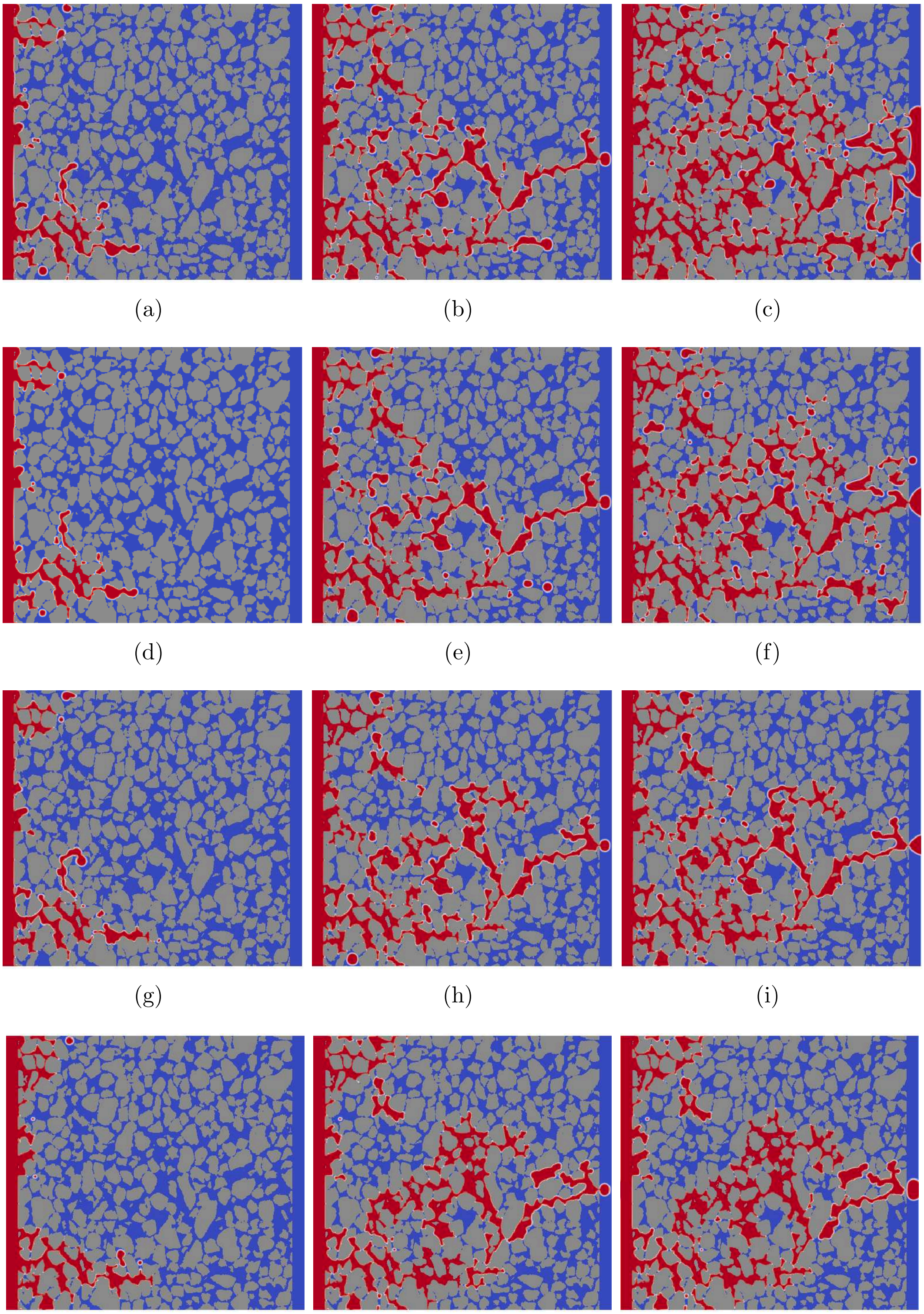

(a) (b) (c)

(d) (e) (f)

(g) (h) (i)

(j) (k) (l)

Source: elaborated by the author.

However, since front B is disconnected front the main flow, it gets trapped inside a dead-end pore. The flow behind the front B selects a different path, towards front A (Figure

Figure 31: Relationship between normalized frontal location and saturation of nonwetting fluid for drainage in the LV60A slice model. The color of each curve represents the pattern observed in the snapshots.

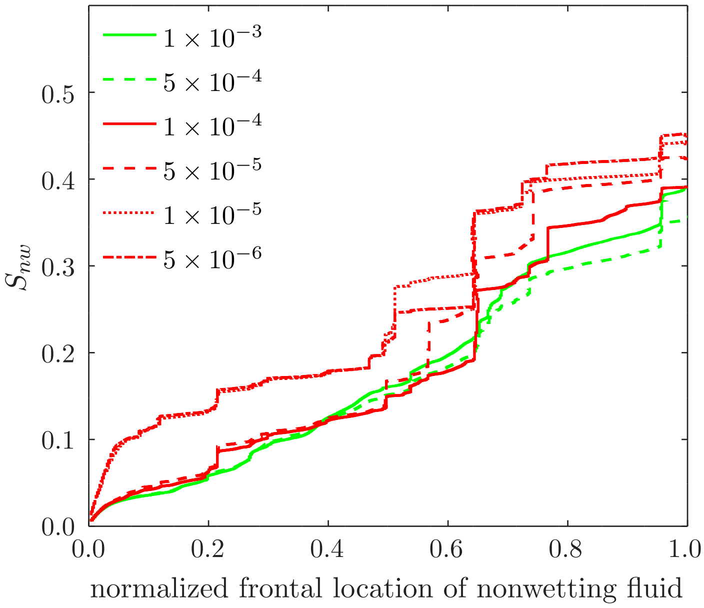

Source: elaborated by the author.

32(g)).

This type of event is frequent during the entire drainage and causes considerable amount of trapping of nonwetting and wetting fluid inside dead-end pores. It illustrates how invading fluid selects the direction of migration similar to the phenomena during drainage in a pore doublet (CHATZIS; DULLIEN, 1983; WOLF; SANTOS; PHILIPPI, 2008), but in a higher scale and including several pores. Furthermore, in the capillary fingering regime frequent Haines jumps as those showed in Figure 25 occur, and can be more intense due to higher pore-throat size ratio.

Figure 32(h) shows the final saturation condition at this location. The flow selected a different path to move forward. The fluid clusters located in the surrounding areas of the main path are very disconnected because of the thin throats and dead-end pores.

The increase of nonwetting fluid saturation with time is shown in Figure 33, where timestep is normalized. In this case, the definition of stop criteria followed the same considerations as in the homogeneous model. Each case had to be treated individually to achieve consistent and practical simulations. Although in some cases the rate of increase of S_{nw} seems high at final timesteps, the QS state is found because of the quick drop in the rate at the last timesteps. When $Ca = 5.0 \times 10^{-5}$, for example, the QS state is reached right after BT. Once the nonwetting fluid finds the preferential path, it avoids enter further pores or throats. The viscous forces are small and do not contribute for further pore invasion as in higher Ca cases. This causes a subtle decrease in the rate of increase of saturation after BT and stop criterion is found quickly. At high Ca, the fluid finds a preferential path faster due to the viscous forces, and BT is reached earlier. The fluid keeps invading the porous medium and the saturation increases considerable before reaching QS state.

This characteristic is also shown in Figure 34, where the wetting fluid saturation at breakthrough and quasi-steady state are plotted as a function of the Ca. The cases with

Figure 32: Snapshots of pore filling events during drainage in the LV60A slice model with $Ca = 5.0 \times 10^{-5}$.

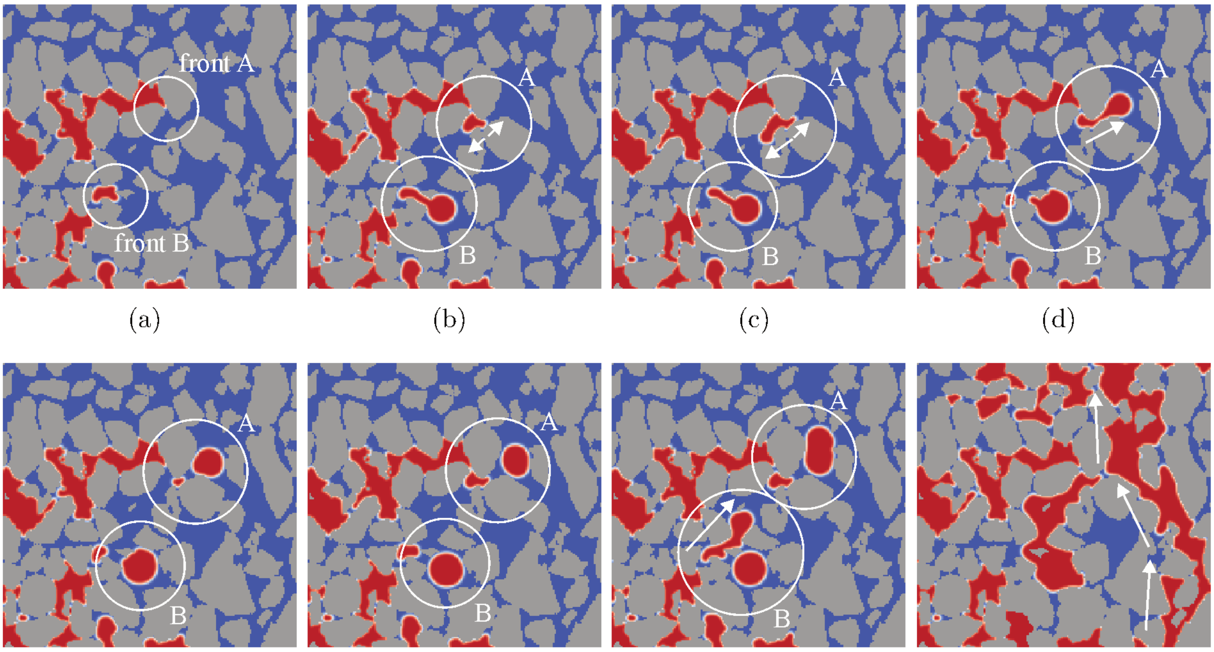

(a) (b) (c) (d)

(e) (f) (g) (h)

Source: elaborated by the author.

Figure 33: Nonwetting fluid saturation as a function of normalized timestep during drainage in the LV60A slice model. The red marker indicates the breakthrough point.

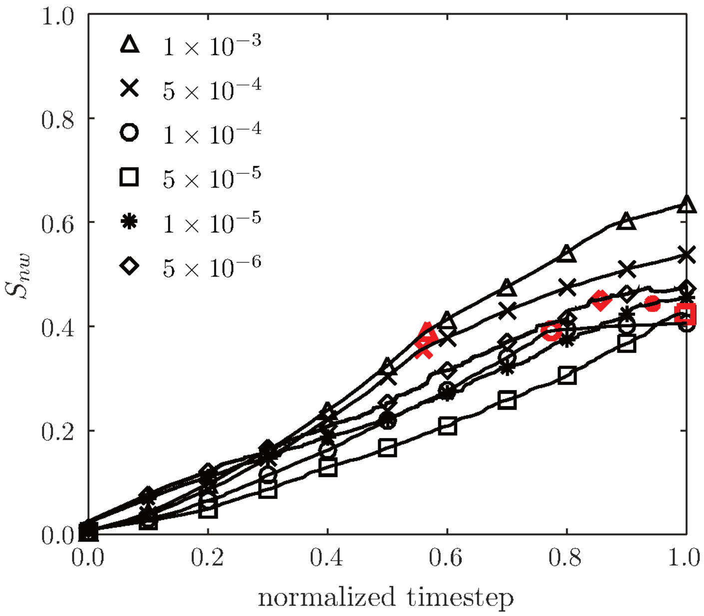

Source: elaborated by the author.

high Ca have higher residual S_w at BT but lower residual S_w at QS state. Comparing Figures 34 and 28, a difference is found between homogeneous and heterogeneous cases. This can be explained by the different patterns observed in Figures 30 and 23. In the homogeneous model, the stable displacement with a uniform front of the nonwetting fluid sweeps a larger area of the porous medium and S_w at BT is close to saturation at QS state. The S_w difference between BT and QS state is higher in the heterogeneous medium at high Ca. The irregular geometry of pores and throats produces an unstable displacement, where the fluid finds a preferential path and do not sweeps a considerable area of the medium. This leads to an early BT, with lower wetting fluid saturation. However, due to the viscous forces the fluid keeps invading further pores, and S_w at QS state is much lower. This shows the importance of evaluating the quasi-steady state because the effect of Ca on residual saturation can be different at BT in distinct media.

As in the homogeneous medium, the residual S_w at BT and QS state with $Ca = 5.0 \times 10^{-5}$ and $Ca = 1.0 \times 10^{-4}$ are higher. This is caused by the same effect found in the homogeneous medium. Faster pore filling events in the capillary regime prevent the nonwetting fluid to redistribute equally in the pores, leading to a higher amount of trapped wetting fluid. Lower values of Ca provide more time for fluid to redistribute. Furthermore, fluid's selectivity events are also slower in cases with lower Ca, which contributes for a lower residual wetting saturation. For example, the event illustrated in Figure 32 for the case with $Ca = 5.0 \times 10^{-5}$ is not similar as in the case with $Ca = 1.0 \times 10^{-5}$. In the lowest Ca case, by the time that the front A reaches breakthrough in the thin throath, the nonwetting fluid still did not reach the location of front B. Thus, after breakthrough, front A selects the backward pore, invading all pore and moving backward instead of forward as in the case presented in Figure 32.

However, the difference in residual S_w between the low and intermediate Ca ranges in this case is lower than in the homogeneous medium. The geometry of pores and throats of the homogeneous model contributes more for the fluid redistribution.

Figure 34: Wetting fluid saturation as a function of the Ca at breakthrough and quasi-steady state for drainage in the LV60A slice model.

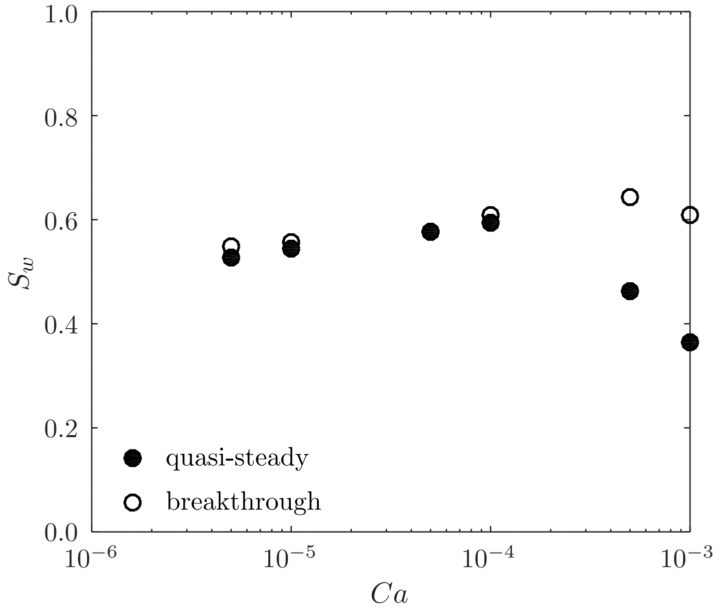

Source: elaborated by the author.

4.3 RESULTS WITH 3D POROUS ROCK IMAGES

This section presents and discuss the results of drainage in the 3D digital rock models shown in section 3.2. Parameters and setup of simulations are defined in section 3.3. The same Ca range used for drainage in the 2D models were used in 3D models. However, the two cases with lowest Ca did not reach breakthrough and quasi-steady state. The simulation takes a long time because of the relative large porous media used and low displacement rate. Thus, the results in those cases will be shown at the time where simulations were stopped, which will be properly indicated.

4.3.1 Drainage in the LV60A rock model

Figure 35 shows snapshots of drainage in the LV60A digital rock model with $Ca = 5.0 \times 10^{-5}$ at different times. Only the nonwetting fluid is represented in red. Although it is difficult to analyze the flow behavior in the snapshots of 3D models, two aspects can be seen: the connectivity of the fluid is greater than in the 2D heterogeneous model, and nonwetting fluid seems to occupy a considerable space of the porous medium. In 3D models the pores have a higher coordination number, i.e., they are interconnected with several other pores and the fluid is allowed to flow in various directions at the same time. Thus, a preferential path through the outlet is not clear, and the fluid creates various fingers that spread across the porous medium. This shows the importance of dimensionality and of a reliable representative elementary volume, i.e., the intrinsic characteristic of the geometry grants the 3D models a more consistent representation of the whole porous media than 2D models.

In Figure 36, snapshots of a slice of the 3D model at half breakthrough time, breakthrough and quasi-steady states are compared for the four simulated cases where BT and QS state were achieved. The cases with high Ca present an unstable displacement. The fluid is able to sweep a large are of the medium due to the viscous forces. They also play an important role after BT, since the nonwetting fluid keeps invading further areas and saturation increases. This is observed comparing Figures 36(b) and (c), for example.

The intermediate Ca are in the capillary fingering regime. One evidence is the lower connectivity of the fluid even at QS state. The viscous forces are low and do not contribute for invasion in thin pores and throats. A high amount of wetting fluid is trapped and BT and QS state are practically similar.

The slice refer to the location where breakthrough occurs in the intermediate Ca values. The BT in cases with high Ca occurs in a different location. This shows that opposite to the 2D heterogeneous model, there is not a similar preferential path for unstable displacement and capillary fingering. The high connectivity of pores provides more directions for the fluid to move in the unstable displacement and breakthrough occurs in a different point.

Although the preferential paths are different between different regimes, they are still similar within the same regime. This can also be seen in Figure 37, which shows the relationship between normalized frontal location of nonwetting fluid and S_{nw} during drainage. As in the 2D slice model of the LV60A rock, the two displacement patterns observed in the snapshots are represented with different coloured curves. The curves within each regime exhibit steps in similar locations, which indicates preferential paths for each Ca range. However, it is more difficult to determine those paths because of the

Figure 35: Snapshots of drainage in the LV60A digital rock model with $Ca = 5.0 \times 10^{-5}$ at different timesteps:(a) 120,000, (b) 800,000, (c) 1,580,000 and (d) 1,773,200.

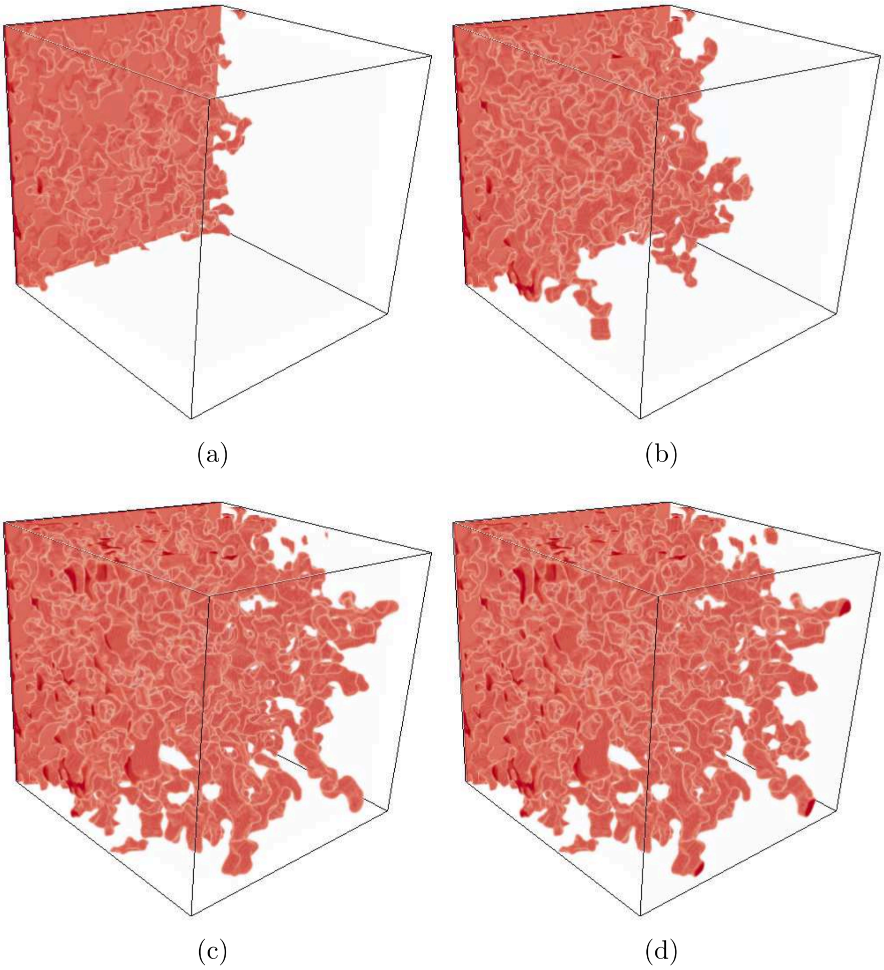
(a) (b) (c) (d)

Source: elaborated by the author.

complexity of the geometry. In this case, the breakthrough point indicates one possible path, but since the geometry is three-dimensional other paths exist and might be clear only when QS state is reached. Furthermore, it is not possible to conclude that the curves within the lowest Ca range present similar steps in similar locations as other in the capillary regime, since simulations did no reach BT.

In unstable displacement, the frontal location of nonwetting fluid increases more smoothly, and the small steps occur due local capillary fingering mechanisms. Capillary fingering presents a disordered step-like behavior due to the increase in nonwetting saturation in several directions while the most advanced finger remains at the same location. The disordered behavior is due the heterogeneity of the model, which is evident when Figures 24 and 31 are compared.

The cases in the lower Ca range did not reach breakthrough and the stop point is indicated with a cross marker. The amount of nonwetting fluid saturation for the same value of the frontal location is lower than in other Ca ranges. This indicates a possible lower value of S_{nw} at BT and QS. In the 2D models, the lower Ca cases showed a higher increase of S_{nw} with frontal location than intermediate Ca cases, and final S_{nw} was also higher. This might occur also in the 3D models, but in this case the S_{nw} would be lower.

The increase of nonwetting fluid saturation with time is shown in Figure 38, where

Figure 36: Snapshots of drainage in the LV60A digital rock model at half breakthrough time, breakthrough and quasi-steady state with four different Ca: (a)-(c) 1.0×10^{-3}, (d)-(f) 5.0×10^{-4}, (g)-(i) 1.0×10^{-4} and (j)-(l) 5.0×10^{-5}.

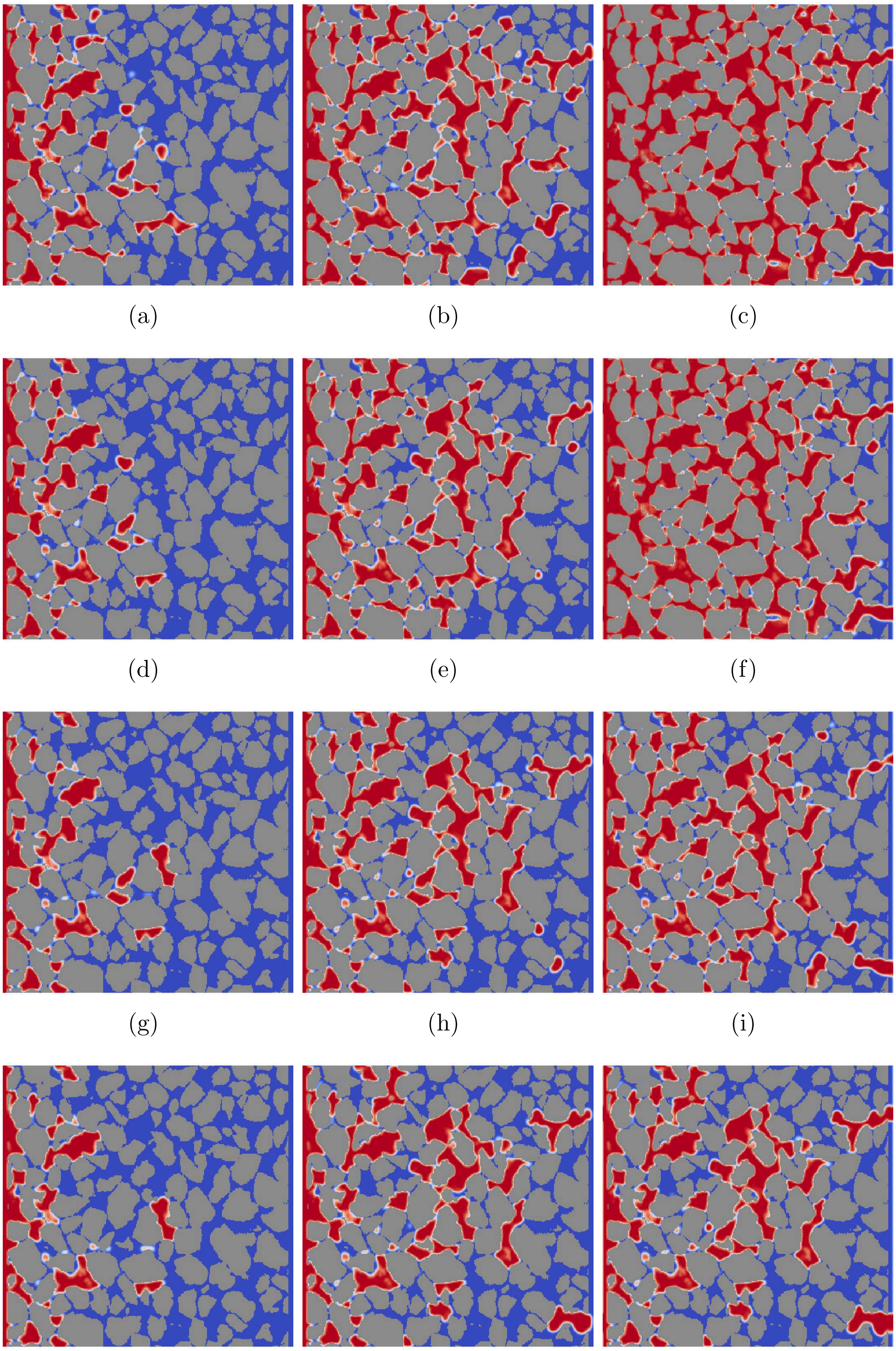
(a) (b) (c)
(d) (e) (f)
(g) (h) (i)
(j) (k) (l)

Source: elaborated by the author.

timestep is normalized. In the drainage with 3D porous models, the same stop criterion was used for all simulations. Opposite to the 2D models, it is not necessary to set different stop criterion to assure that simulation will achieve breakthrough and quasi-states. The

Figure 37: Relationship between normalized frontal location and saturation of nonwetting fluid for drainage in the LV60A digital rock model. The color of each curve represents the pattern observed in the snapshots, and the cross marker represents the location where simulation stopped in low Ca cases.

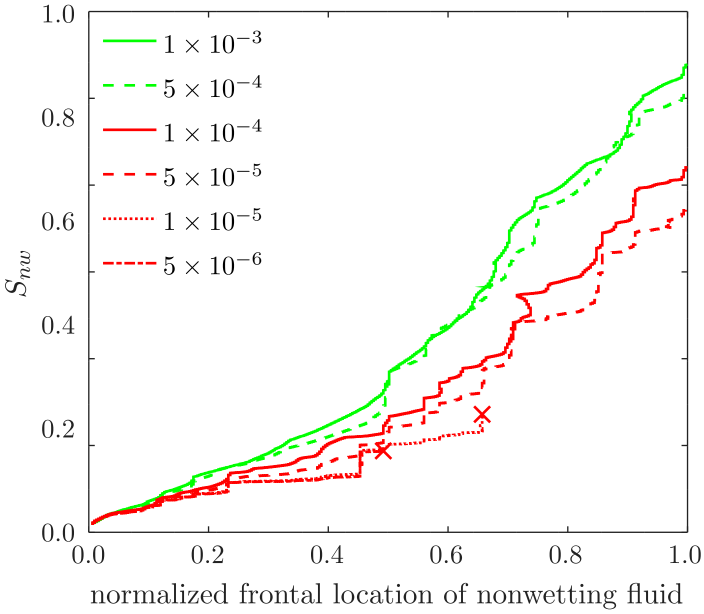

Source: elaborated by the author.

3D geometries have more interconnected pores that allow a more stable simulation (lower density ratio during displacement) and that provide several paths for the fluid to reach breakthrough. However, the total computational time required for simulations is much higher. This was an obstacle for simulations at low Ca to reach breakthrough.

The simulations in which BT and QS state was reached present a smooth increase of S_{nw} with time. As in the 2D models, after BT the rate of increase of S_{nw} decreases considerably. However, in this case, QS state takes longer to be achieved. The high connectivity of the model allows considerable invasion of nonwetting fluid after BT even at low Ca.

Total physical time of drainage is lower in 3D cases than in 2D cases. The total timesteps in the simulations with 2D slice of LV60A rock is three times higher than with the 3D image for the same values of Ca.

In Figure 34, the wetting fluid saturation at breakthrough and quasi-steady state are plotted as a function of the Ca. In both BT and QS state moments, the residual saturation of wetting fluid increases with decreasing Ca. This shows that capillary fingering regime leads to a higher amount of trapped wetting fluid as also shown in Figure 36. The values of S_w for the lower Ca range were measured at the moment in which simulations were stopped. As seen earlier, it is possible that final values are lower, since the increase of S_{nw} with frontal location of nonwetting fluid is slower.

The difference between the values of S_w at BT and QS state is larger in the high Ca range. The presence of viscous forces and high pore connectivity leads to an early breakthrough, but also to a considerable invasion of nonwetting fluid after BT.

The solid and discontinuous lines in the plot represent logarithm fitting curves with coefficients of determination $R^2 = 0.99383$ and $R^2 = 0.99274$ for breakthrough and quasi-steady state, respectively. This shows that in this case the effect of Ca in the residual

Figure 38: Nonwetting fluid saturation as a function of normalized timestep during drainage in the LV60A digital rock model. The red marker indicates the breakthrough point.

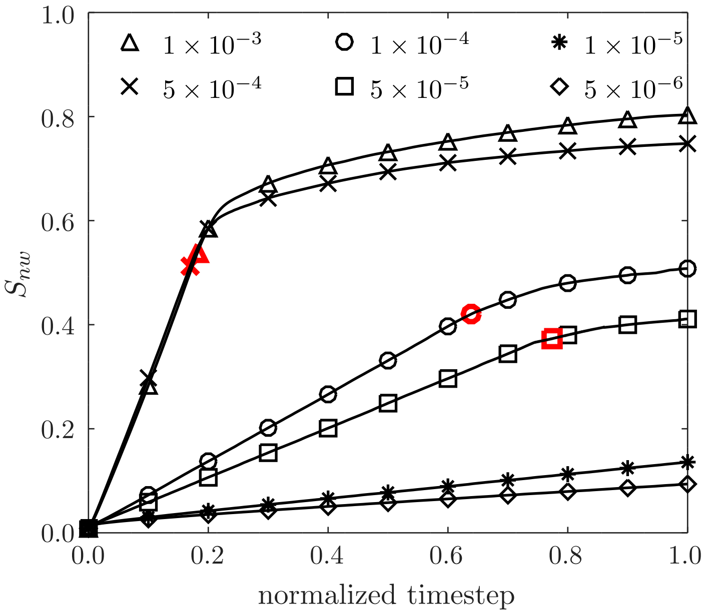

Source: elaborated by the author.

saturation might be determined by a logarithm relationship.

Figures 39 and 34 show also the importance of evaluating the residual saturation at quasi-steady state because the effect of Ca can be different in distinct media. In 3D models, S_{nw} can increase considerably after BT even in drainage with low Ca.

The residual wetting fluid is illustrated in Figure 40, which shows snapshots at quasi-steady state in the high and intermediate Ca ranges and at the time in which simulations were stopped in the lower Ca range. In lower Ca cases a high amount of wetting fluid remains trapped inside the porous media.

4.3.2 Drainage in Berea rock model

Figure 41 shows snapshots of drainage in the Berea digital rock model with $Ca = 5.0 \times 10^{-5}$ at different times. Only the nonwetting fluid is represented in red. As shown in section 3.2, the Berea rock has a lower porosity and permeability compared to the LV60A rock. This has important effects in the saturation condition during drainage. Comparing Figures 41 and 35, it is possible to see that in this case the amount of nonwetting fluid is lower, since a considerable part of the porous medium is consisted of solid grains.

The volume occupied by solid grains decreases the fluid connectivity inside the porous medium. This can be seen in Figure 42, where snapshots of a slice of the 3D model at half breakthrough time, breakthrough and quasi-steady states are compared for the four simulated cases where BT and QS state were achieved. Unstable displacement occurs in the high Ca cases and capillary fingering regime in the low Ca cases. In the first regime, the invasion is more efficient and saturation of nonwetting fluid at QS state is higher. However, the fluid connectivity is low in all cases. The difference between the regimes is mainly after BT, where the unstable displacement regime leads to fluid invasion

Figure 39: Wetting fluid saturation as a function of Ca at breakthrough and quasi-steady state for drainage in the LV60A digital rock model. The solid and discontinuous lines represent logarithm fitting curves with $R^2 = 0.99383$ and $R^2 = 0.99274$ for breakthrough and quasi-steady state, respectively.

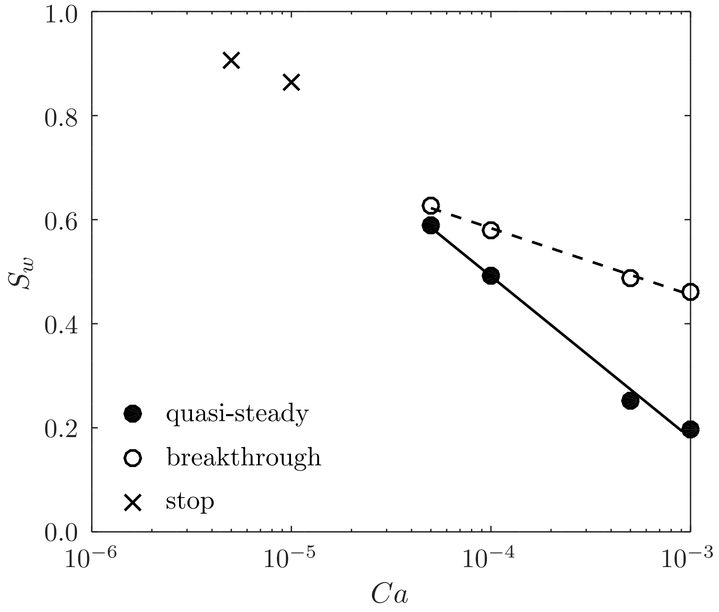

Source: elaborated by the author.

in small pores and throats.

In all cases it is not possible to determine the paths through the outlet because the additional dimension of this model is critical for the flow. In the 3D snapshots of Figure 41 it is possible to see the points where breakthrough occur. The flow in this model is more affected by side and backward movements, and if preferential paths exist it will necessarily consist of tortuous ways toward the outlet.

Figure 43 shows the relationship between normalized frontal location of nonwetting fluid and S_{nw} during drainage. As in the LV60A rock, the two displacement patterns observed in the snapshots are represented with different coloured curves and exhibit steps in similar locations, which indicates preferential paths for each Ca range. The steps in the capillary fingering regime are considerable higher, which indicates a high amount of side and backward movements, as expected for this model. The steps in this case occur near the outlet of the porous medium.

The cases in the lower Ca range did not reach breakthrough and the stop point is indicated with a cross marker. In those cases, the amount of nonwetting fluid saturation is similar with other capillary fingering curves near the outlet. This indicates that the values of S_{nw} at BT and QS might be similar using different Ca values within the capillary fingering regime.

The drainage with $Ca = 1.0 \times 10^{-5}$ stopped when nonwetting fluid was close to BT. This is evidenced by the cross marker near the outlet. The saturation level is higher than in other cases, which indicated that S_{nw} at BT would probably be higher. However, it is not possible to conclude if final S_{nw} at QS state would also be higher. Nevertheless, this shows that saturation history is highly dependent of the geometry used, since the drainage in LV60A rock model resulted in different curves (Figure 37).

Figure 44 shows the increase of nonwetting fluid saturation with time, where timestep

Figure 40: Snapshots at final state showing residual wetting fluid trapped for drainage in the LV60A digital rock model with $Ca = 1.0 \times 10^{-3}$ (a), 5.0×10^{-4} (b), 1.0×10^{-4} (c), 5.0×10^{-5} (d), 1.0×10^{-5} (e) and 5.0×10^{-6} (f).

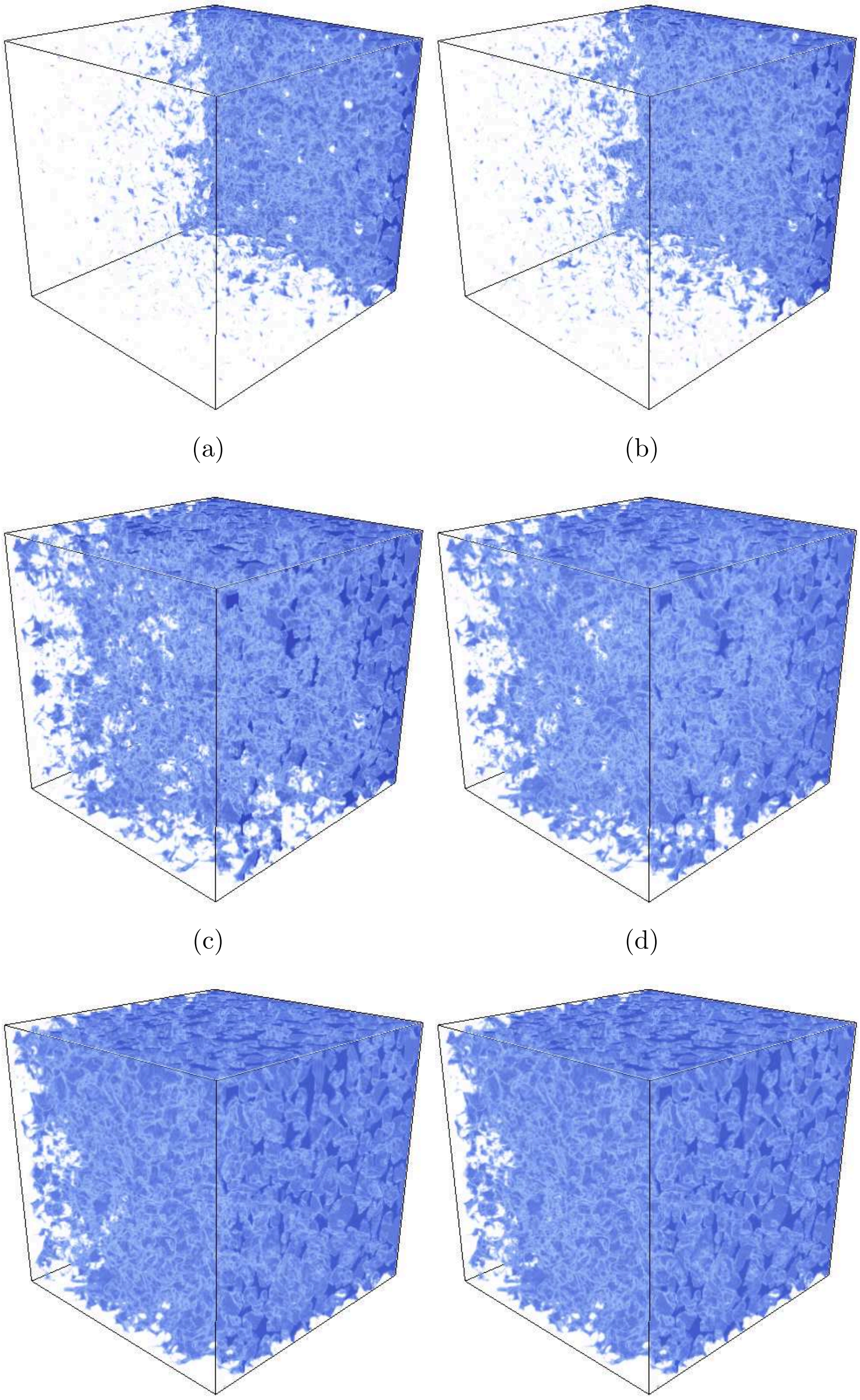

(a) (b)

(c) (d)

(e) (f)

Source: elaborated by the author.

is normalized. The simulations in which BT and QS state was reached exhibit a smooth increase of S_{nw} with time. The rate of increase of S_{nw} is still high after BT, and decreases only a considerable time after BT. Furthermore, intermediate Ca cases reach BT earlier than in the LV60A 3D rock model. This shows that a preferential path is more likely to

Figure 41: Snapshots of drainage in the Berea digital rock model with $Ca = 5.0 \times 10^{-5}$ at different timesteps:(a) 120,000, (b) 500,000, (c) 1,000,000 and (d) 1,670,000.

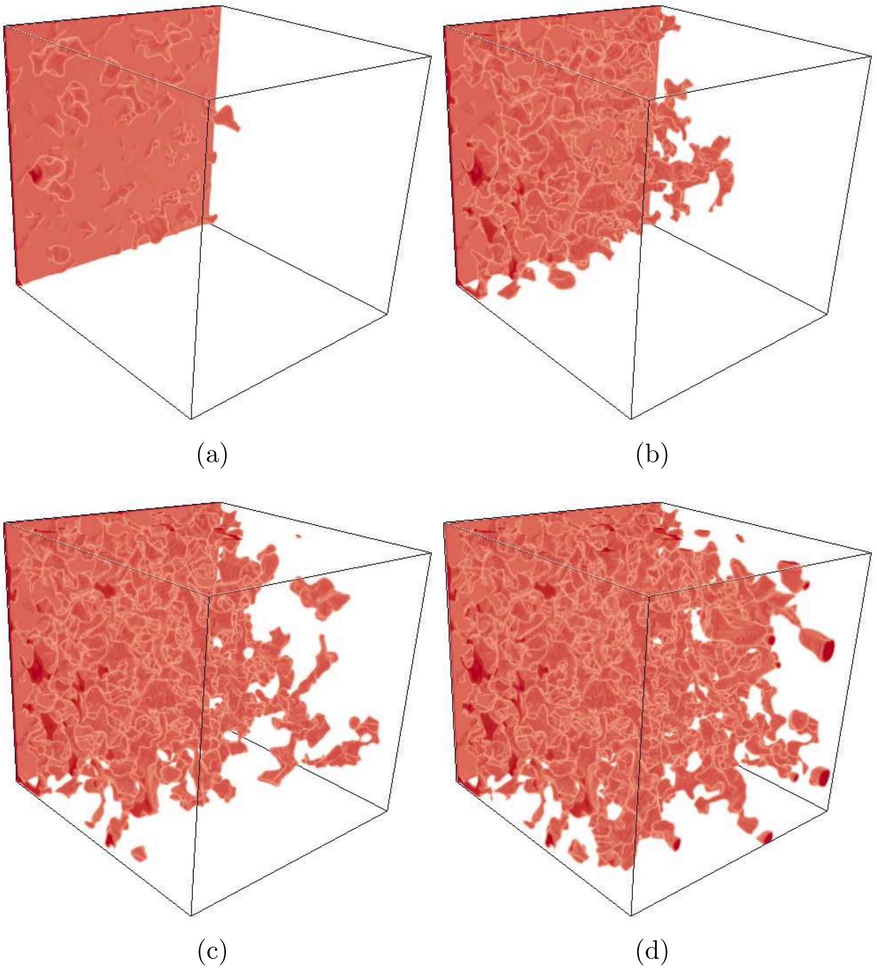
(a) (b)
(c) (d)

Source: elaborated by the author.

exist in this rock since pore connectivity is lower. This effect was also observed in the slice of the LV60A rock model (Figure 30).

Total time of simulation and physical time of drainage in this case are slightly lower than in the LV60A 3D rock model, since the amount of fluid spaces is lower.

The earlier BT in intermediary Ca cases is also observed in Figure 45, where wetting fluid saturation at breakthrough and quasi-steady state are plotted as a function of the Ca. The difference in S_w between BT and QS state is higher than in the LV60A rock model. In the high Ca range, this difference is even greater. The high velocity of displacement leads to an early breakthrough, but also to a considerable invasion of nonwetting fluid after BT.

Capillary fingering regime in this case also leads to higher residual S_w at QS state as in the LV60A rock model. However, in the present case the value of S_w at BT is similar in all Ca ranges. As seen in Figure 43, the simulation with $Ca = 1.0 \times 10^{-5}$ almost reach BT, and in Figure 45 it is clear that S_w value at BT would be similar or lower than with higher Ca. This proves that a preferential path exist in this rock and high displacement rate leads to early BT through this path. At low Ca values, the fluid also flows through the preferential path, but since displacement rate is lower, the fluid invades other pores at the same time, leading to a high S_w at BT. This is highly dependent on the geometry

Figure 42: Snapshots of drainage in the Berea digital rock model at half breakthrough time, breakthrough and quasi-steady state with four different Ca: (a)-(c) 1.0×10^{-3}, (d)-(f) 5.0×10^{-4}, (g)-(i) 1.0×10^{-4} and (j)-(l) 5.0×10^{-5}.

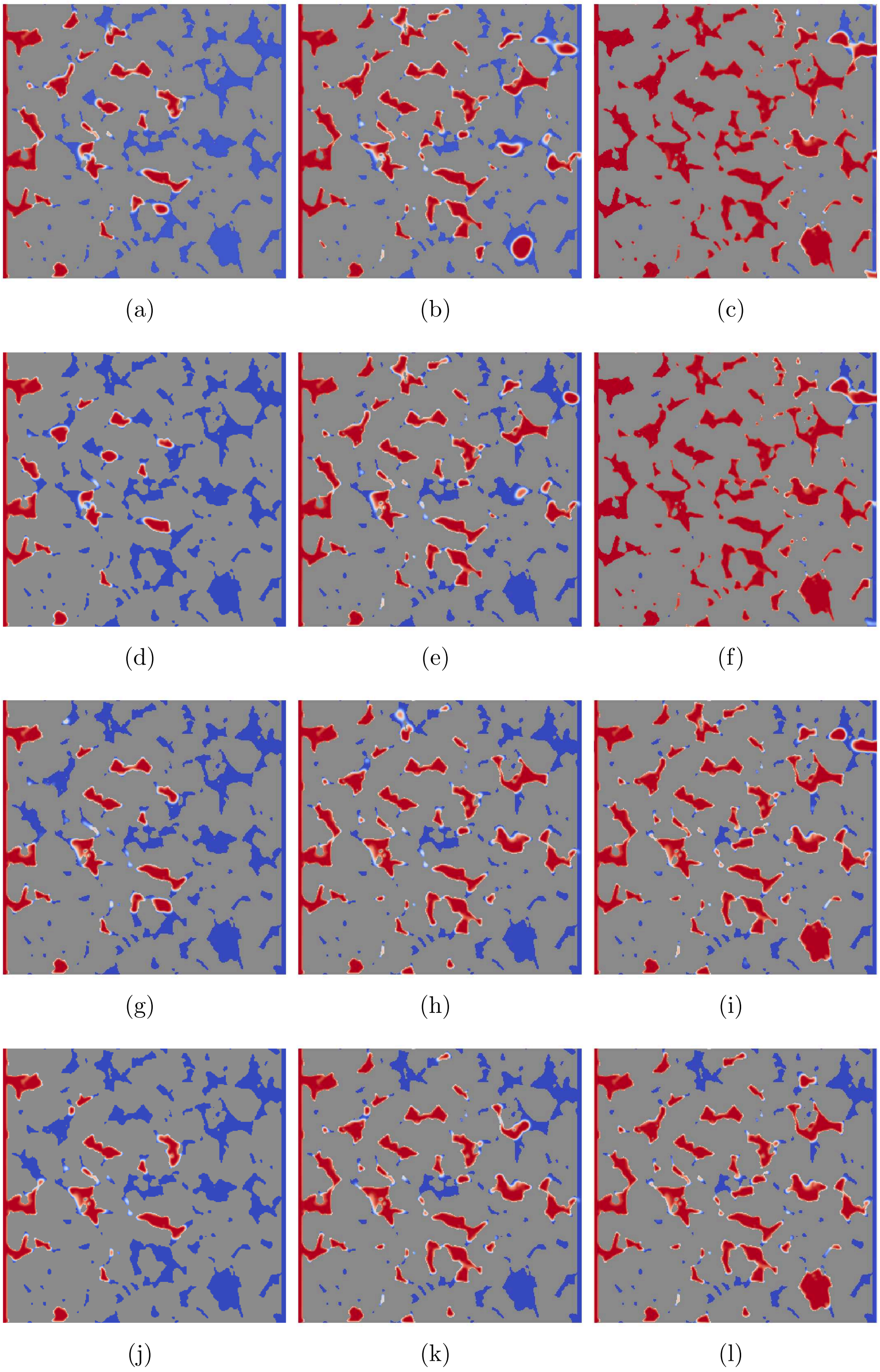

Source: elaborated by the author.

of pores and throats inside the medium.

Furthermore, it is not possible to conclude that at QS state the wetting fluid saturation would be lower in the low Ca range. Once the preferential path is found and BT

Figure 43: Relationship between normalized frontal location and saturation of nonwetting fluid for drainage in the Berea digital rock model. The color of each curve represents the pattern observed in the snapshots, and the cross marker represents the location where simulation stopped in low Ca cases.

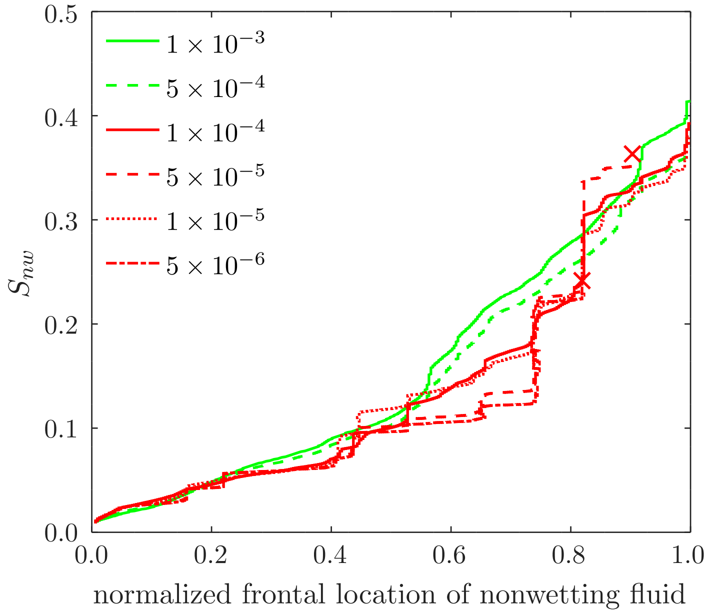

Source: elaborated by the author.

Figure 44: Nonwetting fluid saturation as a function of normalized timestep during drainage in the Berea digital rock model. The red marker indicates the breakthrough point.

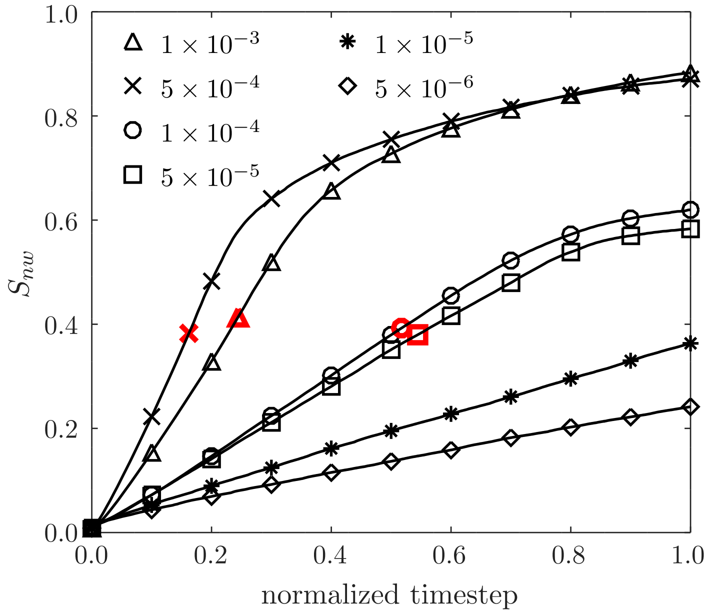

Source: elaborated by the author.

occurs, it is possible that the fluid avoids to invade further pores inside the medium since a higher pressure would be necessary. The QS state in this case would be reached right after BT, similar to what occurs with the slice of LV60A rock model (Figure 34).

The solid and discontinuous lines in the plot represent logarithm fitting curves with coefficients of determination $R^2 = 0.44754$ and $R^2 = 0.95685$ for breakthrough and quasi-steady state, respectively. This shows that the effect of Ca in the residual saturation at QS state might be determined by a logarithm relationship, but not at BT. Furthermore, Figures 45 and 39 show that the decrease in Ca leads to higher residual S_w at BT and QS state. The individual values of S_w are highly dependent on the medium geometry and degree of heterogeneity and connectivity. Also, the effect of lower Ca is not clear since simulations did not reach BT and QS state.

Figure 45: Wetting fluid saturation as a function of Ca at breakthrough and quasi-steady state for drainage in the Berea digital rock model. The solid and discontinuous lines represents logarithm fitting curves with $R^2 = 0.44754$ and $R^2 = 0.95685$ for breakthrough and quasi-steady state, respectively.

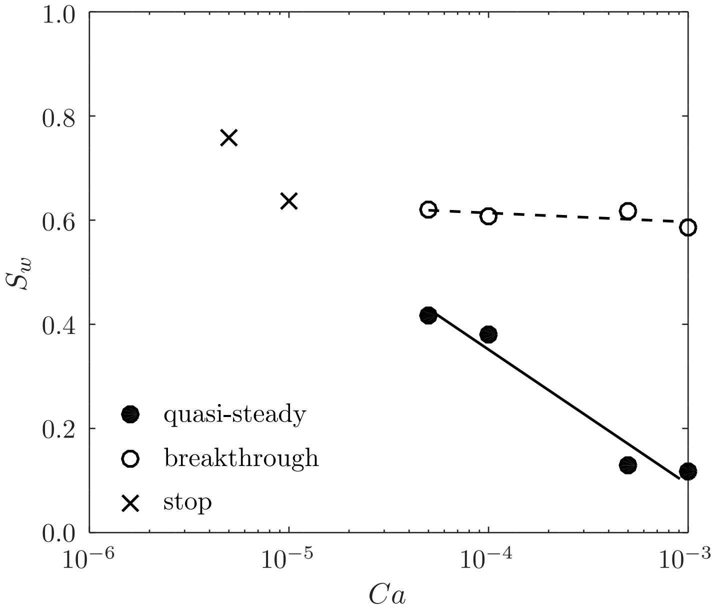

Source: elaborated by the author.

Figure 46 shows the final wetting fluid trapped in the Berea rock model. The lower Ca cases present a high amount of wetting fluid inside the porous medium. The amount, however, is lower than in the LV60A rock model. The solid grains occupy more space in this rock. Furthermore, final wetting fluid saturation values are lower in the Berea rock model in all displacement regimes. Although pore connectivity, porosity and intrinsic permeability are lower, the sweeping efficiency is higher in the Berea rock. As explained in section 3.2, the sandpack LV60A presents broader grain size distribution with more large grains. This leads to a broad pore size distribution and larger degree of heterogeneity. The rock exhibits more dead-end pores and thin pores and throats, which increases the amount of trapping.

Figure 46: Snapshots at final state showing residual wetting fluid trapped for drainage in the Berea digital rock model with $Ca = 1.0 \times 10^{-3}$ (a), 5.0×10^{-4} (b), 1.0×10^{-4} (c), 5.0×10^{-5} (d), 1.0×10^{-5} (e), 5.0×10^{-6} (f).

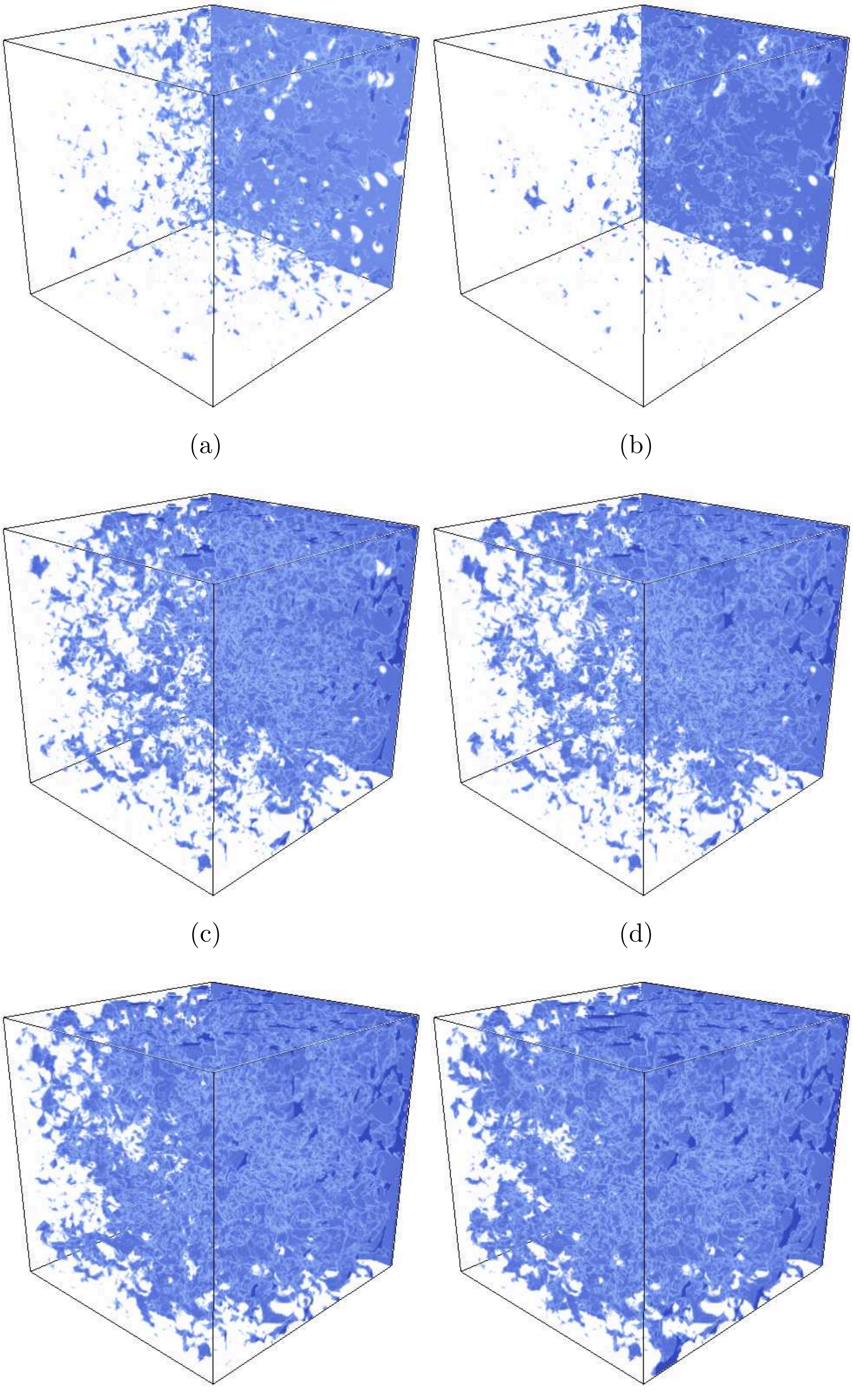

(a) (b)

(c) (d)

(e) (f)

Source: elaborated by the author.

4.3.3 Relative permeability

The fluid distributions obtained at quasi-steady state after drainage in the 3D porous models were used to calculate the relative permeability for the wetting and nonwetting fluid. A constant pressure difference was applied in the fluids and simulations were run until the relative difference of relative permeability measured each 100 timesteps reached 0.0001.

The relative permeability is calculated with Equation 2.5 for each fluid using the intrinsic permeability of each rock as shown in section 3.2 and the applied pressure difference. The flow rate Q_j is obtained with the following equation for the x direction (considering that the pressure difference is applied in the x direction):

$$Q_j = \sum_i u_{xi} S_{ij}, \tag{4.2}$$

where i indicates a lattice position and j the fluid considered.

Figures 47 and 48 show the relative permeability of nonwetting and wetting phases as a function of the capillary number during drainage and as a function of the residual wetting fluid saturation, respectively. As Ca decreases, saturation of wetting fluid increases and thus the relative permeability for the wetting fluid, while the relative permeability for the nonwetting fluid decreases considerably.

The solid and discontinuous lines in the plot represent logarithm fitting curves in Figure 47 and a linear fitting curve in Figure 48. The coefficient of determination in all cases is higher than 0.95, which indicates that at this saturation level the relative permeabilities have a linear relationship with residual saturation. Since the wetting fluid saturation exhibits a logarithm relationship with Ca (Figure 39), the same occurs with the relative permeability (Figure 47).

In Figure 47, it is possible to see that the relative permeability for the nonwetting fluid in the Berea rock is higher than in the LV60A rock for the same level of Ca. This is caused by the higher nonwetting fluid saturation reached at final state achieved in the Berea rock, i.e., the drainage process is more efficient in terms of saturation level in the rock with lower degree of heterogeneity.

A different perspective is found in Figure 48. For the same value of saturation, the relative permeability for the nonwetting fluid is slightly higher in the LV60A rock. The relative permeability for the wetting fluid is practically similar. This means that the capability of fluid transmission in the multiphase flow is slightly better in the rock with higher porosity and intrinsic permeability.

Those characteristics show the great influence of medium geometry in the sweeping process in a porous rock. On one hand, a lower degree of heterogeneity provides lower amount of trapped wetting fluid. On the other hand, a higher porosity and intrinsic permeability results in higher relative permeability for the same saturation level. Those characteristics might be present together in one single rock, but it is not the case with the Berea and LV60A rocks. This information is extremely useful to define the best method for extraction in the oil recovery industry.

Figure 47: Relative permeability of wetting and nonwetting phases as a function of the capillary number in drainage in the LV60A and Berea rock models. The solid and discontinuous lines represent logarithm fitting curves with $R^2 > 0.95$.

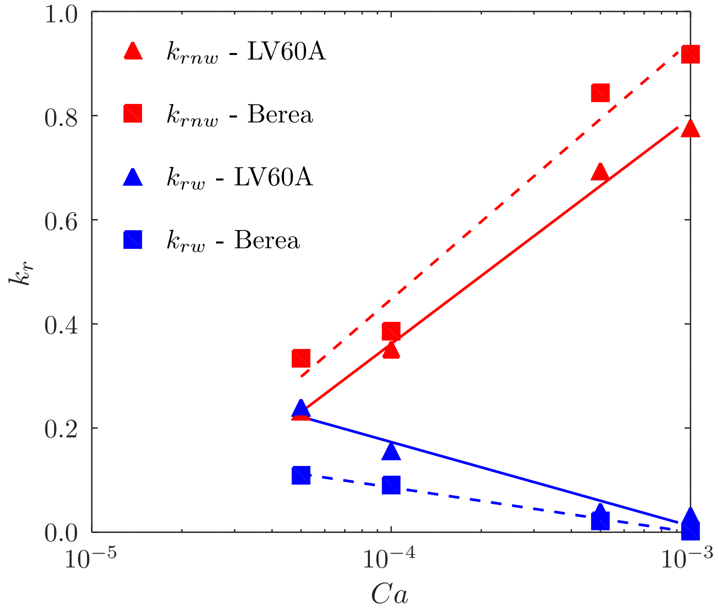

Source: elaborated by the author.

Figure 48: Relative permeability of wetting and nonwetting phases as a function of the residual wetting saturation after drainage in the LV60A and Berea rock models. The solid and discontinuous lines represent linear fitting curves with $R^2 > 0.95$.

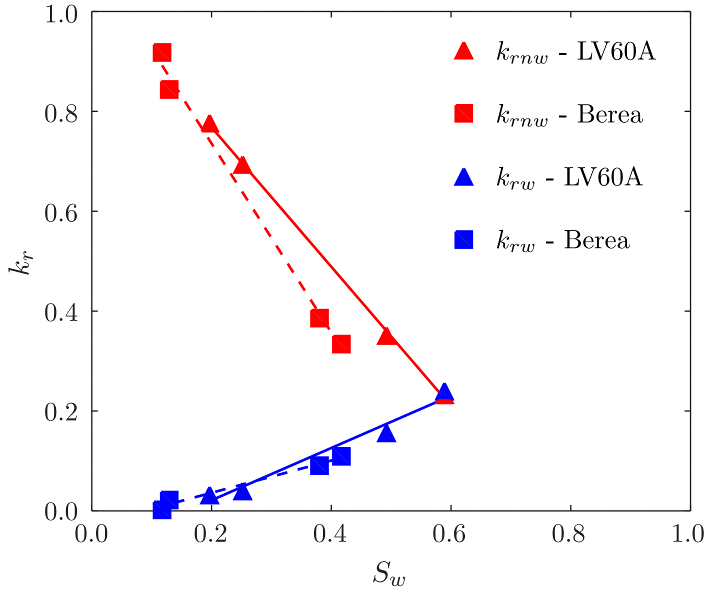

Source: elaborated by the author.

5 CONCLUSIONS

Drainage was carried out in 2D and 3D digital models of porous media using a multicomponent Lattice Boltzmann model based on a color gradient model with a two-relaxation collision scheme. The range of capillary number in simulations is within the capillary fingering and unstable displacement regimes. Viscosity, density and interfacial tension were fixed in all cases and inlet velocity was varied to reach the desired capillary number. Strongly nonwetting condition of the invading fluid was set as the wetting condition at the solid boundaries.

The model was applied in a few test cases of capillary filling and bubble tests. The interface inducing force and the wetting boundary condition showed good consistency with expected wetting and capillary effects. The implemented convective boundary condition gives reasonable physical similarity and boundary stability. The verification of these test cases was important to define properly the parameters for simulations in real porous media and to give confidence about the model.

The porous media used allowed the comparison of homogeneous and heterogeneous geometries, as well as the effect of additional dimensionality. The following conclusion remarks can be achieved from the discussion of the drainage processes:

(i) The applied multicomponent LB model was able to recover with quality the fluid dynamics during drainage in the porous media used in this work. Several aspects were observed such as the displacement patterns and pore-scale mechanisms, which are similar with observations in literature shown in section 2.3.

(ii) Pore-scale events in the capillary fingering regime such as Haines jumps are an important mechanism of trapping during drainage. In all cases their occur with frequency, specially at low Ca values, and are more intense in geometries with higher pore-throat size ratio. In 2D models, those mechanisms can lead to higher residual wetting saturation at intermediate values of Ca because of the high fluid velocity. In 3D models, the effect depends on pore connectivity and degree of heterogeneity. The inertial forces at pore-scale play an important role in those events even at low Ca.

(iii) Preferential paths for the flow are observed in the 2D and 3D models. They provide the lowest required capillary pressure for the nonwetting fluid through the outlet. In 3D models, more than one path can be found depending on the pore connectivity. In low pore connectivity media such as the Berea rock, the preferential path is more clear and has more effect on the saturation at breakthrough. Furthermore, during drainage the preferential path can be affected by the pore-scale mechanisms and surrounding fluid fronts and fingers. This leads to different preferential paths between distinct flow regimes.

(iv) Residual wetting fluid at breakthrough and quasi-steady state is highly dependent on the capillary number. A lower value of Ca leads to more trapped wetting fluid in 3D models mainly because of the media geometries. In the 2D models, the low velocity of the fluid at low Ca provided a better condition for fluid redistribution, causing a lower residual wetting fluid saturation. In all cases, the highest Ca range resulted in the lowest S_w.

(v) The degree of heterogeneity in 3D models has an important effect on residual saturation after drainage. The LV60A rock has a broad pore size distribution, with more dead-end pores and thin pores and throats, which increases the amount of trapping. The Berea rock has lower porosity and intrinsic permeability, but the degree of heterogeneity is lower than the LV60A. This leads to higher sweeping efficiency of drainage and higher relative permeability for the same Ca value used in drainage. The LV60A rock has a higher porosity and intrinsic permeability, which results in higher relative permeability for the same saturation level.

(vi) In the high level of nonwetting fluid saturation reached at quasi-steady state with 3D models, the relative permeabilities for the wetting and nonwetting fluids have a linear relationship with saturation. As the irreducible wetting fluid saturation increases the relative permeability for the wetting fluid also increases, while the opposite occurs with relative permeability for the nonwetting fluid.

As a lessons-learned, a few points might be summarized. The boundary conditions must be properly selected and implemented in the computational domain. In the present case, the inlet and outlet sections were determinant for the simulation stability. Furthermore, in simulations with 2D models the stop criteria had to be defined for each case individually. The main cause is the density ratio during the drainage. Specially in the heterogeneous models, the density ratio increases quickly due to the constant injection of nonwetting fluid in the small spaces of the media. As explained in section 3.1, the LB model used is not capable of calculating high density ratio ($\rho_R/\rho_B > 10$), and simulations diverge because of interface instabilities. Another possible solution could be to find the optimum stop criterion for the lowest Ca case and use the same criterion for cases with higher Ca. This would allow a more consistent comparison of results. An important point of using the present model is to maintain the value of α lower than 0.1 and β higher than 0.9 to achieve stable and consistent simulations.

The investigation carried out in the present work is a first step in the study of recovery efficiency in real porous media. Future works can benefit from results and final conditions of the present work. For example, imbibition displacements and further drainage processes can be simulated by using the fluid distributions achieved at final state. This allows the calculation of complete curves of relative permeability and capillary desaturation curves, which are the main inputs for decisions in the oil recovery industry. Furthermore, other possible investigations can be summarized:

(i) use lower ranges of Ca consistent with real reservoir values, with the request of higher computational resources;

(ii) set different viscosity ratio and wettability conditions, which are known to have an important effect on saturation and permeability;

(iii) use a different inlet boundary condition, such as pressure boundary condition or a defined velocity field at inlet, in order to accomplish a more realistic condition, and measure the gradient of Ca inside the rock;

(iv) use a near 2D model instead of 2D model, by creating more slices of the same 2D image in the third dimension, in order to create a similarity with micromodel experiments;

(v) mirror the digital rock image to create perfect periodic boundary conditions;

(vi) parametric study on the geometry of 3D porous images to investigate quantitatively the influence of the degree of heterogeneity and the porosity, by setting different pore-throat size ratios and other possible geometric parameters.

Finally, this work showed the potential of LBM in calculating multicomponent flow in complex geometries. The method is a strong tool for the evaluation of relevant properties of immiscible displacement in porous media. Due to computational capacity it was not possible to simulate further ranges of Ca or investigate other relevant parameters. However, the methodology presented in this work provides an efficient tool to calculate complete curves of relative permeability and capillary desaturation curves for drainage and imbibition using a variety of parameters. With the current improvement of computational technology and modelling techniques, the study of immiscible displacement is strongly benefited. Hopefully, future works may introduce new details about oil recovery by simulating the entire reservoir rock with real properties measured in site.

BIBLIOGRAPHY

ANDREW, M. et al. The imaging of dynamic multiphase fluid flow using synchrotron-based x-ray microtomography at reservoir conditions. **Transport in Porous Media**, Springer, v. 110, n. 1, p. 1–24, 2015.

ANSARINASAB, J.; JAMIALAHMADI, M. Pore-scale investigation of some effective parameters on immiscible displacement efficiency using free energy model of lattice boltzmann method. **Journal of Petroleum Science and Engineering**, Elsevier, v. 156, p. 748–762, 2017.

ARMSTRONG, R. et al. Modeling the velocity field during haines jumps in porous media. **Advances in Water Resources**, Elsevier, v. 77, p. 57–68, 2015.

ARMSTRONG, R. T. et al. Critical capillary number: Desaturation studied with fast x-ray computed microtomography. **Geophysical Research Letters**, Wiley Online Library, v. 41, n. 1, p. 55–60, 2014.

BEAR, J. **Dynamics of fluids in porous media**. New York: Dover Publications, 1972.

BEAR, J.; BACHMAT, Y. **Introduction to modeling of transport phenomena in porous media**. [S.l.]: Springer Science & Business Media, 2012.

BEAR, J.; BUCHLIN, J. **Modelling and applications of transport phenomena in porous media**. [S.l.]: Springer, 1991.

BORGMAN, O. et al. Immiscible fluid displacement in porous media with spatially correlated particle sizes. **Advances in Water Resources**, Elsevier, v. 128, p. 158–167, 2019.

CHATZIS, I.; DULLIEN, F. Dynamic immiscible displacement mechanisms in pore doublets: theory versus experiment. **Journal of Colloid and Interface Science**, Elsevier, v. 91, n. 1, p. 199–222, 1983.

CHATZIS, I.; MORROW, N. Correlation of capillary number relationships for sandstone. **Society of Petroleum Engineers Journal**, Society of Petroleum Engineers, v. 24, n. 05, p. 555–562, 1984.

CHEN, H.; CHEN, S.; MATTHAEUS, W. H. Recovery of the Navier-Stokes equations using a lattice-gas Boltzmann method. **Physical Review A**, APS, v. 45, n. 8, p. R5339, 1992.

COTTIN, C.; BODIGUEL, H.; COLIN, A. Drainage in two-dimensional porous media: From capillary fingering to viscous flow. **Physical Review E**, APS, v. 82, n. 4, p. 046315, 2010.

DONG, B.; YAN, Y.; LI, W. Lbm simulation of viscous fingering phenomenon in immiscible displacement of two fluids in porous media. **Transport in porous media**, Springer, v. 88, n. 2, p. 293–314, 2011.

DONG, B. et al. Lattice boltzmann simulation of viscous fingering phenomenon of immiscible fluids displacement in a channel. **Computers & Fluids**, Elsevier, v. 39, n. 5, p. 768–779, 2010.

DONG, H.; BLUNT, M. Pore-network extraction from micro-computerized-tomography images. **Physical review E**, APS, v. 80, n. 3, p. 036307, 2009.

DULLIEN, F. **Porous media: fluid transport and pore structure**. [S.l.]: Academic press, 1992.

GENNES, P.-G. D.; BROCHARD-WYART, F.; QUÉRÉ, D. **Capillarity and wetting phenomena: drops, bubbles, pearls, waves**. [S.l.]: Springer Science & Business Media, 2013.

GEORGIADIS, A. et al. Pore-scale micro-computed-tomography imaging: Nonwetting-phase cluster-size distribution during drainage and imbibition. **Physical Review E**, APS, v. 88, n. 3, p. 033002, 2013.

GINZBURG, I. Equilibrium-type and link-type lattice boltzmann models for generic advection and anisotropic-dispersion equation. **Advances in Water resources**, Elsevier, v. 28, n. 11, p. 1171–1195, 2005.

GUNSTENSEN, A. K. et al. Lattice Boltzmann model of immiscible fluids. **Physical Review A**, APS, v. 43, n. 8, p. 4320, 1991.

HAINES, W. Studies in the physical properties of soil. v. the hysteresis effect in capillary properties, and the modes of moisture distribution associated therewith. **The Journal of Agricultural Science**, Cambridge University Press, v. 20, n. 1, p. 97–116, 1930.

HALLIDAY, I.; HOLLIS, A.; CARE, C. Lattice boltzmann algorithm for continuum multicomponent flow. **Physical Review E**, APS, v. 76, n. 2, p. 026708, 2007.

HAZLETT, R.; CHEN, S.; SOLL, W. Wettability and rate effects on immiscible displacement: Lattice boltzmann simulation in microtomographic images of reservoir rocks. **Journal of Petroleum Science and Engineering**, Elsevier, v. 20, n. 3-4, p. 167–175, 1998.

HE, X.; CHEN, S.; ZHANG, R. A lattice Boltzmann scheme for incompressible multiphase flow and its application in simulation of rayleigh–taylor instability. **Journal of Computational Physics**, Elsevier, v. 152, n. 2, p. 642–663, 1999.

HEJAZI, S.; SHAH, S.; PINI, R. Dynamic measurements of drainage capillary pressure curves in carbonate rocks. **Chemical Engineering Science**, Elsevier, v. 200, p. 268–284, 2019.

HERRING, A. et al. Observations of nonwetting phase snap-off during drainage. **Advances in water resources**, Elsevier, v. 121, p. 32–43, 2018.

HIGUERA, F.; SUCCI, S.; BENZI, R. Lattice gas dynamics with enhanced collisions. **EPL (Europhysics Letters)**, IOP Publishing, v. 9, n. 4, p. 345, 1989.

HIGUERA, F. J.; JIMENEZ, J. Boltzmann approach to lattice gas simulations. **Europhys. Lett.**, v. 9, p. 663, 1989.

HONGJUN, W. et al. Assessment of global unconventional oil and gas resources. **Petroleum Exploration and Development**, Elsevier, v. 43, n. 6, p. 925–940, 2016.

HOU, S. et al. Evaluation of two lattice Boltzmann models for multiphase flows. **Journal of Computational Physics**, Elsevier, v. 138, n. 2, p. 695–713, 1997.

HUANG, H.; HUANG, J.-J.; LU, X.-Y. Study of immiscible displacements in porous media using a color-gradient-based multiphase lattice boltzmann method. **Computers & Fluids**, Elsevier, v. 93, p. 164–172, 2014.

HUANG, H.; SUKOP, M.; LU, X. **Multiphase lattice Boltzmann methods: Theory and application**. [S.l.]: John Wiley & Sons, 2015.

HUANG, J.; XIAO, F.; YIN, X. Lattice boltzmann simulation of pressure-driven two-phase flows in capillary tube and porous medium. **Computers & Fluids**, Elsevier, v. 155, p. 134–145, 2017.

HUGHES, R.; BLUNT, M. Pore scale modeling of rate effects in imbibition. **Transport in Porous Media**, Springer, v. 40, n. 3, p. 295–322, 2000.

IMPERIAL COLLEGE CONSORTIUM ON PORE-SCALE MODELLING. **Berea Sandstone**. figshare, Oct 2014. Disponível em: <¡*https : //figshare.com/articles/Berea*$_s$*andstone*/1153794/2¿>.

IMPERIAL COLLEGE CONSORTIUM ON PORE-SCALE MODELLING. **LV60A sandpack**. figshare, Oct 2014. Disponível em: <¡*https : //figshare.com/articles/LV*60A_s*andpack*/1153795/2¿>.

INGHAM, D.; POP, I. **Transport Phenomena in Porous Media**. [S.l.]: Elsevier Science, 1998. ISBN 9780080543192.

JAMALOEI, B. Y.; ASGHARI, K.; KHARRAT, R. The investigation of suitability of different capillary number definitions for flow behavior characterization of surfactant-based chemical flooding in heavy oil reservoirs. **Journal of Petroleum Science and Engineering**, v. 90-91, p. 48–55, 2012.

JIANG, L. et al. The role of flow rates on flow patterns and saturation in high-permeability porous media. **International Journal of Greenhouse Gas Control**, Elsevier, v. 78, p. 364–374, 2018.

KHISHVAND, M.; AKBARABADI, M.; PIRI, M. Micro-scale experimental investigation of the effect of flow rate on trapping in sandstone and carbonate rock samples. **Advances in water resources**, Elsevier, v. 94, p. 379–399, 2016.

LAKE, L. W. **Enhanced oil recovery**. [S.l.]: Old Tappan, NJ; Prentice Hall Inc., 1989.

LENORMAND r¿; TOUBOUL, E.; ZARCONE, C. Numerical models and experiments on immiscible displacements in porous media. **Journal of fluid mechanics**, Cambridge University Press, v. 189, p. 165–187, 1988.

LIU, H. et al. Multiphase lattice Boltzmann simulations for porous media applications. **Computational Geosciences**, Springer, v. 20, n. 4, p. 777–805, 2016.

LIU, H. et al. Pore-scale simulations of gas displacing liquid in a homogeneous pore network using the lattice boltzmann method. **Transport in porous media**, Springer, v. 99, n. 3, p. 555–580, 2013.

LOU, Q.; GUO, Z.; SHI, B. Evaluation of outflow boundary conditions for two-phase lattice boltzmann equation. **Physical review E**, APS, v. 87, n. 6, p. 063301, 2013.

MATTILA, K. et al. An efficient swap algorithm for the lattice boltzmann method. **Computer Physics Communications**, Elsevier, v. 176, n. 3, p. 200–210, 2007.

MATTILA, K. et al. Comparison of implementations of the lattice-boltzmann method. **Computers & Mathematics with Applications**, Elsevier, v. 55, n. 7, p. 1514–1524, 2008.

MCNAMARA, G. R.; ZANETTI, G. Use of the Boltzmann equation to simulate lattice-gas automata. **Physical review letters**, APS, v. 61, n. 20, p. 2332, november 1988.

MOHAMAD, A. A. **Lattice Boltzmann method: fundamentals and engineering applications with computer codes**. [S.l.]: Springer Science & Business Media, 2011.

MORROW, N.; CHATZIS, I.; TABER, J. Entrapment and mobilization of residual oil in bead packs. **SPE Reservoir Engineering**, Society of Petroleum Engineers, v. 3, n. 03, p. 927–934, 1988.

MOSTAGHIMI, P.; BLUNT, M.; BIJELJIC, B. Computations of absolute permeability on micro-ct images. **Mathematical Geosciences**, Springer, v. 45, n. 1, p. 103–125, 2013.

NGUYEN, V. et al. The effect of displacement rate on imbibition relative permeability and residual saturation. **Journal of Petroleum Science and Engineering**, Elsevier, v. 52, n. 1-4, p. 54–70, 2006.

NILSSON, M. et al. Effect of fluid rheology on enhanced oil recovery in a microfluidic sandstone device. **Journal of Non-Newtonian Fluid Mechanics**, Elsevier, v. 202, p. 112–119, 2013.

PATEL, H.; KUIPERS, J.; PETERS, E. Effect of flow and fluid properties on the mobility of multiphase flows through porous media. **Chemical Engineering Science**, Elsevier, v. 193, p. 243–254, 2019.

PEREIRA, G. Fluid flow, relative permeabilities and capillary pressure curves through heterogeneous porous media. **Applied Mathematical Modelling**, Elsevier, 2019.

PHILIPPI, P. et al. From the continuous to the lattice boltzmann equation: The discretization problem and thermal models. **Physical Review E**, APS, v. 73, n. 5, p. 056702, 2006.

PHILIPPI, P. et al. High-order lattice-boltzmann. **Journal of the Brazilian Society of Mechanical Sciences and Engineering**, v. 38, n. 5, p. 1401–1419, Jun 2016.

QIAN, Y. H.; D'HUMIÈRES, D.; LALLEMAND, P. Lattice BGK models for Navier-Stokes equation. **EPL (Europhysics Letters)**, IOP Publishing, v. 17, n. 6, p. 479, 1992.

RAEINI, A.; BIJELJIC, B.; BLUNT, M. Modelling capillary trapping using finite-volume simulation of two-phase flow directly on micro-ct images. **Advances in Water Resources**, Elsevier, v. 83, p. 102–110, 2015.

RAEINI, A.; BLUNT, M.; BIJELJIC, B. Direct simulations of two-phase flow on micro-ct images of porous media and upscaling of pore-scale forces. **Advances in Water Resources**, Elsevier, v. 74, p. 116–126, 2014.

ROTHMAN, D. H. Cellular-automaton fluids: A model for flow in porous media. **Geophysics**, Society of Exploration Geophysicists, v. 53, n. 4, p. 509–518, 1988.

ROTHMAN, D. H.; KELLER, J. M. Immiscible cellular-automaton fluids. **Journal of Statistical Physics**, Springer, v. 52, n. 3–4, p. 1119–1127, 1988.

RUSPINI, L.; ØREN, R. F. P. Pore-scale modeling of capillary trapping in water-wet porous media: A new cooperative pore-body filling model. **Advances in Water Resources**, Elsevier, v. 108, p. 1–14, 2017.

SATTER, A.; IQBAL, G. 3 - reservoir rock properties. In: **Reservoir Engineering**. Boston: Gulf Professional Publishing, 2016. p. 29 – 79. ISBN 978-0-12-800219-3.

SAYARI, S. A. The influence of wettability and carbon dioxide injection on hydrocarbon recovery. Imperial College London, 2009.

SHAN, X.; CHEN, H. Lattice Boltzmann model for simulating flows with multiple phases and components. **Physical Review E**, APS, v. 47, n. 3, p. 1815, 1993.

SHAN, X.; YUAN, X.-F.; CHEN, H. Kinetic theory representation of hydrodynamics: a way beyond the navier–stokes equation. **Journal of Fluid Mechanics**, Cambridge University Press, v. 550, p. 413–441, 2006.

SIEBERT, D. et al. Thermal lattice boltzmann in two dimensions. **International Journal of Modern Physics C**, World Scientific, v. 18, n. 04, p. 546–555, 2007.

SPENCER, T.; HALLIDAY, I.; CARE, C. Lattice boltzmann equation method for multiple immiscible continuum fluids. **Physical Review E**, APS, v. 82, n. 6, p. 066701, 2010.

SPENCER, T.; HALLIDAY, I.; CARE, C. A local lattice boltzmann method for multiple immiscible fluids and dense suspensions of drops. **Philosophical Transactions of the Royal Society A: Mathematical, Physical and Engineering Sciences**, The Royal Society Publishing, v. 369, n. 1944, p. 2255–2263, 2011.

SUCCI, S. **The lattice Boltzmann equation: for fluid dynamics and beyond**. [S.l.]: Oxford university press, 2001.

SUKOP, M.; OR, D. Invasion percolation of single component, multiphase fluids with lattice boltzmann models. **Physica B: Condensed Matter**, Elsevier, v. 338, n. 1-4, p. 298–303, 2003.

SUKOP, M.; THORNE, D. **Lattice Boltzmann Modeling Lattice Boltzmann Modeling**. [S.l.]: Springer, 2006.

SUN, Z.; SANTAMARINA, J. Haines jumps: Pore scale mechanisms. **Phys. Rev. E**, American Physical Society, v. 100, p. 023115, Aug 2019.

SWIFT, M. R. et al. Lattice Boltzmann simulations of liquid-gas and binary fluid systems. **Physical Review E**, APS, v. 54, n. 5, p. 5041, 1996.

TALABI, O. et al. Predictive pore-scale modeling: from three-dimensional images to multiphase flow simulations. **Proceedings of the Society of Petroleum Engineers, Denver, SPE**, v. 115535, 2008.

TSUJI, T.; JIANG, F.; CHRISTENSEN, K. Characterization of immiscible fluid displacement processes with various capillary numbers and viscosity ratios in 3d natural sandstone. **Advances in Water Resources**, Elsevier, v. 95, p. 3–15, 2016.

WANG, Y. et al. Pore scale investigation on scaling-up micro-macro capillary number and wettability on trapping and mobilization of residual fluid. **Journal of contaminant hydrology**, Elsevier, v. 225, p. 103499, 2019.

WARDA, H. et al. Lattice boltzmann simulations of the capillary pressure bump phenomenon in heterogeneous porous media. **Journal of Petroleum Science and Engineering**, Elsevier, v. 157, p. 558–569, 2017.

WILKINSON, D.; WILLEMSEN, J. Invasion percolation: a new form of percolation theory. **Journal of Physics A: Mathematical and General**, IOP Publishing, v. 16, n. 14, p. 3365, 1983.

WOLF, F.; SANTOS, L. dos; PHILIPPI, P. Micro-hydrodynamics of immiscible displacement inside two-dimensional porous media. **Microfluidics and nanofluidics**, Springer, v. 4, n. 4, p. 307, 2008.

WOLF, F. G. Modelagem da interação fluido-sólido para simulação de molhabilidade e capilaridade usando o modelo Lattice-Boltzmann. Florianópolis, SC, 2006.

WOLF-GLADROW, D. A. **Lattice-gas cellular automata and lattice Boltzmann models: an introduction**. New York: Springer, 2004.

XU, R. et al. Continuous vs discontinuous capillary desaturation and implications for ior/eor. In: **Paper SCA2018-066 presented at at the International Symposium of the Society of Core Analysts held in Trondheim, Norway**. [S.l.: s.n.], 2018.

YEKEEN, N. et al. Nanoparticles applications for hydraulic fracturing of unconventional reservoirs: A comprehensive review of recent advances and prospects. **Journal of Petroleum Science and Engineering**, v. 178, p. 41–73, 2019.

YIOTIS, A. et al. A lattice boltzmann study of viscous coupling effects in immiscible two-phase flow in porous media. **Colloids and Surfaces A: Physicochemical and Engineering Aspects**, Elsevier, v. 300, n. 1-2, p. 35–49, 2007.

ZACHAROUDIOU, I.; BOEK, E. Capillary filling and haines jump dynamics using free energy lattice boltzmann simulations. **Advances in water resources**, Elsevier, v. 92, p. 43–56, 2016.

ZHANG, C. et al. Influence of viscous and capillary forces on immiscible fluid displacement: Pore-scale experimental study in a water-wet micromodel demonstrating viscous and capillary fingering. **Energy & Fuels**, ACS Publications, v. 25, n. 8, p. 3493–3505, 2011.

ZHAO, B.; MOHANTY, K. Effect of wettability on immiscible viscous fingering in porous media. **Journal of Petroleum Science and Engineering**, Elsevier, v. 174, p. 738–746, 2019.

ZOU, Q.; HE, X. On pressure and velocity boundary conditions for the lattice boltzmann bgk model. **Physics of fluids**, AIP, v. 9, n. 6, p. 1591–1598, 1997.